

# PLACE IN RETURN BOX to remove this checkout from your record. TO AVOID FINES return on or before date due.

DATE DUE	DATE DUE	DATE DUE
JUN 2 4 2	000	

1/98 c/CIRC/DateDue.p65-p.14

## DESIGN AND DEVELOPMENT OF LOW SOLIDITY VANED DIFFUSERS FOR CENTRIFUGAL COMPRESSORS

By

**Won Joong Kim** 

## **A DISSERTATION**

Submitted to
Michigan State University
in partial fulfillment of the requirements
for the degree of

**DOCTOR OF PHILOSOPHY** 

**Department of Mechanical Engineering** 

1998

#### **ABSTRACT**

## DESIGN AND DEVELOPMENT OF LOW SOLIDITY VANED DIFFUSERS FOR CENTRIFUGAL COMPRESSORS

By

#### Won Joong Kim

Interest has recently increased in the use of Low Solidity Vaned Diffusers. Typically downstream of a centrifugal compressor impeller, three types of radial diffusers are used: 1) vaneless diffuser (VNL), 2) conventional vaned diffuser (CVND), and 3) Low Solidity Vaned Diffuser (LSVD). It is well known that a low solidity vaned diffuser is a good compromise between the vaneless diffuser and the conventional vaned diffuser.

Four low solidity vaned diffusers (LSVD5 through LSVD8) were designed for experimental analysis. Experimental testing of a centrifugal compressor with the low solidity vaned diffusers along with two vaneless diffusers and one vaned diffuser has been carried out downstream of the same impeller to understand the pressure recovery phenomena in each of the three types of diffusers, and the effect of design parameters on performance and the results were compared with the results from numerical simulation. The design parameters include the solidity, turning angle, vane setting angle angle, and the number of vanes. The testing was performed at three different rotational speeds (Mu=0.69, 0.88, 1.02). The experimental results proved the superior merits of LSVDs

relative to the vaneless and vaned diffuser. The LSVD fulfilled the high expectations since they seemed to combine the advantages of the conventional diffuser systems by providing a good pressure recovery over a wide flow range.

Besides steady performance analysis, pressure fluctuations were measured to understand the instability of a compressor stage such as stall and surge using fast response dynamic pressure transducers installed in various locations of the compressor stage. A rotating stall was found only with the vaneless diffuser configurations. It is presumed the progressive impeller stall is due to the destabilization of the impeller flow. This fluctuation was added to the destabilization of the vaneless diffuser and triggered the stage surge with high fluctuation.

Some of the experimentally tested low solidity vaned diffusers were compared with 3-D viscous calculations to understand the flow phenomena inside the diffuser. The effect of geometric parameters of the low solidity vaned diffuser on the flow characteristics was also investigated by numerical calculation. The results showed that low solidity vaned diffuser stalls when the vane suction surface separation was accompanied by the end wall separation, and this qualitatively compared well with the experiments.

Copyright by Won J. Kim 1998 To all my family and all my teachers.

#### **ACKNOWLEDGMENTS**

I am very grateful to my advisor, Professor Abraham Engeda, for his guidance, support, and encouragement throughout the course of this research work. Sincere thanks go to Professors Craig W. Somerton, Clark J. Radcliffe, Charles R. MacCluer and Mr. Ronald H. Aungier for their invaluable advice, suggestions, and continued interest in my work. Mr. Aungier has been most generous with his time throughout this research work; I have been supported in many ways by his considerable experience and special considerations.

I wish to particularly acknowledge many helpful discussions with Mr. Chuck Boal, Bill Hohlweg, Ken Greene, and Frank Kushner of Elliott Company. I also appreciate the numerous criticisms, assistance, and great friendship of Dr. Jean-Luc Di Liberti of Turbomachinery Lab., Michigan State University. I also thank Mr. Craig Gunn for his help in preparing my thesis.

The support of Elliott Company, Trane Company, and Division of Engineering Research is greatly appreciated. Much of the research was made possible with the equipment provided by Elliott Company.

Last but not least, I would like to thank my parents not only for financial support but also for their spiritual encouragement; my wife, Jiyoung; and my son, Hanul for their love at all times. Also I will cherish the memories with many Korean friends at Michigan State University.

## TABLE OF CONTENTS

LIST	IST OF TABLES	
LIST	T OF FIGURES	X
NOM	MENCLATURE	XII
1.	INTRODUCTION	1
1.1.	CENTRIFUGAL COMPRESSORS AND DEMANDS ON THEM	1
1.2.	THE IMPELLER	4
1.3.	THE RADIAL DIFFUSER	6
1.3	<b></b>	6
	3.2. Vaned Diffusers	
1.4.	OBJECTIVE OF THE PRESENT WORK	11
2.	THE CENTRIFUGAL COMPRESSOR	15
2.1.	STEADY FLOW OF A CENTRIFUGAL COMPRESSOR	
2.1	··· - ·· - ·· - ·· - ·· - ·· - ·· - ··	
2. <i>1</i>		
2.2.	INSTABILITY OF A COMPRESSOR STAGE	
2.2		
2.2		
2.3.	RESEARCH STATUS ON LOW SOLIDITY VANED DIFFUSER	
2.4.	LOW SOLIDITY VANED DIFFUSER DESIGN	45
<b>3.</b>	EXPERIMENTAL SETUP	48
3.1.	Test Compressor	48
3.2.	INVESTIGATED LOW SOLIDITY VANED DIFFUSERS	50
3.3.	MEASUREMENT	51
3.4.	STEADY PERFORMANCE DATA ACQUISITION	55
3.4		
3.4		
3.5.	Unsteady Performance Data Acquisition	
3.5	5.1. Obtaining and Storing the Pressure Signal	64
3.5		
3.5	5.3. Analysis of the Data	68
4.	EXPERIMENTAL RESULTS OF STEADY PERFORMANCE	72
4.1.	OVERALL PERFORMANCE CHARACTERISTICS	
4.1	1.1. Effect of Solidity	75
4.1		
4.1	1.3. Effect of the Turning Angle on the Operating Range	
4.2.	PRESSURE RISE IN THE STAGE WITH THE LOW SOLIDITY VANED DIFFUSERS	85
4.3.	Pressure Recoveries in the Diffusers	89
12	2.1 Subdivided Pressure Personaries	0.2

	EXPERIMENTAL RESULTS ON INSTABILITY IN A CENTRIFUG MPRESSOR STAGE	
5.1.		
<i>5</i> .	1.1. Unsteady Behavior of the Stage with the Vaneless Diffusers	97
<i>5</i> .	1.2. Unsteady Behavior of the Stage with the Vaned Diffuser	
<i>5</i> .	1.3. Unsteady Behavior of the Stage with the Low Solidity Vaned Diffusers	
5.2.	INDUCER STALL	
5.3.	ROTATING STALL	111
5.4.	SURGE	111
6.	NUMERICAL CALCULATION OF LOW SOLIDITY VANED DIFF	USERS 113
6.1.	3-D Viscous Flow Solver	113
6.2.	GRID GENERATION AND BOUNDARY CONDITIONS	115
6.3.	CALCULATION RESULTS	120
6.	3.1. Pressure Distributions in the Diffusers	
6.	3.2. Flow Field in the Diffusers	122
6.	3.3. Separation at the Diffuser Vane	<b>12</b> 3
6.	3.4. Vane Setting Angle Effect	124
7.	CONCLUSIONS AND RECOMMENDATIONS	140
API	PENDICES	143
BIB	BLIOGRAPHY	147

## LIST OF TABLES

TABLE 3-1 DIFFUSER GEOMETRIC PARAMETERS	
TABLE 3-2. SUMMARY OF MEASUREMENTS AND MEASUREMENT LOCATIONS	55
TABLE 3-3 NUMBER OF ROTATING STALL CELLS	71
TABLE 5-1 SUMMARY OF THE IMPELLER ROTATING STALL	111
Table 5-2 Summary of surge	112

## **LIST OF FIGURES**

FIGURE 1.1 COMPONENTS OF CENTRIFUGAL COMPRESSOR	1
FIGURE 1.2 H-S DIAGRAM FOR THE CENTRIFUGAL COMPRESSOR STAGE	2
FIGURE 1.3 VELOCITY TRIANGLES FOR AN IDEALIZED IMPELLER	4
FIGURE 1.4 EFFECT OF THE IMPELLER EXIT BLADE ANGLE	4
FIGURE 1.5 TYPES OF VANED DIFFUSERS	9
FIGURE 2.1 JET-WAKE FLOW PATTERN OF IMPELLER DISCHARGING FLOW	15
FIGURE 2.2 AN EXAMPLE OF MEASURED JET/WAKE FLOW AT THE EXIT OF IMPELLER	
(ECKARDT, 1975)	17
FIGURE 2.3 COMPARISON OF IMPELLER DISCHARGE VELOCITY (KRAIN, 1988)	20
FIGURE 2.4 TRAVERSE AT DIFFUSER INLET (FISHER ET AL., 1981)	22
FIGURE 2.5 PITCHWISE DISTRIBUTION OF ABSOLUTE FLOW ANGLE DIFFERENCE AT IMPER	LER
EXIT (HATHAWAY ET AL., 1993)	24
FIGURE 2.6 FLOW REGIME IN STRAIGHT WALL 2 DIMENSIONAL DIFFUSERS	26
FIGURE 2.7 LOSS MAP OF A DIFFUSER (JAPIKSE, 1984)	27
FIGURE 2.8 CONTOURS OF TOTAL PRESSURE LOSS COEFFICIENT	29
FIGURE 2.9 CONTOURS OF LOSS OF STAGE EFFICIENCY PER UNIT WORK COEFFICIENT	29
FIGURE 2.10 PERFORMANCE OF THE VANED DIFFUSERS (YOSHINAGA ET AL., 1980)	30
FIGURE 2.11 AN EXAMPLE OF THE SEPARATED FLOW IN A 2-D DIFFUSER	31
FIGURE 2.12 INDUCER STALL DUE TO HIGH INCIDENCE	
FIGURE 2.13 CRITICAL CONDITIONS OF INDUCER STALL (SENOO ET AL., 1979)	33
FIGURE 2.14 SEQUENCE OF PASSAGE STALL IN A SINGLE PASSAGE, UNSHROUDED IMPEL	
(Lennemann et al., 1970)	35
FIGURE 2.15 CRITICAL INLET FLOW ANGLE WITH DIFFUSER WIDTH (VAN DEN	
Braembussche et al., 1980)	
FIGURE 2.16 COMPARISON OF PRESSURE DISTRIBUTIONS (SENOO ET AL., 1983)	
FIGURE 2.17 MAXIMUM SOLIDITY	47
FIGURE 3.1 COMPRESSOR TEST STAND	
FIGURE 3.2 CENTRIFUGAL COMPRESSOR IMPELLER	
FIGURE 3.3 LSVD GEOMETRY NOTATION	
FIGURE 3.4 MEASUREMENT PLANES IN INLET PIPE	
FIGURE 3.5 MEASUREMENT LOCATIONS	53
FIGURE 3.6 UNSTEADY FLOW SIGNAL PATH	
Figure 4.1 Performance characteristics of the stage at $M_U$ =1.02	
Figure 4.2 Performance characteristics of the stage at $M_U$ =0.88	77
Figure 4.3 Performance characteristics of the stage at $M_U$ =0.69	78
FIGURE 4.4 EFFECT OF SOLIDITY ON THE PERFORMANCE	80
FIGURE 4.5 EFFECT OF VANE NUMBER ON THE PERFORMANCE	
FIGURE 4.6 EFFECT OF TURNING ANGLE	85
FIGURE 4.7 PRESSURE RISE IN THE STAGE WITH THE LOW SOLIDITY VANED DIFFUSER	87
FIGURE 4.8 DIFFUSER PRESSURE RECOVERY (CP <sub>25</sub> ) AT M <sub>U</sub> =1.02	90
FIGURE 4.9 DIFFUSER PRESSURE RECOVERY (CP <sub>25</sub> ) AT M <sub>U</sub> =0.88	

FIGURE 4.10 DIFFUSER PRESSURE RECOVERY (CP <sub>25</sub> ) AT M <sub>U</sub> =0.69	92
Figure 4.11 Subdivided pressure recovery in the diffusers at $M_{\text{U}}$ =1.02	
Figure 4.12 Subdivided pressure recovery in the diffusers at $M_{\text{U}}$ =0.88	95
Figure 4.13 Subdivided pressure recovery in the diffusers at $M_u$ =0.69	
FIGURE 5.1 POWER SPECTRUM OF THE STAGE WITH THE VNL2	
FIGURE 5.2 POWER SPECTRUM OF THE STAGE WITH THE VNL1	104
FIGURE 5.3 POWER SPECTRUM OF THE STAGE WITH THE CVND	105
FIGURE 5.4 POWER SPECTRUM OF THE STAGE WITH THE LSVD5	106
FIGURE 5.5 POWER SPECTRUM OF THE STAGE WITH THE LSVD6	107
FIGURE 5.6 POWER SPECTRUM OF THE STAGE WITH THE LSVD7	108
FIGURE 5.7 POWER SPECTRUM OF THE STAGE WITH THE LSVD8	109
FIGURE 5.8 TEMPERATURES IN THE DIFFUSER	110
FIGURE 6.1 COMPUTATIONAL MESH OF LSVD5 (105 x 50 x 17)	117
FIGURE 6.2 PRESSURE RATIO CURVES OF THE STAGE WITH THE FLOWS USED FOR THE	
NUMERICAL CALCULATION	118
FIGURE 6.3 PRESSURE RISE IN THE STAGE WITH THE LSVD5	119
FIGURE 6.4 GEOMETRY OF THE LSVD5	119
Figure 6.5 Pressure distribution at design flow & $M_U$ =0.69	
Figure 6.6 Pressure distribution at near surge flow & $M_U$ =0.69	127
FIGURE 6.7 PRESSURE DISTRIBUTION AT NEAR CHOKE FLOW & M <sub>U</sub> =0.69	128
FIGURE 6.8 FLOW PATTERN AT DESIGN FLOW & M <sub>U</sub> =0.69	
FIGURE 6.9 FLOW PATTERN AT NEAR SURGE FLOW & M <sub>U</sub> =0.69	
FIGURE 6.10 FLOW PATTERN AT NEAR CHOKE FLOW & M <sub>U</sub> =0.69	
Figure 6.11 Flow from leading edge pattern at design flow & $M_{\text{U}}$ =0.69	
Figure 6.12 Flow from leading edge at near surge flow & $M_U$ =0.69	
Figure 6.13 Flow from leading edge at near choke flow & $M_U$ =0.69	134
FIGURE 6.14 LSVD5 <sup>+2</sup> FOR NEAR CHOKE FLOW AT M <sub>U</sub> =0.69	135
FIGURE 6.15 LSVD5 <sup>+2</sup> FOR NEAR SURGE FLOW AT M <sub>U</sub> =0.69	136
FIGURE 6.16 LSVD5 <sup>-2</sup> FOR NEAR CHOKE FLOW AT M <sub>U</sub> =0.69	
FIGURE 6.17 LSVD5 <sup>-2</sup> FOR NEAR SURGE FLOW AT M <sub>U</sub> =0.69	
FIGURE 6.18 THE FIRST DIFFUSER EFFICIENCY	
FIGURE 6.19 THE SECOND DIFFUSER EFFICIENCY	
FIGURE A.1 H-S DIAGRAM IN A DIFFUSER	144

#### **NOMENCLATURE**

b passage width from hub to shroud

C absolute velocity

c<sub>p</sub> specific heat at constant pressure

Cp pressure recovery  $Cp_{16} = (P_6 - P_1)/(\frac{1}{2}\rho_1 U_2^2)$ 

CVND conventional vaned diffuser

i incidence angle

LSVD low solidity vaned diffuser

M Mach number

M<sub>u</sub> impeller tip Mach number

P pressure, pitch

PS pressure side

r radius

SS suction side

s pitch

T temperature

U<sub>2</sub> impeller tip speed

VNL vaneless diffuser

Z vane number

z axial coordinate

α flow angle with respect to tangent

 $\beta$  vane angle with respect to tangent

 $\phi \qquad \text{inlet flow coefficient} \quad \phi = \dot{m} / \left( \rho_1 U_2 \frac{\pi d_2^2}{4} \right)$ 

γ ratio of specific heats

 $\eta = \frac{h_{06s} - h_{01}}{h_{06} - h_{01}} \cong \left( \left( \pi_{0.16} \right)^{\gamma} / \gamma - 1 - 1 \right) / \left( \tau_{0.16} - 1 \right)$ 

 $\mu \qquad \text{work coefficient} \qquad \mu = \frac{c_p (T_{06} - T_{01})}{\frac{1}{2}U_2^2}$ 

 $\pi$  pressure ratio  $\pi_{0.16} = P_{06}/P_{01}$ 

 $\theta$  blade turning angle

ρ density

 $\tau$  temperature ratio  $\tau_{0.16} = T_{06}/T_{01}$ 

σ solidity

 $\xi = (P_{03} - P_{06})/(\frac{1}{2}\rho_1 U_2^2)$ 

 $\psi \qquad \text{head coefficient} \qquad \psi = \Delta h_{0s} / (\frac{1}{2}U_2^2) \cong c_p T_{01} \left[ (\pi_{0, stage})^{(r-\frac{1}{2})} - 1 \right] / \frac{2}{2}U_2^2$ 

## **Subscripts**

0 total condition

1 stage inlet

2 impeller exit

2a impeller exit - measurement station

3 vane leading edge station based on LSVD

4 vane trailing edge station based on LSVD

5 diffuser exit

6 stage exit

c compressor stage

r radial component

s isentropic

t-t total-to-total

t-s total-to-static

u circumferential component

z axial component

## 1. INTRODUCTION

## 1.1. Centrifugal Compressors and Demands on Them

A turbomachine is a device which adds energy to a fluid (pump, compressor) or extracts energy out of it (turbine) by means of fast-moving blade. In the cylindrical coordinate system, the energy transfer through turbomachinery is governed by the rate of change of the angular momentum (UCu). The function of turbomachinery involves the exchange of significant levels of kinetic energy. Among turbomachinery, a pump uses liquids for a working fluid, while a compressor uses gases. For a compressor, three

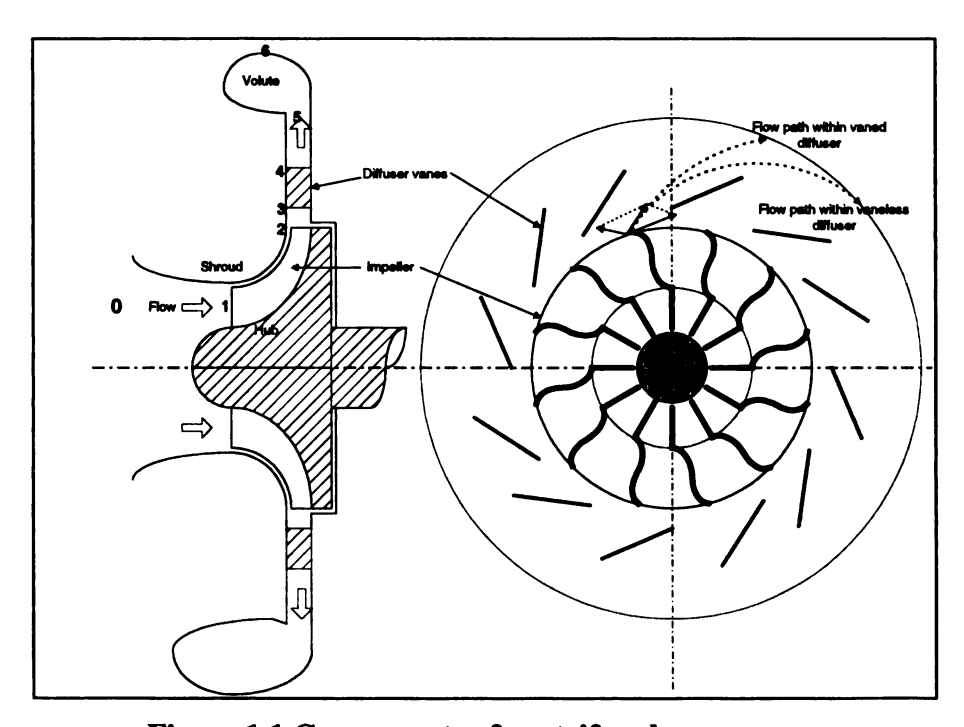


Figure 1.1 Components of centrifugal compressor

different terms (a fan, a blower, and a compressor) may be used depending on the pressure ratio or the pressure rise achieved. Furthermore, depending on the discharge flow direction, a compressor can be classified as axial, centrifugal (or radial), or mixed flow.

The centrifugal compressor, shown in Figure 1.1, is made up from four basic components: (1) a stationary inlet casing, (2) a rotating impeller, (3) a stationary diffuser of the vaneless or vaned type, and (4) the collector or volute.

The contribution of each component of the compressor is shown in Figure 1.2. The fluid is drawn in through the inlet casing into the eye of the impeller parallel to the axis of rotation. In order to add angular momentum, the impeller whirls the fluid outwards and turns it into a direction perpendicular to the rotation axis. As a result, the energy level is increased, resulting in both higher pressure and velocity. The purpose of the following diffuser is to convert some of the kinetic energy of the fluid into static pressure. Outside the diffuser is a scroll or volute whose function is to collect the flow

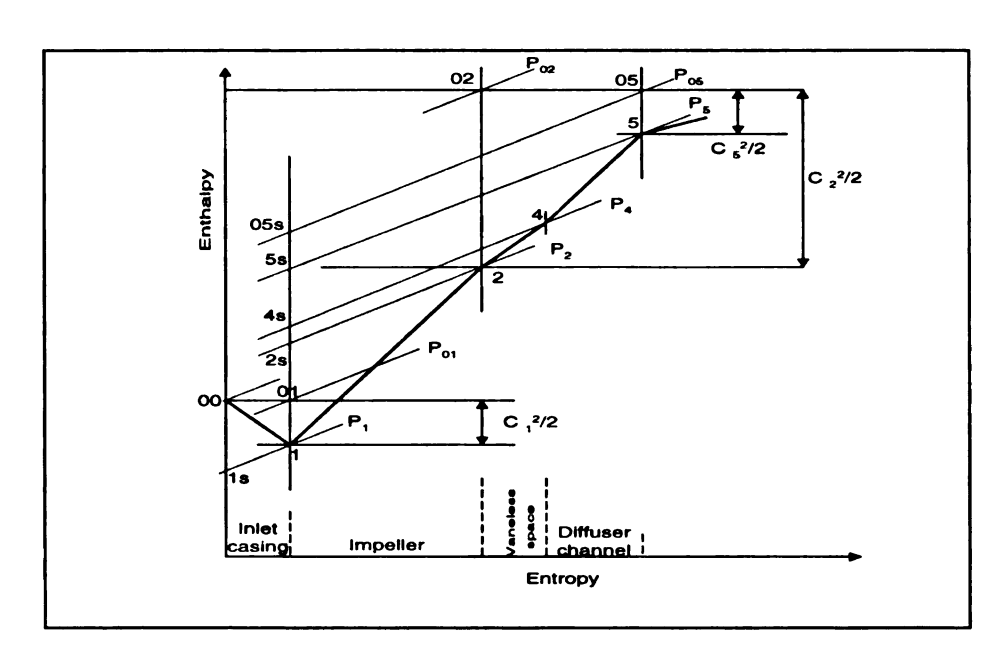


Figure 1.2 h-s diagram for the centrifugal compressor stage

from the diffuser and deliver it to the discharge pipe. It is possible to gain a further deceleration and thereby an additional pressure rise.

Because of the advantages of higher-single stage pressure ratio and the wider stable operating range over axial compressors the centrifugal compressor has been widely used. Centrifugal compressors are found in small gas turbine engines, turbochargers, and refrigeration systems, and are used extensively in the petrochemical and process industry. The other advantages of centrifugal compressors are that they are reliable, compact, and robust; have better resistance to foreign objects; and are less affected by performance degradation due to fouling.

This wide range of demands on centrifugal compressors brings many design considerations. Most of the design requirements need solutions to two major problems: stress and aerodynamics. The stress problems are caused by the material strength limitations and the capability to accurately predict blade and impeller steady state and vibrational stress for complex impeller shapes and at high rotational speeds. The aerodynamic problem is to efficiently accomplish large air deflections and diffusion at high flow velocity, with the added difficulty of very small passage flow areas required to get good efficiency and high pressure ratio. Even though the individual components of the compressor are capable of achieving high efficiency, it is the efficiency of the whole stage that is of great importance. Thus, component matching is an essential aspect of design. It is often required to redesign one or more components of the compressor due to improper matching and sometimes the efficiency of a component is sacrificed to achieve good matching.

#### 1.2. The Impeller

The impeller is the rotating component of the centrifugal compressor stage, where energy transfer of the compressor stage occurs.

$$\Delta h_{0c} = h_{05} - h_{01} = h_{02} - h_{01} \tag{1-1}$$

The specific energy transfer can be derived from the velocity triangle at inlet and outlet from the impeller (Figure 1.3). The rate of change of angular momentum will equal the sum of the moments of the external forces, TQ. When applied angular momentum theorem to an impeller, the torque, TQ, is given by

$$TQ = m(r_2C_{u2} - r_1C_{u1})$$
 (1-2)

The energy transfer is given by the product of angular velocity and the torque, given by the *Euler equation* 

$$m\Delta h_{0c} = -W = \omega TQ = m(U_2 C_{u2} - U_1 C_{u1})$$
 (1-3)

Applying the law of trigonometry to the velocity triangles of exit and inlet of the impeller yields

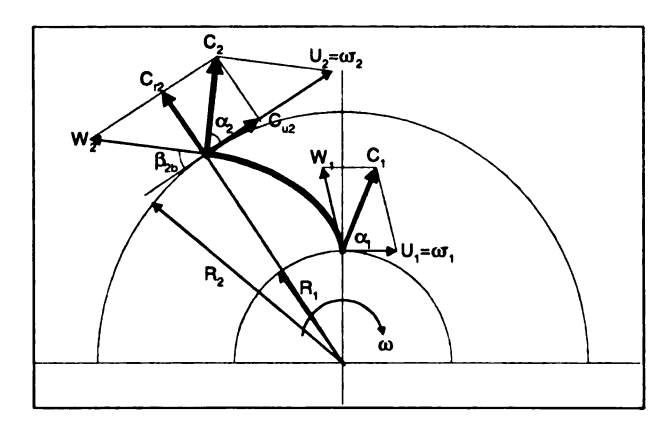


Figure 1.3 Velocity triangles for an idealized impeller

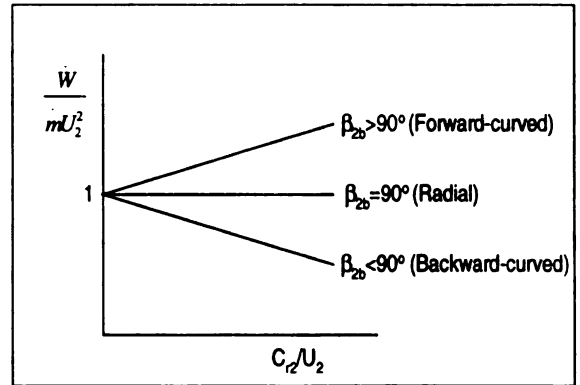


Figure 1.1 Effect of the impeller exit blade angle

$$U_2C_{u2} = \frac{1}{2}(U_2^2 + C_2^2 - W_2^2)$$
 (1-4)

$$U_1 C_{u1} = \frac{1}{2} (U_1^2 + C_1^2 - W_1^2)$$
 (1-5)

Combining (1-3), (1-4), and (1-5) results in the enthalpy rise in terms of velocity relations

$$\Delta h_{oc} = \frac{1}{2} \left[ (U_2^2 - U_1^2) + (W_1^2 - W_2^2) + (C_2^2 - C_1^2) \right]$$
 (1-6)

The sum of the first and the second terms on the right hand side represents the increase in static pressure and the kinetic energy increase is shown in the last term. In an axial compressor machine, there is no impeller tip speed variation ( $U_2 = U_1 = \text{constant}$ ) explaining a higher enthalpy rise in a radial compressor.

If we neglect inlet angular momentum, which is generally acceptable, the theoretical enthalpy reduces to

$$\Delta h_{0c} = \frac{\dot{W}}{m} = U_2 C_{u2} \tag{1-7}$$

Then the effect of impeller exit blade angle,  $\beta_{2b}$  on the theoretical enthalpy rise becomes

$$\frac{W}{m} = U_2^2 (1 - \frac{C_{r2}}{U_2} \cot \beta_{2b})$$
 (1-8)

For a given value of impeller exit blade angle,  $\beta_{2b}$  there is a linear relationship between specific energy transfer and flow rate (Figure 1.1). Theoretical enthalpy of impeller backward-curved blades decreases as the flow rate increases while that of

impeller with the radial blades remains constant The positive-slope condition can be unstable and cause surge. For this reason a backward-curved blade impeller is generally preferred.

#### 1.3. The Radial Diffuser

Diffusion occurs where velocity reduction occurs. Velocity is a vector quantity having both magnitude and direction. In other words, diffusion can occur on an isolated surface or in a duct.

In centrifugal compressors, energy is transferred to the fluid by the impeller. Even though centrifugal impellers are designed for good diffusion within the blade passage, approximately half of the energy imparted to the fluid remains as kinetic energy at the impeller exit. Therefore, for an efficient centrifugal stage, this kinetic energy must be efficiently converted into the static pressure. Thus, a diffuser, which is stationary and is located downstream of the impeller, is a very important component in a centrifugal compressor.

Since over the years the demands on the centrifugal compressors increased for higher pressure ratios and efficiency, different types of radial diffusers have been developed. These different types of radial diffusers can be classified as the vaneless diffusers, the vaned diffusers, and the low solidity vaned diffusers.

#### 1.3.1. Vaneless Diffusers

Vaneless diffusers consist of two radial walls that may be parallel, diverging, or converging. The flow entering a vaneless diffuser has a large amount of swirl; the swirl

angle ( $\alpha = \tan^{-1}(C_r/C_u)$ ) is typically between 10° - 30°. Thus, the tangential component of momentum at low flow rates can be more than twice the radial component. The radial component of the flow diffuses due to the area increase (conservation of mass), and the tangential component diffuses inversely proportional to the radius (conservation of angular momentum). However, the radial component has to surmount the radial pressure gradient for the tangential component to diffuse continuously. When reverse flow of the radial boundary layer occurs, it is not possible for the tangential component to continue diffusing, as this would imply a pressure increase in one component and not in the other. Therefore, in such cases the breakdown of flow occurs, and this can cause the diffuser to stall and produce other flow instabilities such as surge or stall. However, backflow into the impeller is less frequent with vaneless diffusers than with vaned diffusers where local pressure disturbs caused by vane pressure loading.

The vanelsess diffuser is widely used in automotive turbochargers because of the broad operating range it offers. It is also cheaper to manufacture and more tolerant to erosion and fouling than the vaned diffusers. However, the vaneless diffuser needs a large diameter ratio because of its low diffusion ratio. The flow in a vaneless diffuser follows an approximate logarithmic spiral path. The flow in a vaneless diffuser with a radius ratio of 2 and an inlet flow angle of 6° makes a full revolution before leaving the diffuser. This will result in high friction loss due to viscous drag on the walls and accordingly its pressure recovery is significantly lower than is found with vaned diffusers.

Generally the vaneless diffuser demonstrates lower pressure recovery by as much as 20% and lower stage efficiency by 10% compared to a vaned diffuser.

#### 1.3.2. Vaned Diffusers

The role of the vane in a vaned diffuser is to shorten the flow path by deswirling the flow, allowing a smaller outlet diameter to be used. A vaneless space precedes the vaned diffuser to help reduce flow unsteadiness and Mach number at the leading edge of the vanes so as to avoid shock waves. Boundary layer develops and generates appreciable blockage at the vane leading edge. In order to reduce this blockage, the vaneless space should be minimized until it doesn't give any unfavorable effects such as increase in noise level or pressure fluctuations due to interaction of the impeller and diffuser. The flow exiting the impeller follows an approximate logarithmic spiral path to the vane leading edge and is guided by the diffuser channels. The semi-vaneless space follows the vaneless space, ending in a passage throat, which may limit the maximum flow rate in a compressor. The number of diffuser vanes has a direct bearing on the efficiency. With large number of vanes, the angle of divergence is smaller and the efficiency rises until friction and blockage overcomes the advantage of more gradual diffusion.

Although the vaned diffuser typically exhibits higher pressure recovery, the flow range is limited at low flow rate due to vane stall. At high flow rates, flow choking at the throat may also limit flow range.

The major feature of the low solidity vaned diffuser is the absence of a geometric throat which limits flow range of the centrifugal compressor with the vaned diffusers. The low solidity vaned diffusers exhibit high efficiency comparable to conventional vaned diffusers, while holding flow range levels approaching that of vaneless diffusers.

In order to show the variety of vaned diffusers with respect to vane shape, different types of vaned diffuser are listed and described in Figure 1.5.

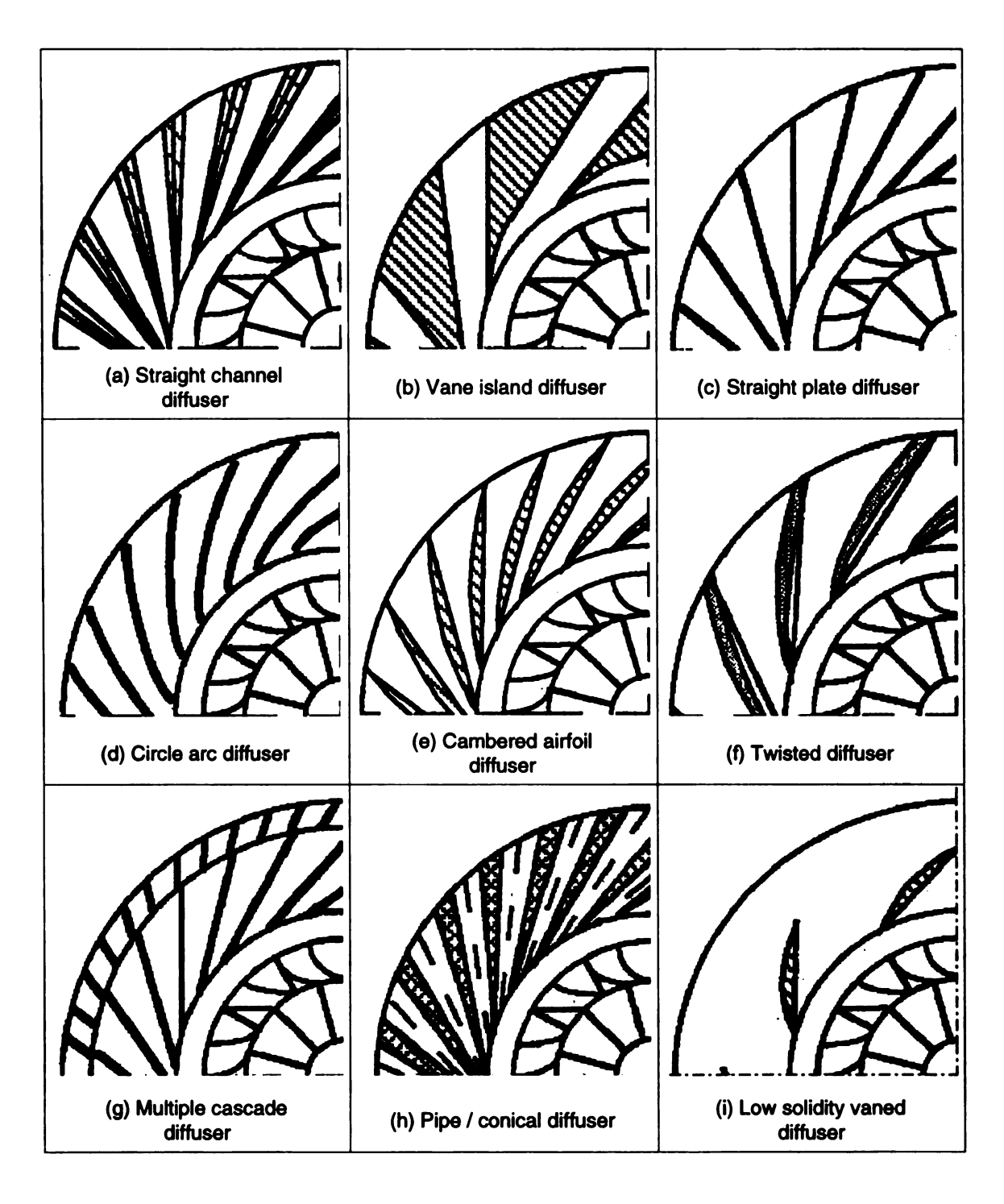


Figure 1.5 Types of vaned diffusers

#### Straight Channel / Wedge Diffuser

The simple geometry of this kind of diffuser enables an easy manufacturing process; and, thus, it is one of the most popular types. Nevertheless, it is large in size.

#### Vane Island Diffuser

The vane island diffuser is basically a refined straight channel diffuser used for high pressure ratios and transonic inlet Mach numbers. It is also large in size, but the number of vanes is very small. To improve the flow conditions, the inlet is curved at the suction side. In total, this leads to a good pressure recovery.

#### Straight Plate Diffuser

Typically, the straight plate diffuser has a large number of vanes(Z>30), and the pressure recovery is not very good. Its merit is rather cheap manufacturing process due to the simple geometry. A chamfered pressure side leading edge might be used to improve incidence matching in the severe initial diffusion rate.

#### Circular Arc Diffuser

Since the geometry is simple and the ends of the vanes are not profiled except a sharpening, the circular arc diffuser can be manufactured easily. It doesn't show any outstanding aerodynamic characteristic.

#### Cambered Airfoil Diffuser

The cambered airfoil diffuser, which is used for both transonic and subsonic flow, is often designed on the base of data from axial cascades.

#### Twisted Diffuser

The peculiarity of the refined cambered vanes is their 3-dimensional twisted shape that matches to the flow. A good efficiency, a wide range and a high pressure recovery are obtained.

### Multiple Cascade Diffuser

As the manufacturing process grows with additional cascades, cambered vanes are usually chosen to reduce the expenses. The advantages are a higher efficiency and a reduced risk of separation due to the higher number of vanes at the increased radii.

#### Pipe / Conical Diffuser

The pipe diffuser is used for higher pressure ratios and transonic applications. The pressure recovery is good compared to the channel diffuser. The circular cross section of the drillings is considered to allow these diffusers to swallow a highly non-uniform flow much better than the 2-dimensional cascade type. Also it is economic because of simple geometry definition and easy manufacturing process required.

### Low Solidity Vaned Diffuser

This diffuser is often used for low flow coefficient compressors and gains a good pressure recovery in combination with a wide operation range.

#### 1.4. Objective of the Present Work

One of the critical problems in the design of the centrifugal compressor is the diffusion of a high level of kinetic energy entering the radial diffuser. An adverse pressure

gradient thickens the boundary layer at the wall resulting in flow separation if the pressure gradient becomes excessive.

A centrifugal compressor stage can have an overall efficiency as high as 85± 2% in the pressure ratio range of 2 to 6. For such a compressor, if operating at favorable condition, the diffuser efficiency can be about 75 to 85%, while the impeller efficiency can be above 90%, which is a remarkably high value in view of the large energy added. It compares well with the best transonic and supersonic axial compressor rotors that add much lower energy per stage. However, at off-design flows the diffuser efficiency drops rapidly while the impeller efficiency remains almost constant.

The high impeller performance has been achieved within the confines of mechanical limitations that permit very little variation in the blade or rotor design. Thus, it can be said that improvement in radial impeller efficiency can only be incremental and will require a very significant amount of development effort.

Therefore diffuser improvement offers a more promising approach to better compressor performance than does the impeller. Moreover, a diffuser is much less restricted by the mechanical limitations when compared to the impeller of a centrifugal compressor. If the radial diffuser efficiency of 85 to 90% can be attained, an improvement of 4 to 5 percentage points in overall efficiency of the centrifugal compressor can be achieved.

It has been possible to obtain high diffuser efficiency (up to 85%) with the help of specifically designed vaned diffusers. But the major disadvantage of the vaned diffusers is that they limit the range of operation of the compressor. In this work the vaned diffuser design has been studied in detail with a view to understand all the parameters that help in

attaining high efficiency. At the same time to identify the parameters, which restrict the flow range of the compressor as wide flow, range is very important for most compressor applications.

It is well known that the low solidity vaned diffusers have significant advantage over both the vaneless and the conventional vaned diffusers because they are able to attain efficiency competitive with vaned diffusers and an operating range approaching that of vaneless diffusers. Interest has recently increased in the use of low solidity vaned diffusers for industrial centrifugal compressors. The compressor industry has been designing and testing the low solidity vaned diffusers over the last sixteen years. Nonetheless, the important design parameters and their effects on performance are not well established. For this reason, continued research is required to establish better design procedures and to better define the range of applications.

In this work, the low solidity vaned diffusers were designed, manufactured, experimentally tested and analyzed numerically using 3-D viscous Navier-Stokes code to understand the influence of vital aerodynamic and geometric parameters on the flow phenomena.

The four new low solidity vaned diffusers along with one conventional vaned diffuser and two vaneless diffusers were tested downstream of the same impeller at Michigan State University's Turbomachinery Laboratory.

This work contains the results of those tests. The overall steady performance of the compressor with the different diffusers was compared with the results obtained by 3-D viscous Navier-Stokes code simulation. The influence of the geometric design

parameters on the flow was investigated through numerical simulation. Besides steady performance analysis, unsteady performance analysis has been carried out.

The main objective of this work is to contribute to the design methodology and performance assessment of low solidity vaned diffuser by:

- Designing and testing four LSVDs,
- Understanding their steady and unsteady performance,
- Numerically validating the experimental data,
- Determining the influence and effect of both the geometric and aerodynamic parameters of LSVD on its performance,
- Numerically predicting the influence and effect of both the geometric and aerodynamic parameters of the LSVD on its performance for configurations where experimental testing was not performed.

## 2. THE CENTRIFUGAL COMPRESSOR

## 2.1. Steady Flow of a Centrifugal Compressor

## 2.1.1. Flow Between Impeller and Diffuser

Centrifugal compressor stage optimization requires a proper impeller/diffuser matching, as this has considerable influence on the efficiency and stability of the stage. For a good stage performance, the efficiency of the impeller and the diffuser are of equal importance. However, the efficiencies of both these components are interdependent due to the impeller/diffuser interaction.

The impeller flow is strongly affected by three-dimensional boundary layers,

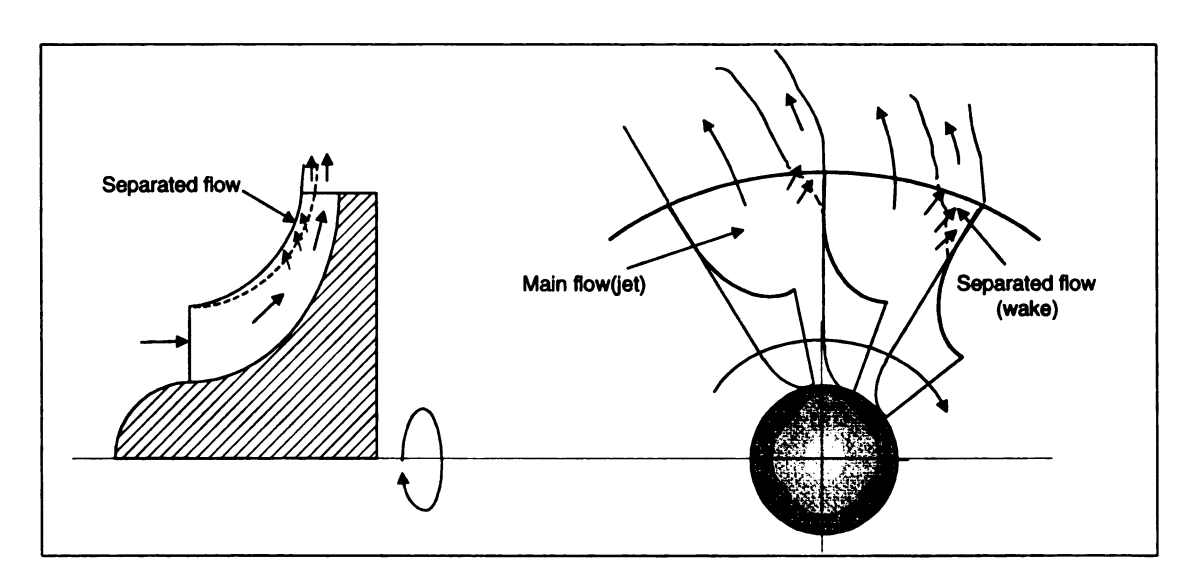


Figure 2.1 Jet-Wake flow pattern of impeller discharging flow

secondary flows, and flow separation. Thus, the flow discharged from the impeller is mostly often highly non-uniform with significant three-dimensional velocity components exhibiting jet/wake flow pattern. Jet/wake flow patterns are generated by Coriolis force, curvature, boundary layer, and tip clearance effects that separate the flow into high (jet) and low (wake) velocity fluid. Turning of the flow from axial to radial direction generates secondary flow, which drives low momentum fluid to the shroud. Once the flow has separated on the suction side the separated flow region in the meridional plane rapidly grows toward the hub surface. The pressure gradient from pressure side to suction side (blade-to-blade) also influences the secondary flow driving low momentum fluid toward the suction side.

The diffuser pressure recovery is largely affected by the highly distorted, unsteady impeller discharge flow. On the other hand, the diffuser vanes are believed to act on the internal three-dimensional impeller flows. The non-uniform flow from the impeller is sensed as an unsteady flow by the vaned diffuser vanes, while the presence of diffuser vanes is seen as an unsteady disturbance by the impeller. Moreover, this interaction between the impeller and diffuser vanes is a strong source of noise and vibrational excitation.

The interaction between the impeller and diffuser flow is one of the critical problems in design of highly loaded centrifugal compressors. The diffuser has to remove these non-uniformities in velocity and flow direction so as to efficiently recover the static pressure.

Many investigators have studied the jet/wake flow behavior at the impeller exit, in order to understand the various effects contributing to this kind of flow. And also many

investigations have been carried out on the interaction of the impeller and the diffuser vanes on the impeller discharge flow how jet and wake mix in the vaneless space or diffuser downstream of the impeller.

Eckardt (1975) performed detailed measurements in the impeller discharge mixing zone for a radial type impeller running at tip speed of 300m/s by high frequency measuring system. From the measured relative velocity distribution behind the impeller (Figure 2.2) he showed a region with high radial flow component near the pressure side having relatively stable flow and low total pressure losses and a region near suction side/shroud corner with low mass flow, high turbulence and losses. Thus, he showed the jet-wake flow exiting the impeller. Similar measurements in the vaneless space following the impeller up to a radius ratio of r/r<sub>2</sub>=1.089 showed that the jet and wake have not mixed completely and the flow is not axisymmetric.

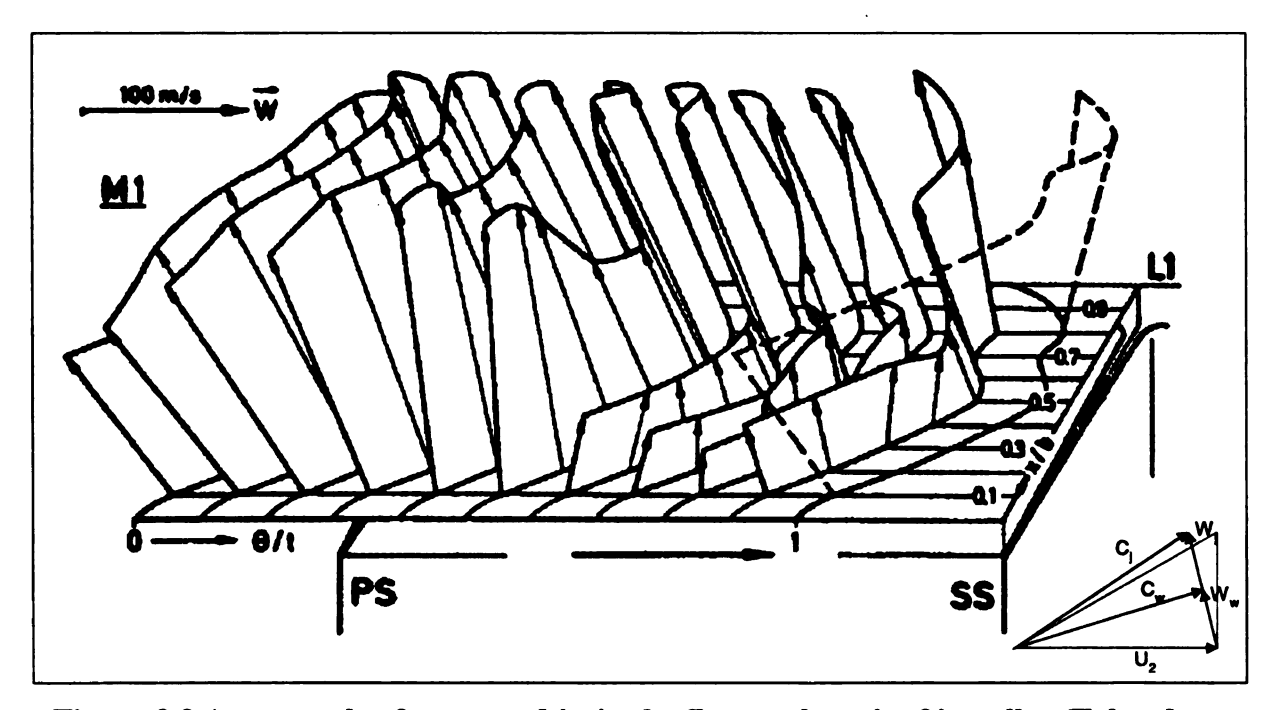


Figure 2.2 An example of measured jet/wake flow at the exit of impeller (Eckardt, 1975)

Baghdadi (1977) studied the effect of impeller blade wakes on the performance of the vaned diffuser by using a vortex rig. The vortex rig could produce only the axial distortions in the flow at diffuser inlet. Thus, he could compare the results of vortex rig with the results of an actual compressor to examine the effect of impeller blade wakes. He found close agreement in the performance of the vaned diffusers used with the vortex rig and the actual compressor. Therefore, he concluded that the impeller blade wakes do not significantly affect diffuser performance. The reason for this could be that the blade wakes mix very rapidly by energy transfer or due to the lack of response of the diffuser vanes to the high frequency flow variations imposed by the rotating wakes.

Johnson and Moore (1980, 1982, 1983), using a ghost impeller similar to the Eckardt's impeller, measured the three mutually perpendicular velocity components and rotary stagnation pressure to study the wake formation and development. They found that the wake flow was an accumulation of low rotary stagnation pressure fluid at the suction side/shroud corner of the impeller blade passage and that the turbulent mixing associated with the shroud boundary layer separation and the strength of the secondary flow strongly influence the size and location of the wake, respectively. The major flow phenomena contributing to the formation and development of the wake were:

- (a) The adverse static pressure gradient between the inlet and the exit of the axial to radial bend in the impeller near the shroud/suction side corner, which results in a substantial increase in low stagnation pressure fluid at the inlet region of the bend, and
- (b) The convection of low stagnation pressure fluid by the secondary flows, which are generated in the boundary layer due to the curvature and rotation of the impeller passage.

They also showed that the mass flow rate had an influence on the location of the wake at the impeller outlet; the wake was located on the suction surface for below design flows, near the suction surface/shroud corner at design flow and on the shroud at above design flows. Since the secondary flows are a function of mass flow rate, they showed that the secondary flows in the impeller passage contribute to the formation of the wake and that they also have strong influence on the position of the wake at the impeller exit plane.

Krain (1981) performed L2F measurements both inside the impeller (near the exit) and in the diffuser with a vaneless and a vaned diffuser downstream of the impeller. The diffuser blades have a slight effect on the velocity profiles at the shroud, whereas the velocity patterns at the hub region were similar with both diffusers. The small effect of the diffuser vanes on the impeller flow was presumed to be due to high vane leading edge to impeller exit radius ratio of 1.1. However, the measurements in the vaneless space of the vaned diffuser showed unsteady flow angle variations of up to 17°, and up to 13° in the diffuser throat region. Thus, there does not exist any station ahead of the diffuser throat where flow is fully mixed out.

Krain (1988) studied the flow behavior in three different types of centrifugal impellers. The impellers tested were (a) radially ending Eckardt impeller, (b) radially ending splitter blade impeller (14 + 14 blades) and (c) new backswept impeller. He concluded that the secondary flows and distorted throughflows found in all three impellers were caused by the swirling impeller flow inside the impeller. Moreover, he found that the vortex flow had influence on the throughflow patterns, thus, it was

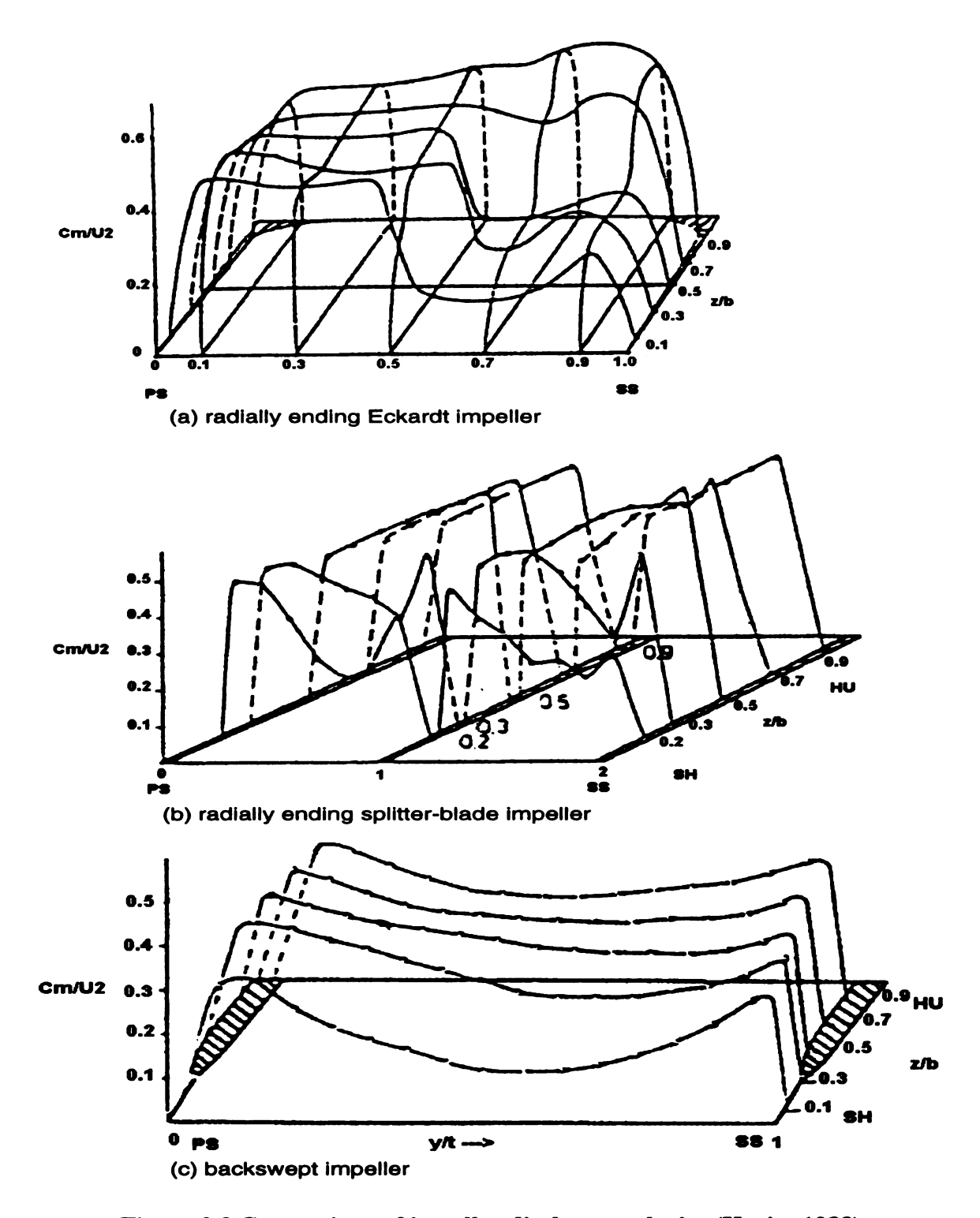


Figure 2.3 Comparison of impeller discharge velocity (Krain, 1988)

impossible to avoid distorted impeller discharge flow, unless the flow development is guided in such a way that the vortex flow fully disappeared at the impeller discharge.

Fisher and Inoue (1981) found that the vaned diffuser played a major role in establishing the circumferential variations in the mean flow conditions at the impeller exit. They observed that by increasing the blade angle, the circumferential variations increased. However, an increase in the number of diffuser vanes decreased the variation of the flow conditions in the circumferential direction. They also found that the vane setting radius had a major effect on the flow conditions. Figure 2.4 shows the velocity variation in circumferential direction for two different radial clearances between impeller tip and diffuser vanes (4% and 10% of  $r_2$ ).

Inoue and Cumpsty (1984) carried out hot-wire measurements in the vaneless space between the impeller and vaned diffuser at a range of flow coefficients for three different diffusers with 10, 20, and 30 vanes set at each of three different radius ratios, 1.04, 1.1, and 1.2. It was found that the circumferential distortion of flow from the impeller was very rapidly attenuated in the entrance region of the diffuser vanes and had only minor effects on the flow inside the vaned diffuser passages. The effect of the diffuser vanes on the flow discharge from the impeller was evident and reversal of the flow back into the impeller was detected when the diffuser vanes were close to the impeller and flow rate was low. The time mean total and static pressure at impeller outlet were found to vary over the pitch of a diffuser vane, and a variation in the strength of impeller wake was also observed. Inoue and Cumpsty (1984) in their work show that the angular velocity profile did not vary as significantly as the radial velocity across the span with radius. They also found that the circumferential distortions of the radial velocity in vaneless diffuser did not disappear even at  $r/r_2=1.3$ . However, the distortion patterns of

tangential velocity decreased rapidly with radius, which can be attributed to the energy transfer between jet and wake regions.

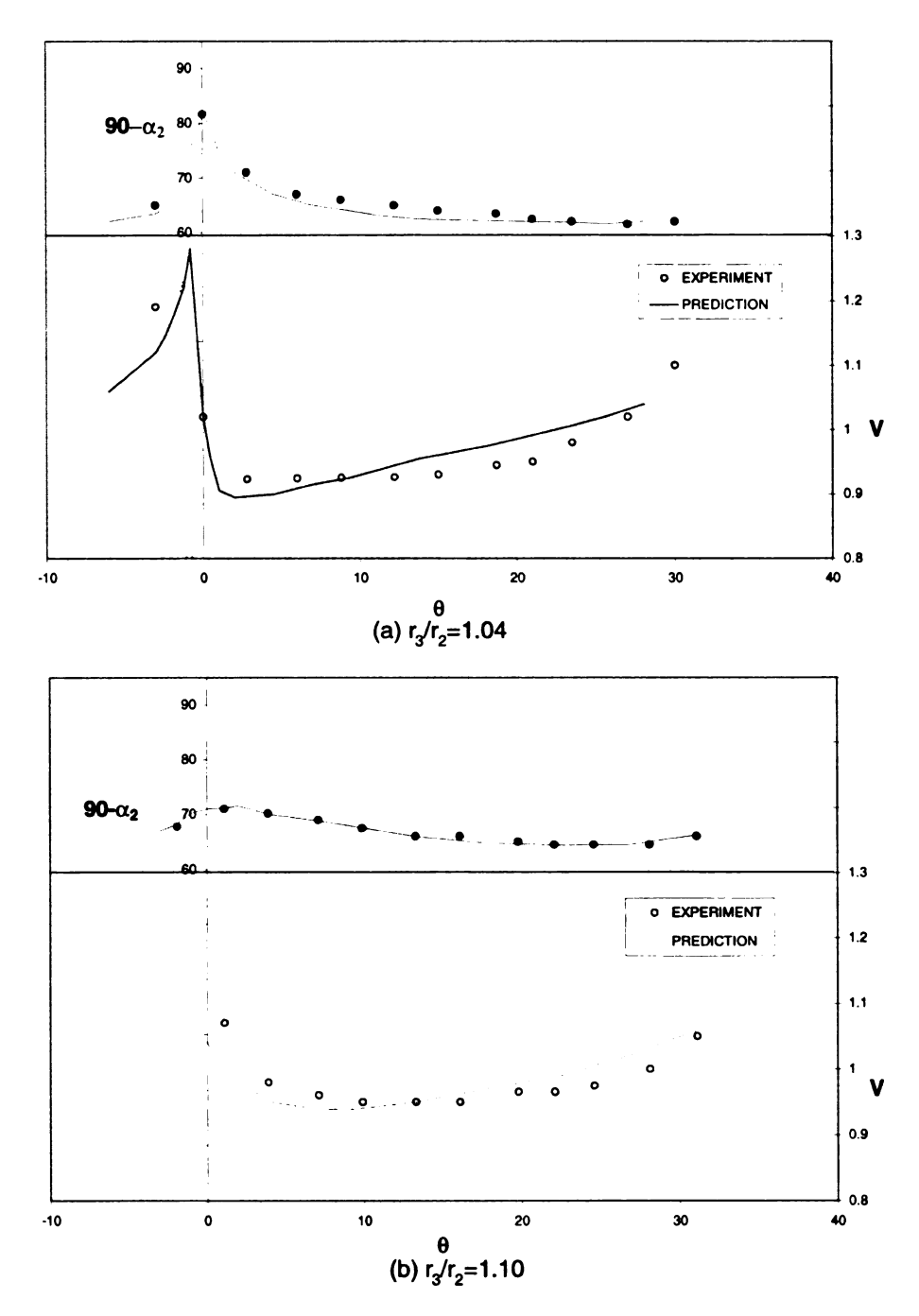


Figure 2.4 Traverse at diffuser inlet (Fisher et al., 1981)

Hathaway et al. (1993) studied flow field of the NASA low speed centrifugal compressor impeller using laser anemometry and 3D viscous code (Dawes code) in order to understand a detailed primary and secondary flow development within an unshrouded centrifugal compressor impeller. The results obtained by them were very similar to those of the Krain and others. In addition to this they also showed that 3D viscous code results were in good agreement with the experimental results. They also compared their results with the results of the Krain's impellers and found good agreement. They found that the low-momentum fluid near the blade surfaces migrates outward toward the blade tip. The fluid that moves up the blade pressure and suction surfaces is entrained into the tip clearance jet and the fluid is transported toward the pressure side/shroud corner of the characteristic throughflow momentum wake that is found in unshrouded centrifugal impellers. They also studied the impeller wake mixing phenomenon downstream of centrifugal impeller. They measured absolute flow angles at four different locations up to a r/r<sub>2</sub> of 1.065 and found that the throughflow momentum wake region generated as a result of tip clearance flow mixes out more slowly than does the viscous blade wake as the flow moves through the vaneless diffuser. This was concluded from the pitchwise absolute flow angle distribution study at 50% span and 90% span as shown in Figure 2.5. Thus, the flow field in the vaneless space near the shroud surface is composed of low momentum regions of the viscous blade wake and the throughflow momentum wake.

Pinarbasi and Johnson (1994) also showed very similar results through hot wire anemometer measurements at numerous radius locations in the vaneless diffuser downstream of a backswept impeller.

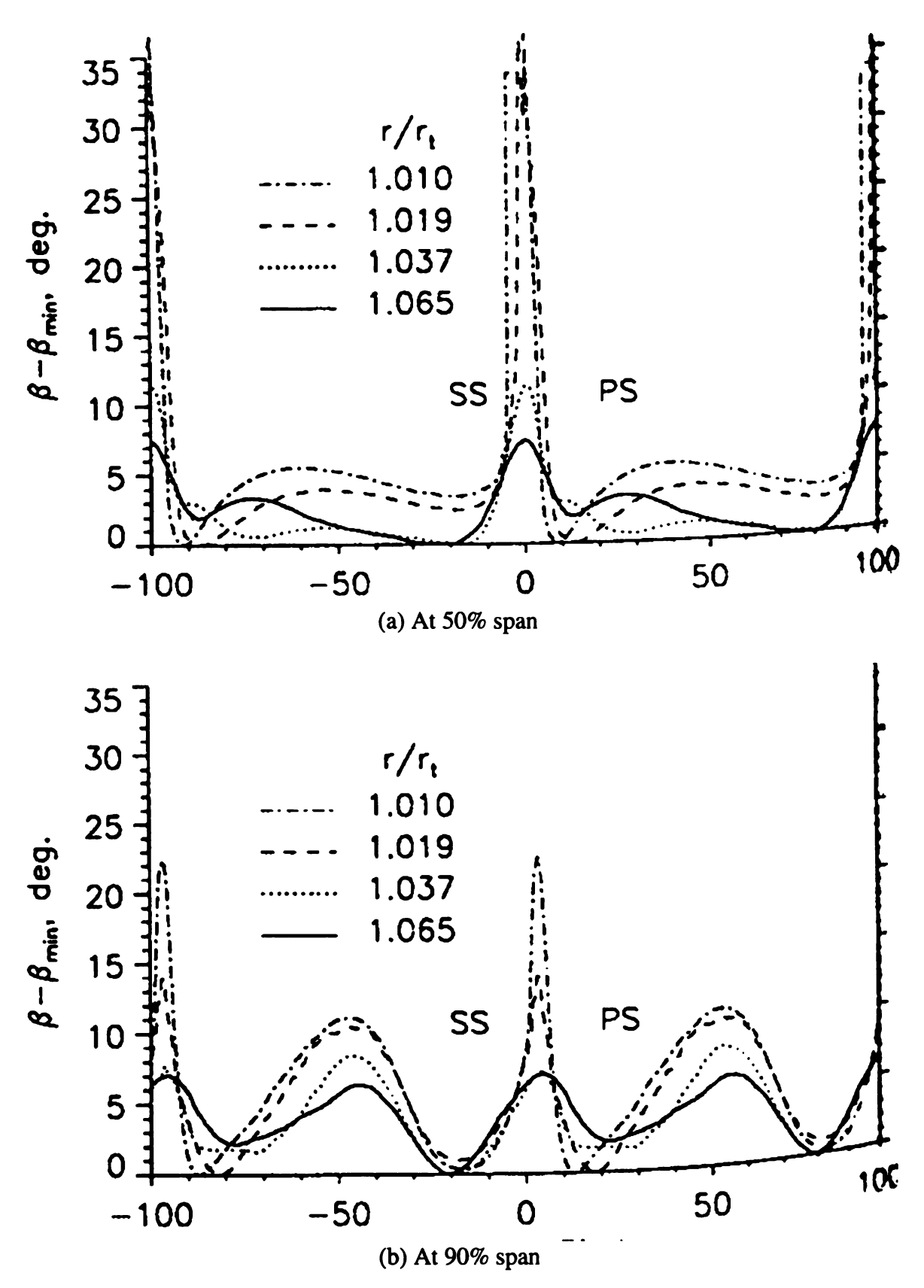


Figure 2.5 Pitchwise distribution of absolute flow angle difference at impeller exit (Hathaway et al., 1993)

Thus, the flow received by any diffuser downstream of a centrifugal compressor is very non-uniform and contains jet and wake flow patterns caused by the secondary flows inside the impeller blade passage. In the vaneless space downstream of the impeller, the dynamic variations and the flow distortions in the circumferential direction tend to mix out in short radial distance. However, the passage wakes and the flow variations in the axial direction across the span tend to persist through out the vaneless diffuser.

# 2.1.2. Diffuser Design Parameters

The performance of turbomachinery is dominated by diffusion. In most centrifugal compressors both the impeller and the diffuser are limited by the diffusion capabilities of the flow channels. The kinetic energy at the diffuser inlet easily amounts to 50 % of the total energy added by the impeller. An efficient transformation of this energy into pressure is therefore an important part of compressor design. A large part of aerodynamic losses in turbomachines is due to local or general areas of boundary layer separation resulting from local or general degree of diffusion that is too large for the boundary layer to overcome the unfavorable pressure gradient.

There are different groups of diffusers one can use to achieve an appropriate pressure rise.

### **2.1.2.1. 2-Dimensional Simple Diffusers**

Kline et al. (1959) have identified the significant flow regimes in straight-wall two-dimensional diffusers with thin turbulent inlet boundary layers and completed

stability map. They found that maximum pressure recovery occurred when a condition of transitory stall exists. From dimensional analysis, area ratio, divergence angle, inlet Reynolds number, inlet Mach Number, aspect ratio, and inlet blockage are the parameters affecting the diffuser performance (Figure 2.6).

Runstadler et al. (1969) performed the similar experiments as Kline et al. (1958) and showed the diffuser performance as a function of inlet Mach number, aspect ratio and blockage. They demonstrated that the single most important parameter governing the performance is the boundary layer blockage in the throat.

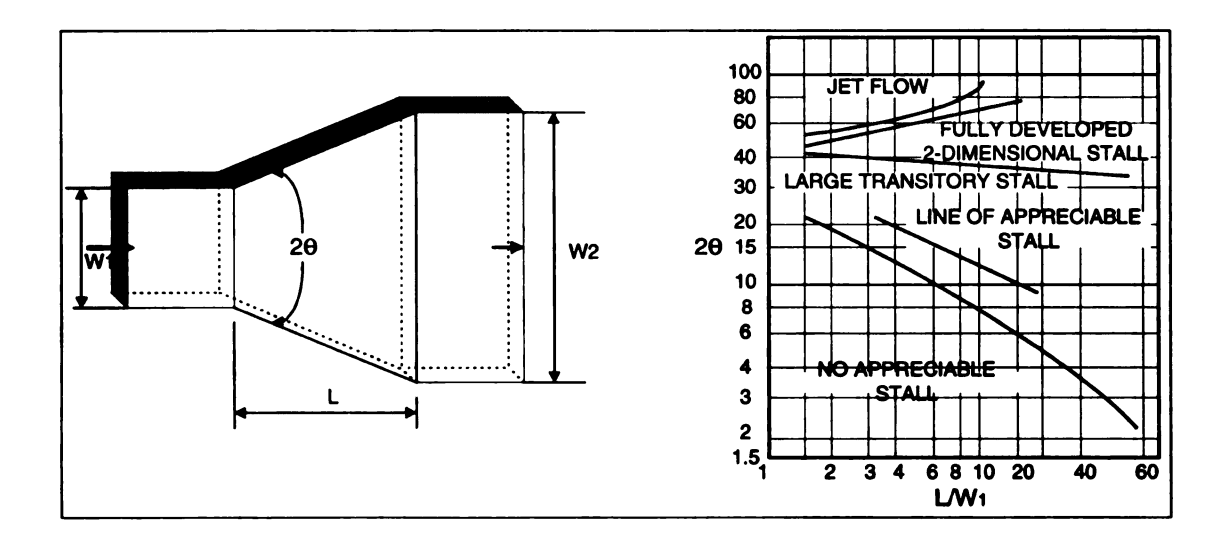


Figure 2.6 Flow regime in straight wall 2 dimensional diffusers (Kline et al., 1959)

Figure 2.7 shows the losses in a typical diffusing element versus the pressure recovery, which was developed using measured data for certain conical diffusers. The impacts of aerodynamic blockage as well as area ratio on diffuser performance are shown. High diffuser effectiveness requires attention to many geometric parameters and a limited

level of aerodynamic blockage. If a diffuser effectiveness of 90% is to be achieved, the inlet aerodynamic blockage should be under 3%. Pressure recoveries in actual turbomachinery are frequently on the order of 0.5 to 0.7 at the best efficiency point.

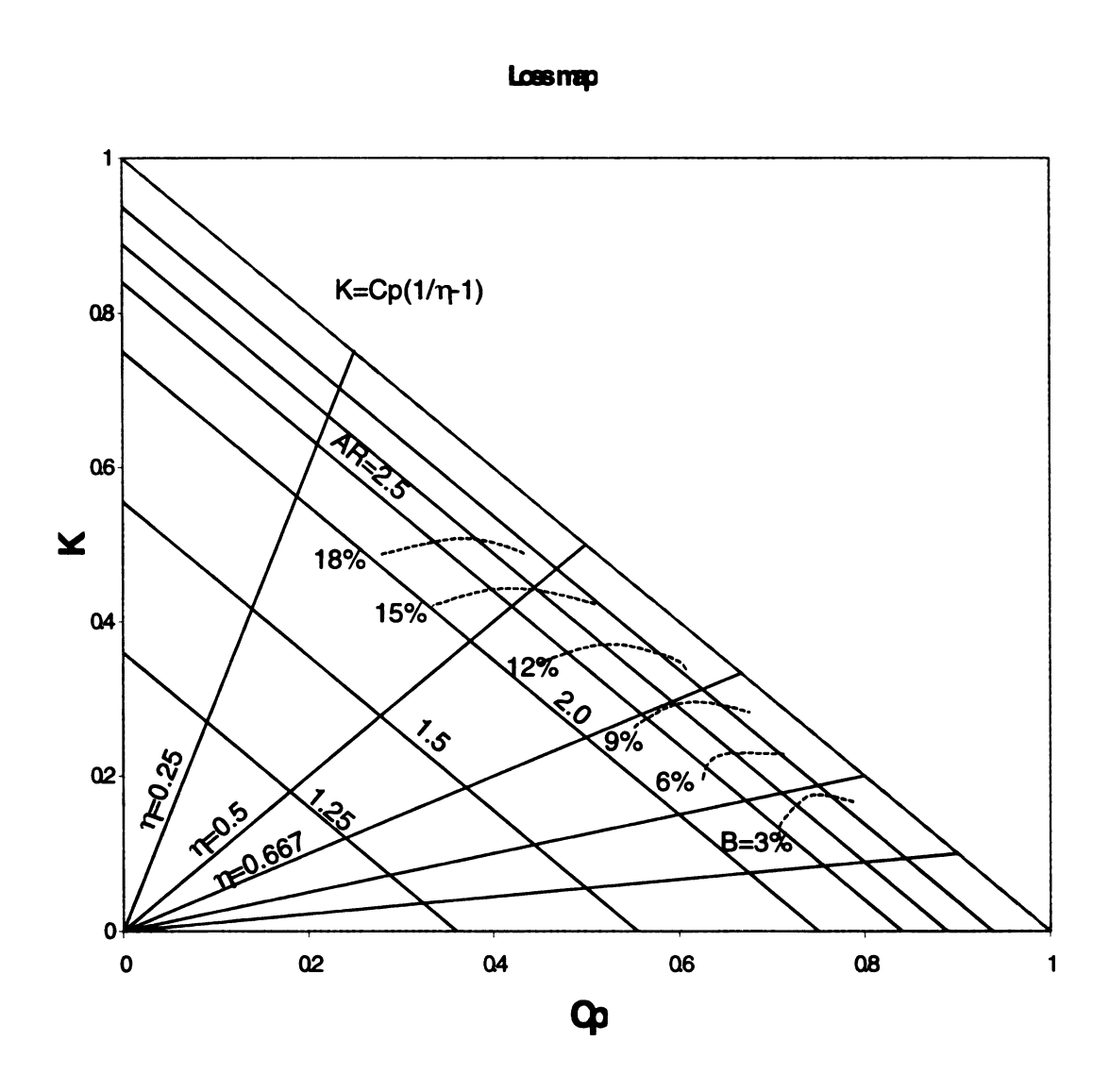


Figure 2.7 Loss map of a diffuser (Japikse, 1984)

#### 2.1.2.2. Vaneless Diffusers

In the vaneless diffuser diffusion is caused by an increasing radius by two radial walls. For an incompressible, inviscid fluid, the process of pressure recovery is described by the following equations. This forms the well-known logarithmic spiral flow path through the vaneless diffuser of constant depth ( $\alpha$ =constant).

$$\rho \cdot c_r \cdot 2\pi rb = \rho \cdot c_u \cdot 2\pi rb \tan \alpha = m \tag{2-1}$$

$$c_{u} \cdot r = const \tag{2-2}$$

However, for air, density varies with pressure and temperature and viscosity exists. Considering these effects, the governing equations are as follow:

$$\rho \cdot c_r \cdot 2\pi r b = \rho \cdot c_u \cdot 2\pi r b \tan \alpha = m \tag{2-3}$$

$$\frac{d}{dr}(rC_u)(\rho_2 C_{r1} 2\pi r_2 b_2) = 4\pi r^2 \tau_u$$
 (2-4)

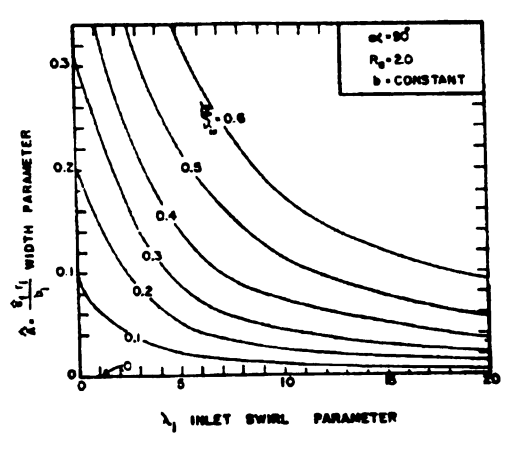
$$\frac{\rho}{r}C_u^2 - \rho C_r \frac{dC_r}{dr} = \frac{dP}{dr} - \frac{\tau_r}{b} \tag{2-5}$$

$$\tau_{u} = -c_{f} \frac{\rho}{2} CC_{u}$$

where,

$$\tau_r = -c_f \frac{\rho}{2} C C_r$$

The broader implications of the basic differential equations have been summarized in several characteristic plots by Johnson et al. (1965) as shown in Figure 2.8 and Figure 2.9. The primary independent parameters are inlet swirl ratio ( $\lambda_i = C_{u2} / C_{r2}$ )



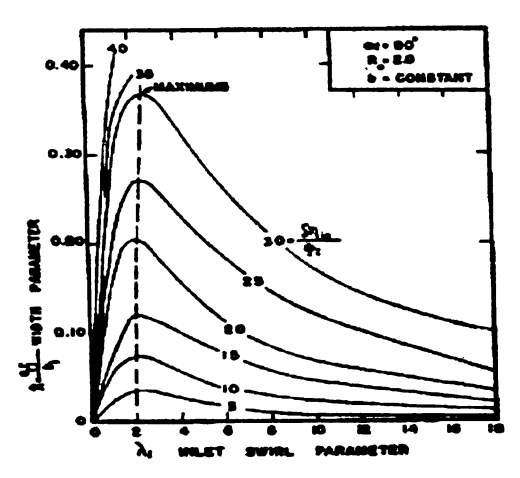


Figure 2.8 Contours of total pressure loss coefficient

Figure 2.9 Contours of loss of stage efficiency per unit work coefficient

and width parameter ( $\hat{A} = \hat{c}_f r_2 / b_2$ ), where the wall friction coefficient is adjusted so that the prediction agrees with the experimental results.

#### 2.1.2.3. Vaned Diffusers

Semivaneless space between the leading edge and the diffuser vane throat is the most important part of vaned diffusers because the inlet blockage factor is decided by it.

Yoshinaga et al. (1980) tested 16 different vaned diffusers in a compressor rig and compared with the data on the two-dimensional diffuser with the inlet blockage of 0.05. These test results showed that the pressure recovery increases up to a critical diffusion limit of 0.5 where diffusion ratio is defined as  $C_4/C_3$ .

Aungier (1988,1990) showed the systematic procedure for the design of vaned diffuser from an evaluation of experimental data for 18 different diffuser design. He made full use of blade loading to achieve maximum pressure recovery within the available space. Also he suggested a new linearized blade-to-blade flow analysis yielding accurate predictions for so simple a method.

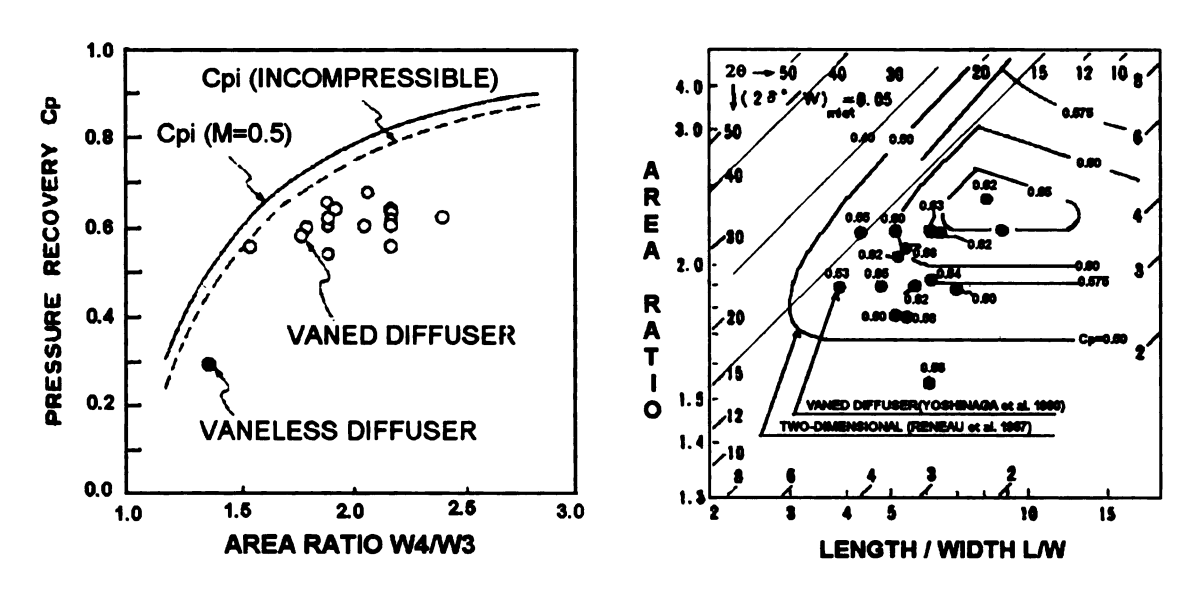


Figure 2.10 Performance of the vaned diffusers (Yoshinaga et al., 1980)

# 2.2. Instability of a Compressor Stage

Stability is defined with respect to the equilibrium operating condition in a system, where it tends to return to its equilibrium operating condition, if the system disturbed slightly. Beyond this point instability might happen locally with a component called "stall" or totally in a system called "surge".

Figure 2.11 is the numerically calculated flow in a 2-D channel diffuser which shows separated flow region due to excessive diffusion. The streaklines from the diffuser inlet are drawn in the upper part and the pressure contours lines and velocities are shown in the lower part. Boundary layer develops rapidly and separates at both walls due to excessive adverse pressure gradient. This condition is called as "diffuser stall".

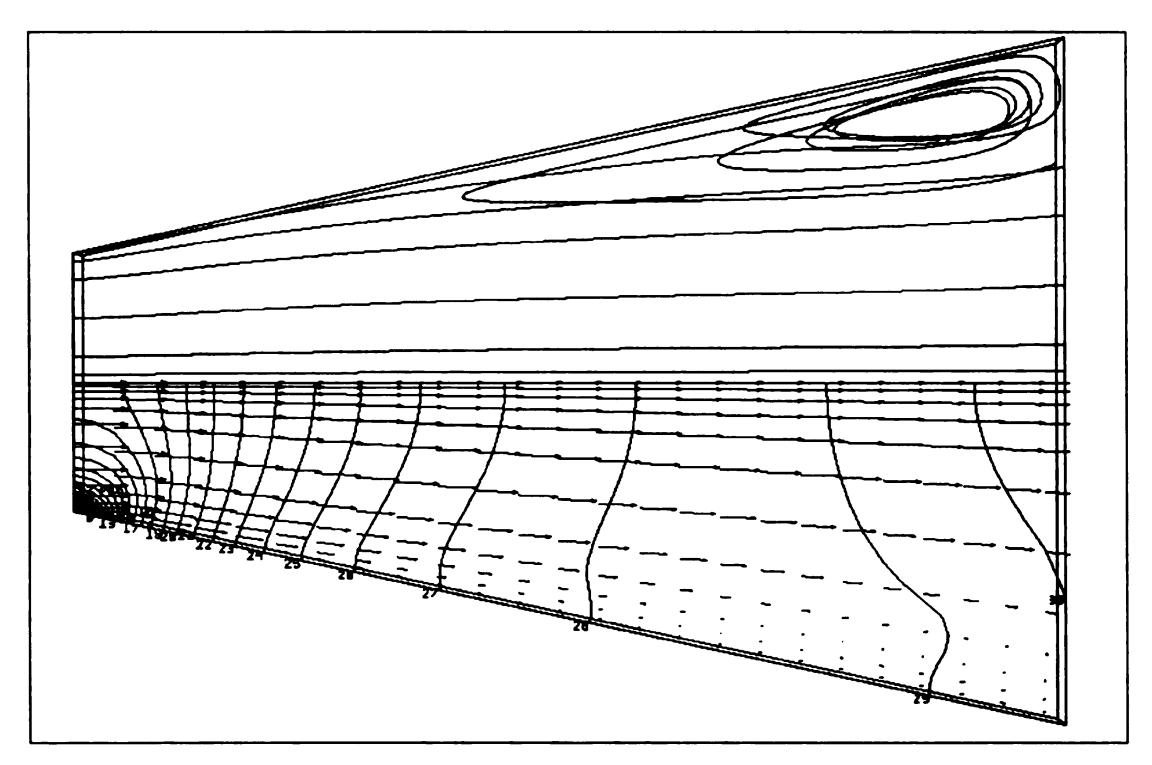


Figure 2.11 An example of the separated flow in a 2-D diffuser

#### 2.2.1. Stall in a Compressor Component

In a diffusing flow, resulting from area change or flow curvature as in an airfoil, there is a possibility that the flow at the wall is retarded so severely that it can no longer follow the wall surface. The necessary energy to overcome this gradient is transmitted from the main inviscid stream to the boundary layer by viscous or turbulent stresses. When the momentum in the boundary layer is insufficient to overcome this pressure gradient, the flow will separate and local return flow will occur. From a macroscopic point of view, this reorientation of the flow can have a steady characteristic (steady stall) or can be an unsteady phenomenon in which separated and attached flow are alternating (rotating stall). This last phenomenon is due to the fact that local flow separation influences the surrounding flow field in such a way that other zones of separated flow are

created which in turn are influencing the initial separated zone. Stall can occur in the inducer (due to incidence), impeller (jet and wake flow), vaneless diffuser (negative radial velocity), vaned diffuser channels, and return channels.

The effect of secondary flow can cause flow separation leading to flow instability.

The instabilities in the compressor can be classified as the component stall, stage stall, and system instability described as surge.

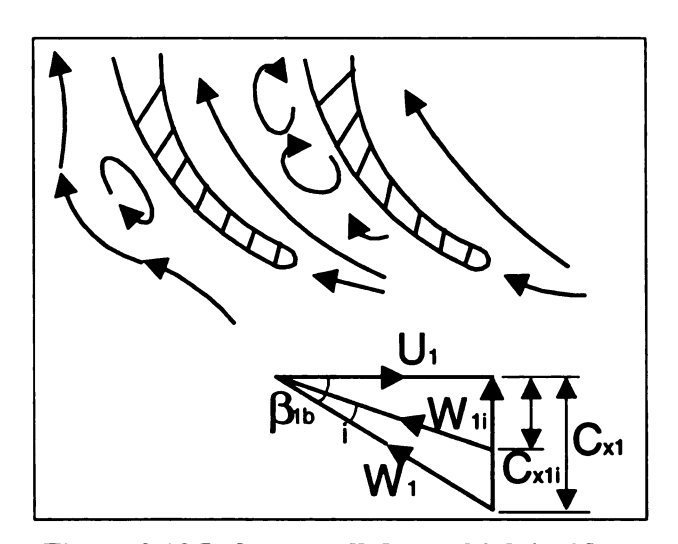


Figure 2.12 Inducer stall due to high incidence

#### 2.2.1.1. Inducer Stall

Stall in the impeller can be due to unsteady phenomena in the inducer or in the radial part of the impeller. When the inducer stalls, high energy fluid emerges from the impeller to the inlet region. The reversed flow discharged from the impeller during inducer stall has a significant impact on the velocity distribution at the inlet.

Mizuki et al. (1976) observed flow at a low flow rate in the inlet duct, the inducer, the impeller channels, and along the shroud casing. This backflow was attributed to a separated flow at the inducer inlet leading edge. Furthermore, they observed a three

dimensional eddy in the inducer channel that became stronger toward the suction side as well as at the shroud casing.

Senoo et al. (1979) investigated a supersonic centrifugal impeller. He was able to associate all necessary phenomena to the impeller, because the compressor had no diffuser so that the flow range was not limited by the diffuser. He suggested that the stall point in the inducer be correlated to the incidence at the tip of inducer and to the relationship between the relative velocity in front of the inducer and the relative velocity in the inducer throat.

Kämmer et al. (1982) reported that pressure fluctuations are non-periodic though unsteady in nature in case of inducer stall.

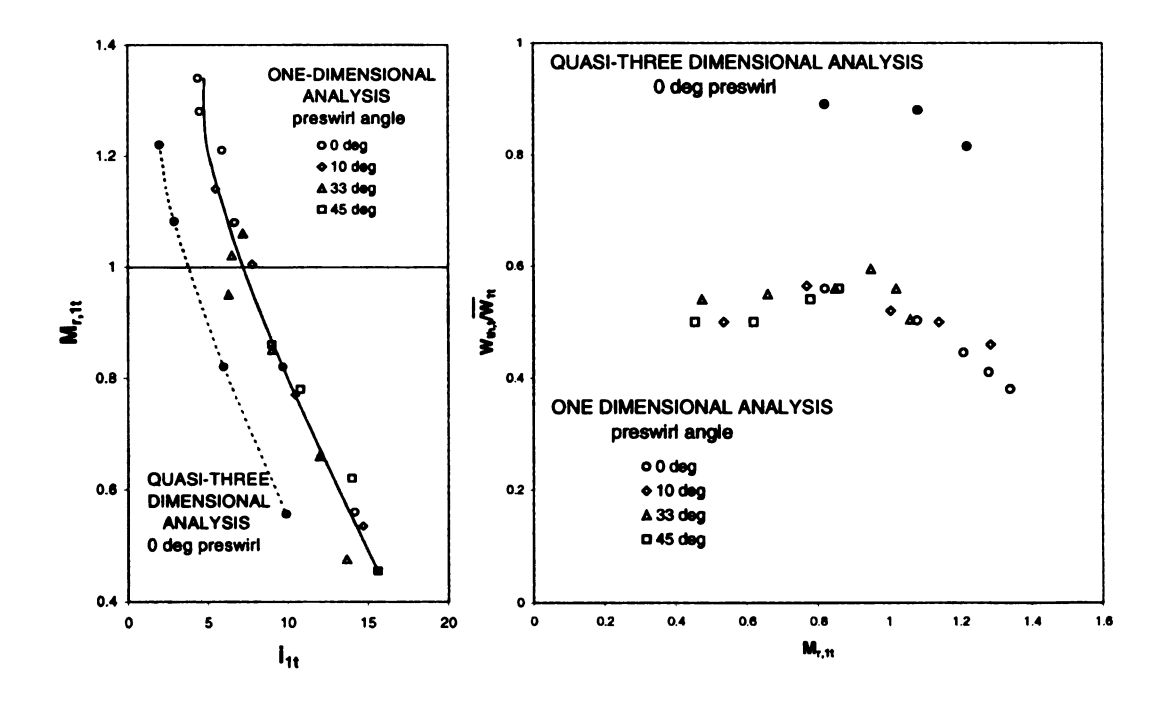


Figure 2.13 Critical conditions of inducer stall (Senoo et al., 1979)

Kämmer et al. (1985) measured the subsequent backflow in terms of temperature, pressure, and flow angle. When the inducer stalls, high energy flow moves back from the

impeller. This backflow has a large tangential flow component. The centrifugal force due to this tangential flow component supports the separation of backflow and the main flow. This causes an increase in temperature and pressure in the inducer. As stall is initiated, the reversed flow at the tip blocks the inlet annulus; and the main flow is accelerated. In addition, a tangential velocity is generated, and it produces prewhirl at the inlet. As mass flow continues to be reduced, the axial velocity distribution becomes more distorted; and the prewhirl affects the main flow.

# 2.2.1.2. Impeller Stall

During impeller rotating stall, pressure fluctuations occur throughout the entire meridional extent of the blade channels.

Visual evidence of rotating stall in a centrifugal impeller passage was given by Lennemann et al. (1970). They visualized the phenomena of rotating stall in the impeller using hydrogen bubble technique.

Figure 2.14 shows the sequence of the unsteady motion triggered by pressure side separation in an unshrouded impeller, which is significantly different from that of the shrouded impeller. The boundary layer separates on the blade pressure side, and the subsequent backflow is supported strongly by the relative eddy effect. The fluid is first driven back along the blade pressure side and further upstream along the blade suction side toward the passage entry. Here fluid moves out of the passage into the inducer. If, due to the rotation, the passage flow conditions become more favorable, the passage flow can recover and the motion is repeated. However, in the case of stall the flow is

separating at the pressure side, while the flow at a stable operation point separates at the suction side due to the jet/wake pattern.

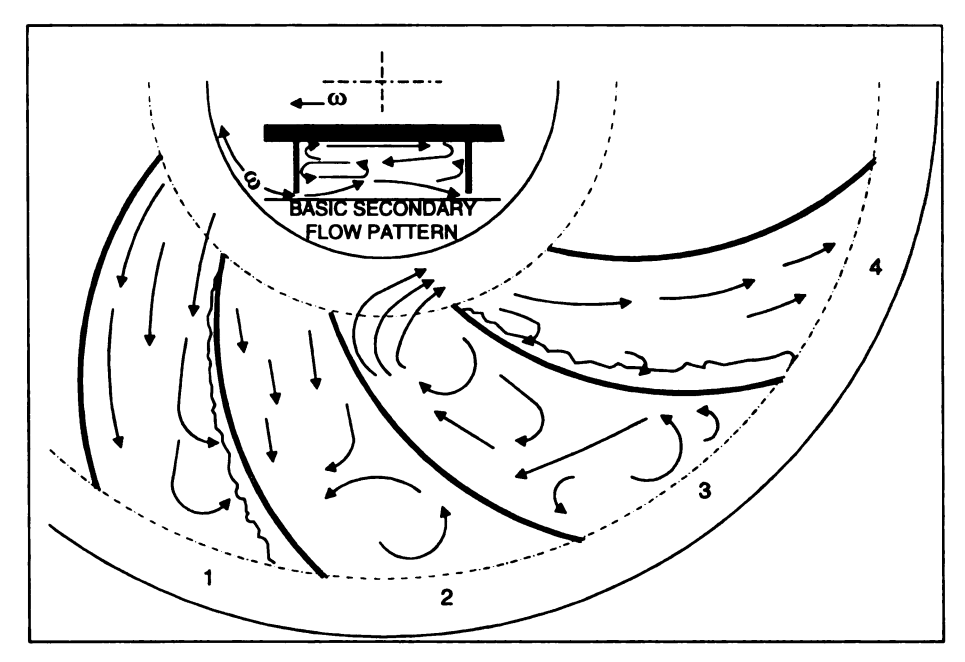


Figure 2.14 Sequence of passage stall in a single passage, unshrouded impeller (Lennemann et al., 1970)

Rodgers (1977) considered the relationship between the relative velocity at the impeller exit and the relative velocity at the impeller inlet as a criterion for impeller stall. He investigated stall criteria using twelve different backswept impellers and suggested a modified diffusion factor taking the effect of meridoinal curvature into consideration. The revised diffusion factor for an impeller with no prewhirl is defined as follows:

$$D_{f} = 1 - \frac{\overline{w_{2}}}{w_{1m}} + \frac{\pi \cdot r_{2} \cdot \mu \cdot u_{2}}{z \cdot s \cdot w_{1m}} + 0.1 \cdot \frac{b}{r_{s}} \left( 1 + \frac{\overline{w_{2}}}{w_{1m}} \right)$$
 (2-6)

This factor is based on the diffusion factor for the axial compressor and extended for centrifugal impellers. The third term takes the load for one single blade in consideration and the fourth term accounts for the influence of curvature of the mean streamline curvature.

Senoo et al. (1979) reported that the stall point of the impeller is determined by the ratio between the relative velocity at the impeller exit to the relative velocity at the impeller inlet, as Rodgers did. Such a correlation is only possible, if no backflow occurs in the inducer.

Kämmer et al. (1982) observed that the rotating stall in their configuration did not always appear in a quasi-steady state. At high speeds, the compressor periodically ran into rotating stall and recovered afterwards.

Fringe et al. (1983) found that three operating modes that they called mild, abrupt, and progressive stall. The propagation velocity of the patterns increased with reduction of the flow rate for mild and abrupt stall. In their tests, the propagation velocity relative to the impeller rotation speed was 25 - 35 %. Progressive impeller rotating stall due to flow separation in the impeller shows typical propagation speed (50~80%) and moderate velocity oscillation of 10%, where the stall cell number seems to remain constant.

#### 2.2.1.3. Vaneless Diffuser Stall

Flow becomes more and more distorted axially in a vaneless diffuser with a small flow rate and the distorted flow patterns rotate in the direction of the impeller rotation. It is not like as the rotating stall in an impeller or a vaned diffuser.

One of the first studies on self-excited rotating pressure fluctuation was done by Jansen (1964). He concluded that diffuser rotating stall will occur when there is local return flow in the diffuser.

From momentum and continuity equations, he derived the linear form of governing equation:

$$\frac{1}{\omega}\frac{\partial}{\partial t}\nabla^2\phi + \frac{\cot\alpha}{r}\frac{\partial}{\partial r}\nabla^2\phi + \frac{1}{r^2}\frac{\partial}{\partial \theta}\nabla^2\phi = 0$$
 (2-7)

where  $\phi$  is a streamfunction and its simplest solution can be expressed as

$$\phi = \psi(r)e^{i(\omega_n t + m\alpha)} \tag{2-8}$$

where  $\psi(r)$  is the local amplitude. He showed in his calculation that even a potential flow in a radial diffuser can become unstable and that the unsteady response of the vaneless diffuser flow is triggered by viscous flow effects but is governed by the inviscid flow. He suggested that the separation of the three-dimensional wall boundary layer trigger rotating stall. This instability causes rotating pressure perturbations.

Senoo (1978,1979) calculated the flows in various vaneless diffusers including boundary layer effects and more complex and likely boundary conditions. He related the reverse flow to the inlet flow angle and diffuser width.

Van den Braembussche et al. (1980) showed that Senoo's prediction of critical diffuser inlet flow angle agrees well with experimental data if a Reynolds number correction is applied as shown in Figure 2.15.

Fringe et al. (1983) performed experimental investigation of the sub synchronous rotating flow patterns in a centrifugal compressor with vaneless diffuser. He found diffuser rotating stall due to a strong interaction between boundary layer and inviscid core flow in the vaneless diffuser. Typical for this rotating stall is the low relative propagation speed ( $\omega_s/\Omega$ <=0.2) and the moderate amplitude of the velocity fluctuations around 10%.

Abdelhamid (1980) proposed stability criterion based on linearized equation for two-dimensional incompressible and frictionless flow assuming that the perturbations are harmonic functions.

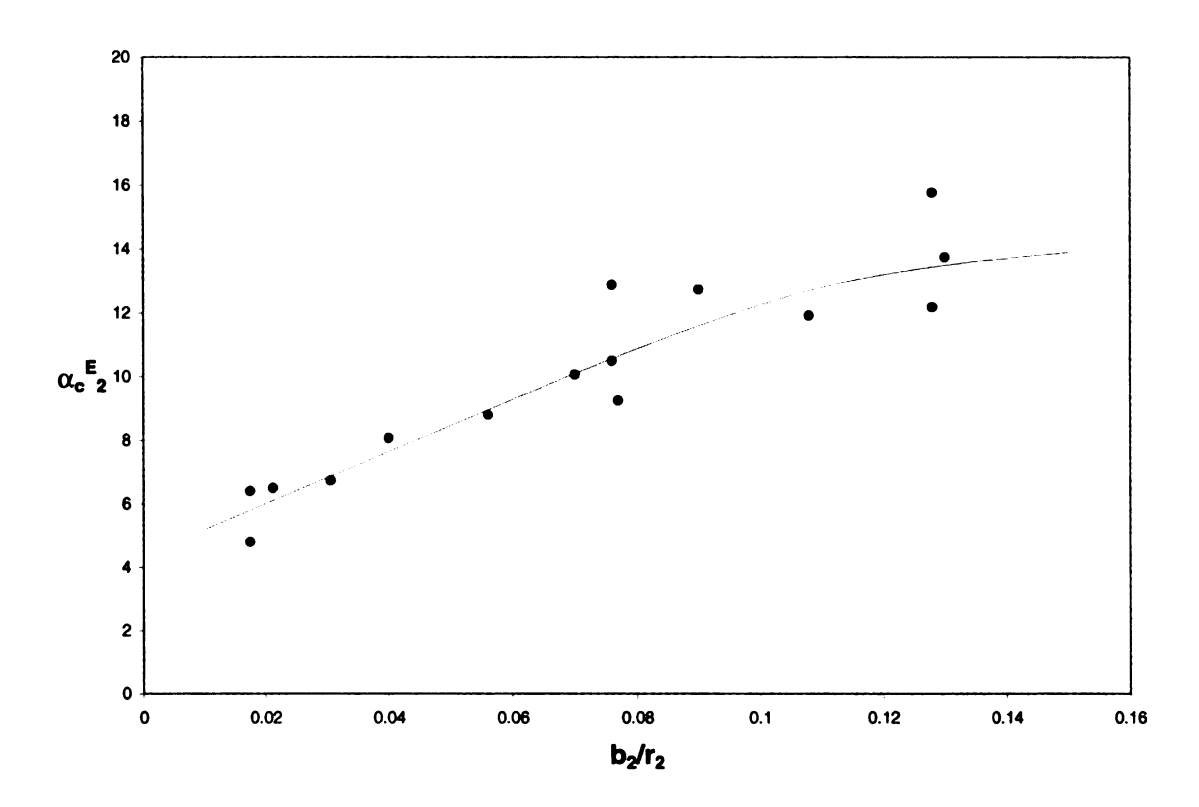


Figure 2.15 Critical inlet flow angle with diffuser width (Van den Braembussche et al., 1980)

# 2.2.1.4. Vaned Diffuser Stall

Stall in a vaned diffuser may be initiated in the semi-vaneless space at the diffuser inlet. The static pressure recovery in this region and incidence angle at the vane leading edge both increase as mass flow is reduced. The combinations of these effects contribute to the initiation of stall. Stalls with 1 to 7 stall cells have been observed in centrifugal compressors with vaned diffusers. Generally, the propagation velocity is much lower for these modes of rotating stall than for those encountered in compressors with vaneless diffusers. Furthermore, lobe number generally decreases as operational speed increases according to Haupt et al. (1988) and Seidel et al. (1991).

Haupt et al. (1988) found a higher number of instances of rotating stall occurring at relatively higher flow rates when their compressor was fitted with a straight channel diffuser than with a cambered vane diffuser. On the other hand, flow oscillation amplitudes for the cambered vaned diffuser exceeded those of the straight channel.

#### 2.2.2. Surge

On the contrary to the rotating stall, where annulus averaged mass flowrate remains roughly constant, surge produces a fluctuation in the system flowrate leading to violent changes of inlet and exit conditions. Surge is a system phenomenon, whereas stall is considered as a local phenomenon. The onset of surge occurs when the operating point lies near the maximum pressure ratio associated with the operating speed. Whereas most axial compressors manifest rotating stall behavior before surge occurs, the centrifugal compressors start surging with or without preliminary rotating stall. Surge causes the compressor system to vibrate and can result in mechanical failure especially to high pressure ratio compressors.

Generally, surge intensity increases with increase in stage pressure ratio and the frequency of flow fluctuation associated with surge is very low in the order of less than 10Hz.

# 2.3. Research Status on Low Solidity Vaned Diffuser

The first reference to a LSVD was in a Japanese patent by Senoo (1978) who characterized the vanes by a solidity of less than 0.9 and introduced both single and tandem row LSVDs. It also suggests that the centrifugal stage had better performance

with LSVD than with the vaneless diffuser without any loss of flow range. Since then Senoo has presented a series of papers that give the details of LSVD performance.

Senoo et al. (1981,1983) presented and discussed the results for both single and tandem row LSVDs installed in a centrifugal blower. They used USA 35B airfoil shape for the vanes conformally mapped into a circular cascade. The single row LSVD tested had 11 blades with 0.69 solidity. The tests with this LSVD were performed with two different stagger angles of 70° and 68°. In addition, another single row LSVD with 13 vanes and 0.82 solidity was also tested. In the case of the two-row tandem cascade LSVD, the first row had a solidity of 0.345 with 11 blades, and the second row had a solidity of 0.63. The tests were performed for various combinations of vane setting or stagger angles and radius ratios between the two rows to arrive at the peak recovery in the diffuser (Figure 2.16).

The results of LSVD tests showed dramatic improvements in pressure recovery with respect to a vaneless diffuser, especially near surge flow. Most importantly, they found almost no reduction in flow range with LSVDs. Near surge, the tandem cascade configurations offered a much smaller additional increase in Cp, but the improvement at high flows was nearly double that of the single row LSVDs. Further they observed that the variation in stagger angle and solidity had a small effect on the performance with relatively minor changes in surge location. The oil film patterns of the single row cascade showed strong secondary flows along the sidewalls indicating the vane suction surface boundary layers were sucked and moved toward the pressure surface of the adjacent vane. This delays the boundary layer separation on the suction surface. From the oil film patterns of two row tandem cascade it was found that the accumulated boundary layer on

the first row pressure surface is redirected to the main flow via the slit, allowing new boundary layers to form on the rear row. Thus, 3-D boundary layer effects along the sidewalls delay stall onset leading to a higher pressure rise.

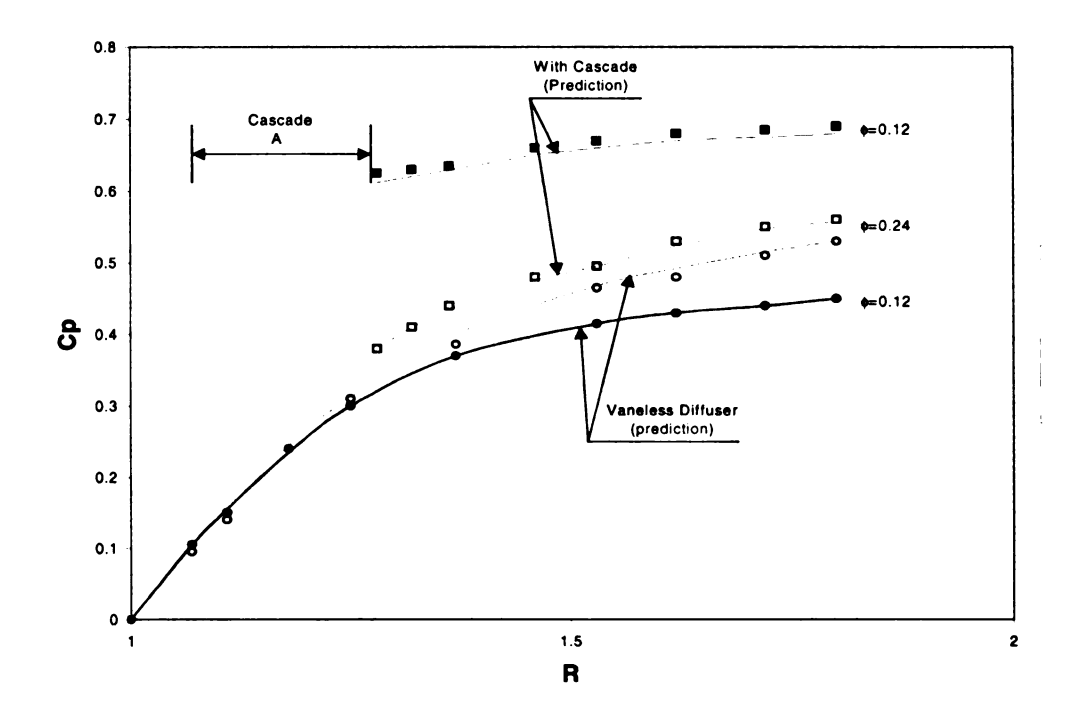


Figure 2.16 Comparison of pressure distributions (Senoo et al., 1983)

Senoo (1984) summarized the effect of solidity, vane number, and stagger angle on the performance of the LSVD and emphasized the need to positively use secondary flow to obtain enhanced diffuser performance. In addition to the data presented in his 1983 paper, new data for a 22 vane LSVD with the same solidity and stagger angle as for the 11 vane configuration as well as a 11 vane design with 0.82 solidity was included.

The peak Cp values were nearly same for 11 and 22 vane configurations, but the peak efficiency point was at about 20% to 25% higher flow for 22 vanes and there was no noticeable change in surge line location with the vane number. However, the Cp drop from peak to surge was more rapid in case of 22 vane LSVD. With the increase in solidity ratio, the peak Cp attained was lowered and moved to higher flow rate. Moreover the

surge occurred at about 20% higher flow rate for LSVD with solidity of 0.82. The surge point moves about 10% lower as the stagger angle increased.

Osborne and Sorokes (1988) used single row LSVDs with single and multistage compressors having radial and mixed flow impellers, along with a wide range of specific speeds and various sizes and gases. From their tests it was concluded that LSVDs were successful with respect to efficiency and flow range even at high and medium specific speeds. They also showed that attractive performance gains resulted with simple flat plate vanes and for geometric parameters (such as vane number and vane setting radius ratios) which were beyond Senoo's study. However the solidity of 0.69 was retained for almost all configurations tested, and the stagger angles were maintained relatively high.

Hayami et al. (1990) showed the LSVD with 0.69 solidity performed better than the vaneless diffuser of a transonic centrifugal compressor. The vanes were conformally transformed from linear cascade of double circular arc vanes. The LSVD also demonstrated good pressure recovery over a wide range of inflow angles, and the pressure recovery improved with increase in the inlet Mach number of up to 1.1. They also found that the LSVD had maximum pressure recovery at an incidence angle of -2° to -3°.

Sorokes and Welch (1991, 1992) developed a rotatable LSVD system, which was used to study the effect of stagger angle. In addition to stagger angle they also studied the effect of vane leading edge radius ratio (by placing the vanes at both 1.08 and 1.15 radius ratio) and the effect of chord length of the vanes by using small and many (S/M) and large and few (L/F) arrangements of the LSVD. All LSVD arrangements tested had 0.735 solidity.

They observed that the best efficiency point, head rise to surge, stability range, and choke margin all exhibit strong sensitivity to stagger angle. The overload capacity displayed a marked decrease as the stagger angle was increased. The factors contributing to this effects were, flow separation from the pressure surface of the vanes, and at high stagger angles the distance between two vanes at the trailing edge decreased tended to form a throat. On the other hand, when the stagger angle was decreased, the LSVD vanes stalled, reducing the surge margin. It was also observed that the decrease in surge margin was significant even for small decrease in stagger angle.

In a comparative study of the vane leading edge radius ratio and the S/M and L/F arrangements, they found that the 1.08 L/F build had the highest pressure recovery. While the 1.15 L/F build exhibited advantage over the 1.08 L/F build in terms of surge margin, both the 1.08 and 1.15 S/M arrangements had better stall margin than their respective L/F counterparts. Thus, the 1.08 L/F build had greater sensitivity to off design incidence, even though its pressure recovery was better than the other builds. They also observed that the length and/or exit angle of the LSVD vanes had influence on the downstream components.

Hohlweg et al. (1993) performed experiments on a process compressor and an air compressor with LSVDs. The LSVD used with the process compressor had 10 vanes with 0.7 solidity, while three LSVDs were tested with an air compressor, all having 16 vanes and 0.7 solidity but different design incidence of -4.1°, -1.9° and +0.3°.

In their results they found that the LSVD with highest negative incidence provided maximum flow range, while the LSVD with +0.3° incidence had small flow range and the stage efficiency was less than the other two LSVDs. However, the LSVD with -1.9°

incidence had better stage peak efficiency than the one with -4.1°. Thus, they concluded that negative design incidence in general was good for LSVD performance and there should be an optimum negative incidence based on the impeller tip Mach number that would provide both good flow range and efficiency.

From the results of low Mach number process compressor testing, they observed that the LSVD had almost the same peak efficiency as the conventional vaned diffuser, but the flow range of LSVD was considerably lower than the conventional vaned diffuser. They speculated from this observation that the low vane number might have allowed large stall cells to develop due to low flow angles at the vane leading edge, even though the design incidence of the LSVD was -3.1°.

Amineni(1996) performed experiments on four different LSVDs having solidity of 0.6 and 0.7 and vane number of 14 and 16 to understand the effects of turning angle and solidity on the performance of the diffusers, and compared these results with numerical analysis. The experiments were performed at three different impeller tip Mach numbers to study the effect of rotational speed on the performance of the diffusers. He showed that the peak efficiency of the compressor increased with an increase in blade turning angle of the low solidity vaned diffuser while the flow range suffered. He also found that the effect of the solidity on the peak efficiency of the compressor stage was very small while lower solidity diffusers were able to provide better flow range. He found that the low solidity vaned diffusers stalled when the vane suction surface separation was accompanied by the end wall separation. He found that nearly 75% of the total pressure recovery in the low solidity vaned diffusers occurred between the impeller exit and the vane trailing edge radius and that the pressure recovery between impeller exit and vane

leading edge was much higher in the case of low solidity vaned diffusers than the conventional vaned or vaneless diffusers.

Thus, there is no clear understanding of the effect of the vane number and solidity of the LSVD, which seem to be two major parameters in the LSVD design. Moreover, the effect of vane number and vane leading edge radius ratio on the impeller discharge flow is not clearly understood in the case of the LSVD, as some of the reports indicate that the LSVDs with small vane leading edge radius ratios performed better, which is not the case in conventional vaned diffusers.

## 2.4. Low Solidity Vaned Diffuser Design

Since there is no clear performance method available for LSVDs, a simple approach for design was chosen concluded from numerical and experimental results with comparable LSVDs carried out by earlier engineers. All four LSVDs were designed with simple flat plate similar to the approach taken by Sorokes et al. (1991,1992) and Hohlweg et al. (1993) because of their reported success and low manufacturing costs. Amineni (1996) investigated LSVDs with 14 vanes and 16 vanes and showed that any increase in vane number manifests into a more stable flow through the diffuser due to blade loading reduction. In this work vane number and solidity was fixed with 18 vanes and 0.9 respectively initially(LSVD5). By trimming the vane trailing edge solidity of 0.8, 0.7, and 0.6 were obtained in turn.

Since the vane inlet angle is regarded to be an important design parameter, the test results of many investigators have been used. The vane inlet angle is determined by first calculating the flow angle at the design point and then adding the required incidence

angle to it. The design flow angle ( $\alpha_2$ ) at the impeller exit was evaluated from a quasi one dimensional flow calculation through the impeller. From the reports of Hohlweg et al. (1993) and Sorokes et al. (1992) it has become very clear that the design incidence angle has a major impact on the flow range and the pressure recovery of the LSVD. Figure 2-5 represents the incidence effect on flow range and it can be seen that in general the flow range tends to increase as the design incidence angle becomes negative up to a certain negative incidence; thus, indicating that there is an optimum incidence angle at which highest flow range can be attained. Figure 2-6 shows the insensibility of the peak efficiency at a design incidence of around -2°. Hohlweg et al. (1993), also obtained highest efficiency for the LSVD with -1.9° design incidence. Thus, for all four LSVDs designed for experimental testing had -2° design incidence.

On the basis of four existing LSVDs a new LSVD with 18 vanes was designed for the highest solidity that still avoids a throat leading to an initial solidity of 0.9. By cutting back the vane tips, solidities of 0.8, 0.7, and 0.6 were also generated. To determine maximum solidity for a vane that has an outer diameter just at the throat, the following simple calculation was carried out.

The geometrical parameters of LSVD are shown in . With given inlet radius  $(r_3)$ , vane inlet angle  $(\beta_3)$ , vane number (Z), and blade thickness  $(t_{bl})$ , pitch (s) is

$$s = 2 \cdot r_3 \cdot \sin\left(\frac{180}{Z}\right) \tag{2-9}$$

Since the blade contour does not form a single line, the blade length has to be corrected

$$l_{adj} = l + \frac{t_{bl}}{2\tan\beta_3} \tag{2-10}$$

The solidity is defined as the ratio of adjusted blade length to pitch

$$\sigma = \frac{l_{adj}}{s} \tag{2-11}$$

With 18 vanes for a given compressor, the maximum solidity came to 0.936.

For convenience, solidity of 0.9 was chosen for a starting solidity and the trailing edges of the diffuser vanes were trimmed to vary the solidity with -0.1 solidity step.

Once the solidity were determined, vane exit angle  $(\beta_4)$  and vane trailing edge radius  $(r_4)$  would be:

$$\tan \beta_4 = \tan \beta_3 + \frac{2\sigma \sin\left(\frac{180}{Z}\right)}{\cos \beta_3} - \frac{t_{bl}}{2r_3 \sin \beta_3}$$
 (2-12)

$$r_4 = r_3 \frac{\cos \beta_3}{\cos \beta_4} \tag{2-13}$$

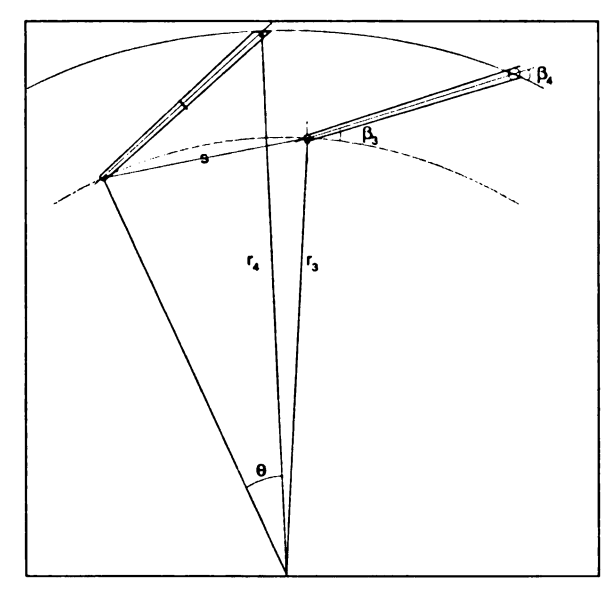


Figure 2.17 Maximum solidity

# 3. EXPERIMENTAL SETUP

# 3.1. Test Compressor

The present investigations of performance of different diffusion systems for a centrifugal compressor were carried out on the first stage of a plant air package compressor. The schematic outline of the test rig is shown in Figure 3.1. The centrifugal compressor was driven by a variable speed motor with a maximum power output of 225 kW. The impeller and the motor were coupled through a gearbox of 9.054 gear ratio. The speed of the motor was accurately controlled by a frequency controller capable of

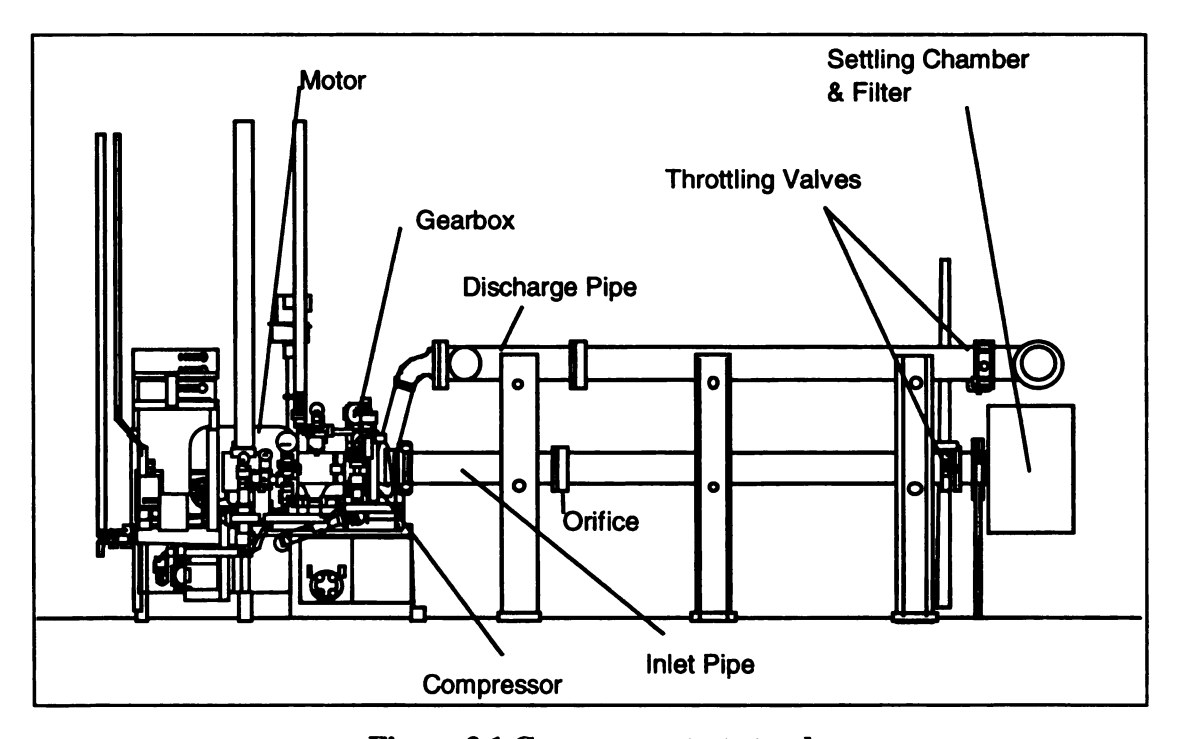


Figure 3.1 Compressor test stand

adjusting the power supplied to the motor in accordance with the load on compressor.

The impeller is unshrouded and has 19 blades with backward leaning angle  $\beta_{2b}$ =70.7°, as shown in Figure 3.2. The blade camberline has ellipsoidal shape in cylindrical section. The inlet hub and shroud diameters are 47.09 mm and 147.67 mm respectively. The impeller tip diameter is 244 mm, with exit blade width of 13.33 mm.

The compressor was tested in an open air loop. The air entered the compressor through an air filter, a settling chamber, and an inlet pipe. The settling chamber provides the compressor with an air supply free of the temperature stratification, thus enabling the compressor inlet temperature to be measured accurately. After being compressed in the impeller, the air is discharged to the outlet pipe after passing through the diffuser and the



Figure 3.2 Centrifugal compressor impeller

volute of the compressor. The air in the outlet pipe is muffled with the aid of silencer before it is discharged. The mass flow rate through the compressor could be controlled by either of the throttle valves located in the inlet or the outlet pipes. However, for the results presented here the mass flow rate was controlled by the throttle valve located in the outlet pipe.

# 3.2. Investigated Low Solidity Vaned Diffusers

Four low solidity vaned diffusers (LSVD5 through LSVD8) were tested downstream of the same impeller. The vanes of all the low solidity vaned diffusers were machined on to an aluminum plate. Figure 3.3 shows the notation of a low solidity vaned diffuser. The low solidity vaned diffusers have constant width from inlet to exit, and the width of the diffusers was equal to that of the conventional vaned diffuser. Similarly, the radius ratio of the vaneless space between the impeller exit and the leading edge of the vanes was the same in all the low solidity vaned diffusers and the conventional vaned diffuser. All diffusers were tested at three different speeds corresponding to the impeller tip Mach number (Mu) of 0.69, 0.88 and 1.02. Amineni (1996) designed and performed tests on the vaneless diffusers, conventional vaned diffuser and LSVD1 through LSVD4 with the same configuration. The principle specifications of the diffusers are given in Table 3-1.

**Table 3-1 Diffuser Geometric Parameters** 

	$b_{2s}/b_2$	$r_3/r_2$	r <sub>4</sub> /r <sub>2</sub>	r <sub>5</sub> /r <sub>2</sub>	Z	θ		σ	Designed by
VNL1	0.70	-	•	1.53	•	•	-	•	Elliott Co.
VNL2	0.83	-	-	1.53	•	•	-	-	Elliott Co.
CVND	1.0	1.09	-	1.53	15	•	0	1.15	Elliott Co.

LSVD1	1.0	1.09	1.23	1.53	14	14.6	-2	0.7	Amineni
LSVD2	1.0	1.09	1. 21	1.53	16	12.9	-2	0.6	Amineni
LSVD3	1.0	1.09	1.20	1.53	14	12.6	-2	0.7	Amineni
LSVD4	1.0	1.09	1.19	1.53	16	11.1	-2	0.6	Amineni
LSVD5	1.0	1.09	1.23	1.53	18	14.6	-2	0.9	Kim
LSVD6	1.0	1.09	1.21	1.53	18	13.1	-2	0.8	Kim
LSVD7	1.0	1.09	1.19	1.53	18	11.5	-2	0.7	Kim
LSVD8	1.0	1.09	1.17	1.53	18	9.9	-2	0.6	Kim

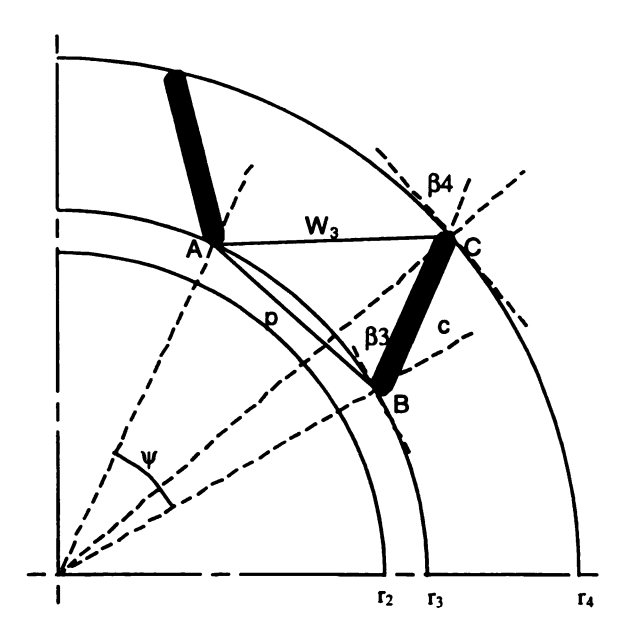


Figure 3.3 LSVD geometry notation

# 3.3. Measurement

The contents of this report present both steady and unsteady results of the experiments performed with the centrifugal compressor test stand having different diffuser configurations described in previous sections. Several static and total temperatures along with static and total pressures and pressure fluctuations at different planes of the compressor stage were measured in order to determine the mass flow rate through the stage, overall performance, and the performance and interaction of various

components of the compressor stage. This section presents the details of all the measurement locations and the measured quantities at these locations.

The mass flow rate was measured with an ASME standard orifice plate. Two total and two static temperatures were measured at different circumferential positions located opposite to each other at the same plane of the inlet pipe, upstream of the orifice. The differential pressure across the orifice plate was measured by two sets of static taps located 76.2 mm downstream and 152.4 mm upstream of the plate. The static pressure at the orifice was also measured at two locations in the same plane, 152.4 mm upstream of the plate.

The stage inlet static and total pressures were measured at two 90° apart circumferential positions each. Similarly, the inlet static and total temperatures are also measured at two different circumferential positions. The pressures are measured at a plane mid way between the orifice plate and the inducer, while the temperatures are measured at a plane located at 330.2 mm from the inducer. Figure 3.4 shows all the measurement planes in the inlet pipe.

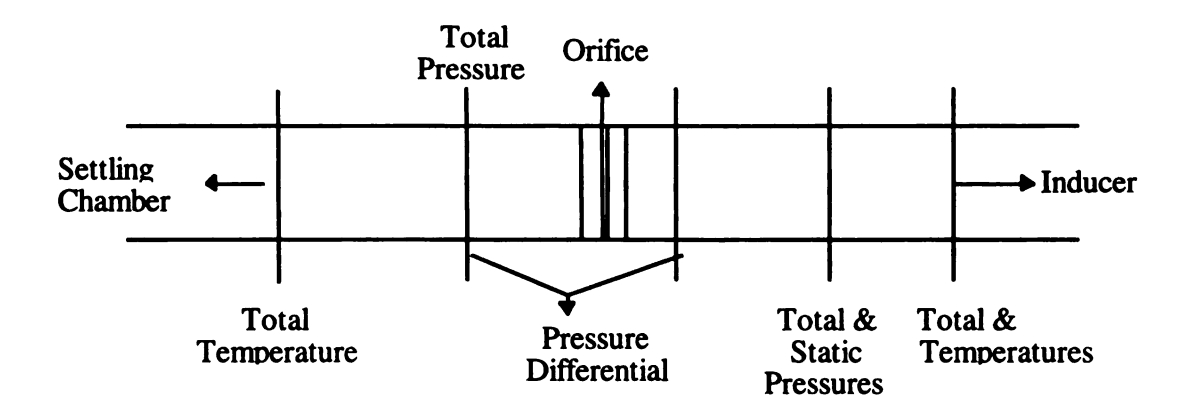


Figure 3.4 Measurement planes in inlet pipe

The inducer behavior is studied by measuring the static temperature just upstream of the inducer and the static pressures at two different axial positions in the inducer. Moreover the pressure fluctuations at the inlet of the inducer are also measured. Figure 3.5 shows the location of the different measurement probes in the compressor stage. The pressure fluctuations and the static pressure in the impeller are measured at a  $r_{imp}/r_2$  ratio of 0.77. All measurements in the impeller are done at the same circumferential plane, and both the dynamic transducers measuring pressure fluctuations and the static pressure taps were located at an angle of 42.5° with respect to each other. All the static taps and the dynamic transducers in the inducer and the impeller were located on the casing of the compressor.

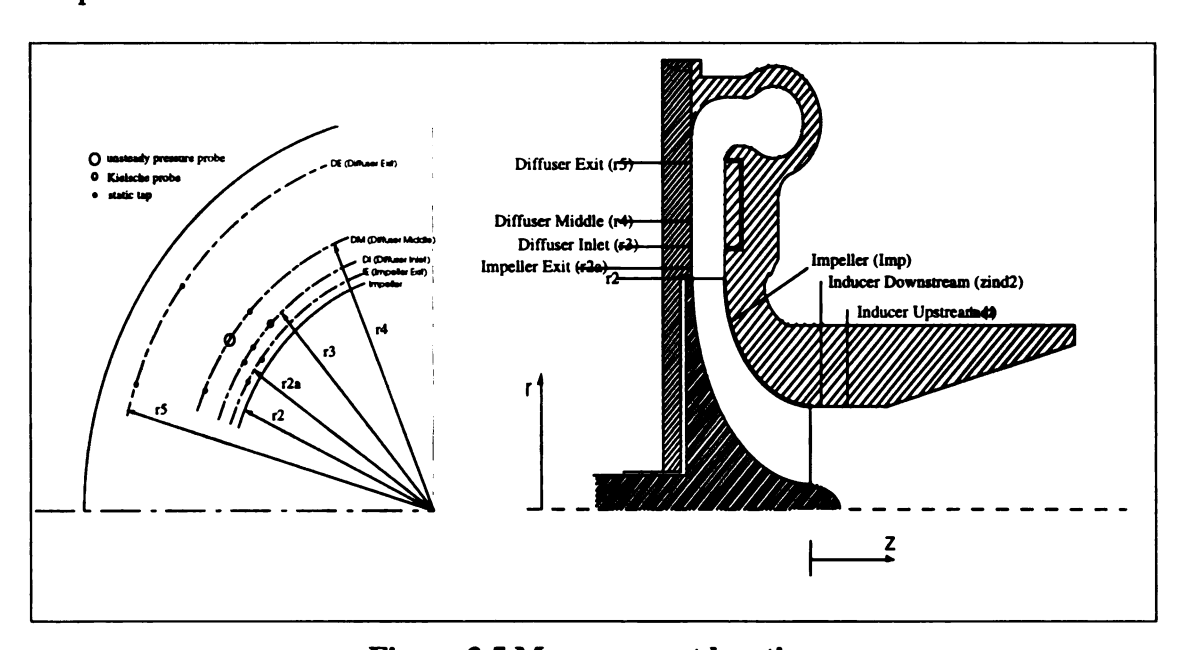


Figure 3.5 Measurement locations

The pressures at the exit of the impeller and at various locations in the diffuser were measured through the taps drilled on the back plate of the compressor. All these taps were located 150° away from the volute tongue in order to minimize any flow asymmetry caused by the presence of volute. Figure 3.5 shows the location of the taps and different

probes on the back plate of the compressor. In all, eight static taps were used to measure the pressure recovery from the impeller exit to the diffuser exit. A set of static taps was located at a radius ratio  $(r_{2a}/r_2)$  of 1.04 to measure the static pressure at the impeller exit. One pair was located at the leading edge radius  $(r_3)$  of all vaned diffusers, a pair was located at the trailing edge radius  $(r_4)$  of the LSVDs or the mid channel of the CVND, and the last pair was located at the diffuser exit radius  $(r_5)$ . In addition to these static pressures the total pressure at the impeller exit was measured at the vane leading edge radius and the pressure fluctuations in the diffuser were measured at the LSVD1 trailing edge radius.

The leading edge radius was chosen for total pressure probe location, since it is assumed that the jet and wake pattern flow coming out of the impeller is mixed out and the flow pattern becomes quasi uniform at this radius. The static taps, the total pressure probe, and the dynamic pressure transducer were placed between the two vanes of the CVND in an attempt to minimize the flow distortion effects caused by the presence of the vanes.

The stage exit pressures and temperatures are measured in the pipe connected to the volute. The exit total and static pressures are measured at four circumferential locations 90° apart in the pipe at the same plane. Similarly the exit total and static temperatures are also measured at four locations at a plane, which is 76.2 mm downstream of the plane where pressures are measured. In order to avoid the heat transfer effects on the temperature measurements the casing of the compressor was covered with insulating material. Table 3-2 summarizes all measurement locations and the quantities measured.

**Table 3-2. Summary of Measurements and Measurement Locations** 

<del></del>					
Location	Position	Static	Notation	Other probes	Unsteady
		pressure			pressure
		taps			transducers
Orifice	as per ASME	2	Porf		
	standards		1 4		
Inlet Pipe	7,	2	Pı	2 total pressure	
•	$\frac{z_1}{}=5$		• •	2 total temperature	
	$r_{1s}$			2 total temperature	
Inducer	Zindl 0.74	1	P <sub>ind1</sub>		
Upstream	$\frac{z_{ind1}}{z} = 0.74$		•		
	$r_{ls}$				
Inducer	$\frac{z_{ind2}}{}=0.40$	1	P <sub>ind2</sub>	1 temperature	Transducer A
Downstream					
	$r_{ls}$				
Impeller	$\frac{r_{imp}}{}=0.77$	2	$\mathbf{p}_{imp}$		Transducer
	$\frac{-1}{2} = 0.77$				B&C
	<b>r</b> 2				$\Delta \phi = 42.5^{\circ}$
Impeller Exit	r.	2	$p_2$		
	$\frac{r_{2a}}{1} = 1.04$	_	P2		
	<i>r</i> <sub>2</sub>				
Diffuser Inlet	<i>r</i> <sub>2</sub>	2	<b>p</b> <sub>3</sub>	1 Kiel probe	
	$\frac{r_3}{r_3} = 1.1$		• •	•	
	<i>r</i> <sub>2</sub>				
Diffuser	$\frac{r_4}{2} = 1.21$	2	P4		Transducer D
Middle					
	<b>r</b> <sub>2</sub>				
Diffuser Exit	$\frac{r_5}{1} = 1.53$	2	P5	1 total pressure	
	$r_2 = 1.33$	}		1 total temperature	
D: 1	. 2		<del> </del>	01	
Discharge pipe		2	P6	2 total pressure	
				2 total temperature	

# 3.4. Steady Performance Data Acquisition

# 3.4.1. Instrumentation

The steady static and total pressures were measured with three different types of pressure measuring devices:

· Validyne - variable reluctance pressure transducers

- · Omega hand held manometers/high stability pressure transducer using molecular bonded strain gage
  - · Water / mercury manometers

The water and mercury manometers have a resolution of 2.54 mm. One of the water manometers is used to measure the differential pressure across the orifice plate and the other is used to measure the stage inlet static pressure. The only mercury manometer is used to measure the stage exit static pressure. The application of the water and mercury manometers at these locations is considered necessary to validate the proper functioning of the Validyne and Omega pressure transducers.

The static pressures were measured with 3.175 mm taps and the total pressures were measured with Kiel probes. Flexible tubing was routed from the static pressure taps and the Kiel probes to the Validyne and Omega transducers. The Validyne transducers are connected to the Validyne digital transducer indicators with Belden type 8434 cable, while the Omega transducers have digital display integrated to the transducer. The Validyne transducers were calibrated with an Omega pressure calibrator in conjunction with the water and mercury manometers, which provide an additional check during the calibration. On the other hand, the Omega pressure transducers were factory calibrated and they were checked for proper function with the water and mercury manometers before use. All pressures were read to the second decimal digit, either in inches of water or mercury. The Validyne pressure transducers are able to measure with an accuracy of ±0.25% of full scale, which includes the effects of linearity, hysteresis and repeatability at an operating temperature range of -17°C to 72°C. Detailed specifications of the instruments are shown in APPENDIX B.

Total temperature probes that were half shielded with bleed slots measured the total temperatures. All temperature measurements were done by copper-constantan (T-type) thermocouples connected to the Omega digital temperature indicators (DP460). The digital displays were calibrated by switching the display to a built-in calibration setting and applying 0.00 mV at the thermocouple input to adjust zero reading and similarly applying 39.00 mV for full scale display reading of 560.0. Once calibrated, the digital displays were capable of indicating temperatures in either °C or °F. For the present study °C display was chosen with 0.1 °C resolution. The accuracy of the Omega digital temperature indicators was ±0.5 °C at 0.1°C resolution setting under the operating temperatures of 5 to 45°C for T-type thermocouples.

#### 3.4.2. Data Collection and Reduction

The compressor was tested at three different impeller tip Mach numbers ( $M_u$  = 0.69, 0.88, 1.02) for each diffuser configuration. At each speed the temperature and pressure measurements were collected from all probe locations for approximately 9 to 13 different mass flow rates, ranging from compressor choke to surge in order to obtain a complete speed line. The mass flow rate through the compressor was controlled with the throttle valve located at the stage exit.

At each flow point, the data were collected when the compressor stage reached steady state condition in terms of the temperature. The stability criterion was the temperatures at the stage inlet and exit oscillated within  $\pm 0.1^{\circ}$ C. Once the stage was considered stable, all the pressures and temperatures were recorded and transferred on to a PowerPC for further data reduction and processing.

The data reduction and processing were done by an EXCEL program. The program first converts the recorded pressures and temperatures into N/m<sup>2</sup> and K. At this stage the temperatures and pressures at each measurement plane are compared with each other and with downstream and upstream measurement planes. In this way any faulty or malfunctioning transducers are detected, and the data from them are eliminated before obtaining average pressures and temperatures at each measurement plane. The program uses the averaged pressures and temperatures at various planes to calculate the stage overall performance and the component performance parameters. The program is also capable of plotting these performance parameters with the mass flow rate or the impeller exit flow angles. This on-line plotting capability of the program acts as a good tool to monitor the behavior of the stage and the whole system; moreover, it also provides greater flexibility in control and operation.

The overall performance parameters calculated were the stage static and total pressure ratios, the total temperature ratio, the total-to-total isentropic efficiency of the stage, the head coefficient, the work coefficient, and the stage pressure recovery. In addition to the above mentioned overall performance parameters, individual component performance was determined by calculating the impeller pressure ratio, the impeller total-to-total efficiency, the pressure recovery of the impeller, the diffuser, and the volute.

In order to understand the pressure recovery phenomenon in all three types of diffusers, the diffusers were subdivided into three regions; and the pressure recovery in each of these regions was calculated. The subdivision was based on the low solidity vaned diffusers: (1) the vaneless space from impeller exit to the vane leading edge, (2) the

vaned region, from vane leading edge to trailing edge, and (3) the downstream vaneless space from vane trailing edge to the diffuser exit.

The stage and impeller total pressure ratio compares the total pressures at the stage exit and rotor exit, with the stage inlet total pressure. As such, they are

$$\pi_{0,rotor} = \frac{P_{03}}{P_{01}} \tag{3-1}$$

and

$$\pi_{0,stage} = \frac{P_{06}}{P_{01}} \tag{3-2}$$

Similarly, the rotor and stage static pressure ratios are given as

$$\pi_{rotor} = \frac{P_2}{P_1} \tag{3-3}$$

$$\pi_{stage} = \frac{P_6}{P_1} \tag{3-4}$$

The isentropic efficiency can likewise be calculated for both the rotor and the stage. Efficiency is the ratio of work done in an ideal process to the actual work. For compression process between two states 1 and 2, this can be expressed as a ratio of the isentropic work (representing the ideal process) and the real work. In terms of enthalpy this becomes (Figure 1-2)

$$\eta_s = \frac{w_s}{w} = \frac{h_{02s} - h_{01}}{h_{02} - h_{01}} \tag{3-5}$$

For an ideal gas with constant  $c_p$ , the relation  $dh = c_p dT$  can be used to rewrite equation (3-5) in terms of temperatures

$$\eta_s = \frac{w_s}{w} = \frac{T_{02s} - T_{01}}{T_{02} - T_{01}} \tag{3-6}$$

In an isentropic process with constant properties, the pressures and temperatures are related according to

$$\frac{P_{02}}{P_{01}} = \left(\frac{T_{02s}}{T_{01}}\right)^{\left(\frac{\gamma}{\gamma-1}\right)} \tag{3-7}$$

Thus, substituting into equation (3-6), the isentropic efficiency for a compression process between state 1 and 2 can be written as

$$\eta_s = \frac{\left(\frac{P_{02}}{P_{01}}\right)^{(r-1/r)} - 1}{\frac{T_{02}}{T_{01}} - 1}$$
(3-8)

It is also known as total-to-total isentropic efficiency as the total conditions at the state 1 and 2 are used to for calculation.

In the present investigation equation (3-8) was used to find the isentropic total to total efficiency of the rotor and the stage. However, the heat transfer through the casing is considered to be negligible and the stage exit total temperature is used for calculating the rotor efficiency too, i.e.  $T_{06} = T_{03}$ . The ratio of stage exit to inlet total temperature is also given as

$$\tau_0 = \frac{T_{06}}{T_{01}} = \frac{T_{03}}{T_{01}} \tag{3-9}$$

Thus, the appropriate expressions for rotor and stage efficiency are

$$\eta_{t-t,rotor} = \frac{\left(\pi_{0,rotor}\right)^{(r-1/r)} - 1}{\tau_0 - 1}$$
 (3-10)

and

$$\eta_{t-t,stage} = \frac{\left(\pi_{0,stage}\right)^{\left(\gamma-\frac{1}{\gamma_{t}}\right)} - 1}{\tau_{0} - 1} \tag{3-11}$$

The energy transferred by the rotating blades to the gas passing through the impeller per unit mass is defined as the compressor "head". Although the compressor produces head, it cannot be measured directly. However, it can be calculated from the measured pressure ratio, inlet and exit temperatures and gas properties. Head in nondimensional form is given as

$$\psi = \frac{\Delta h_{0s}}{\frac{1}{2}U_2^2} \tag{3-12}$$

and is known as isentropic head coefficient. Using equation (3-7) the head coefficient can be written in terms of measured quantities and gas properties as

$$\psi = \frac{c_p T_{01} \left[ (\pi_{0, stage})^{(r-1/2)} - 1 \right]}{\frac{1}{2} U_2^2}$$
 (3-13)

The work coefficient relates the isentropic head coefficient and the isentropic efficiency. It is a nondimensional value of the actual head produced by the compressor and is given as

$$\mu = \frac{c_p (T_{06} - T_{01})}{\frac{1}{2}U_2^2} \tag{3-14}$$

The relation between the head coefficient, work coefficient and the efficiency is

$$\mu = \frac{\psi}{n} \tag{3-15}$$

The static pressure recovery between any two stations 1 and 2 was calculated as the percentage of impeller peripheral dynamic (or velocity) pressure.

$$Cp = \frac{P_2 - P_1}{\frac{1}{2} \rho_1 U_2^2}$$
 (3-16)

Thus the pressure recovery of all the compressor components and the static pressure rise between various stations in the diffuser were calculated using equation (3-16). In addition to the static pressure recovery of the diffuser calculated as mentioned above, the static pressure rise from the vane leading edge station to the diffuser exit was also calculated as percentage of the dynamic pressure at the vane leading edge station.

$$Cp' = \frac{P_5 - P_3}{P_{03} - P_3} \tag{3-17}$$

The total pressure loss from the vane leading edge station to the volute exit was determined in terms of total pressure loss coefficient, which is expressed as

$$\xi = \frac{P_{03} - P_{06}}{\frac{1}{2} \rho_1 U_2^2} \tag{3-18}$$

The mass flow rate through the compressor was calculated from the differential pressure measured across the orifice as per the ASME standards. The equations used for the calculation are given in Miller (1992). In this report the mass flow rate is presented in nondimensional form known as flow coefficient which is given by

$$\phi = \frac{\dot{m}}{\rho_1 U_2 \frac{\pi d_2^2}{4}} \tag{3-19}$$

The flow angles at the impeller exit were calculated at the vane leading edge station as the static and total pressures at this station were measured. From the measured total and static pressures, the Mach number was determined

$$M_{3} = \sqrt{\frac{2}{\gamma - 1} \left[ \left( \frac{P_{03}}{P_{3}} \right)^{\left( \frac{\gamma - 1}{\gamma} \right)} - 1 \right]}$$
 (3-20)

Assuming that there was negligible heat transfer through the casing, i.e.  $T_{03}$ = $T_{06}$  and the Mach number obtained above, the static temperature at the vane leading edge station was calculated

$$T_3 = \frac{T_{06}}{1 + \frac{\gamma - 1}{2} M_3^2} \tag{3-21}$$

Now the absolute flow velocity was calculated from the basic relation that relates the total and static temperature at any point

$$C_3 = \sqrt{2c_p T_{06} \left[ 1 - \left( \frac{T_3}{T_{06}} \right) \right]}$$
 (3-22)

On the other hand, the radial component of the velocity at vane leading edge station was calculated from the continuity

$$C_{r3} = \frac{\dot{m}}{2\pi r_3 b_3} \tag{3-23}$$

The flow angle then was obtained from equations (3-22) and (3-23)

$$\alpha_3 = \sin^{-1}\left(\frac{C_{r3}}{C_3}\right) \tag{3-24}$$

However, in this calculation of flow angle, no blockage caused by the boundary layer growth was considered. Thus, the flow angles calculated were invariably higher than the actual flow angles.

### 3.5. Unsteady Performance Data Acquisition

#### 3.5.1. Obtaining and Storing the Pressure Signal

The pressure fluctuations were measured by PCB pressure transducers. The transducers in the inducer and in the impeller were mounted on the shroud wall, whereas the transducer in the diffuser was mounted on the compressor back plate. All pressure transducers were flush mounted because this eliminated any gap between the transducer diaphragm and the measurement location. Thus, no usable frequency range of the transducer was lost.

The PCB transducer uses a stack of thin piezoelectric quartz crystal wafers to convert the applied pressure on the transducer diaphragm into electric charge. The charge produced is proportional to the applied pressure. The transducer has a built-in accelerometer that compensates for any acceleration and reduces distortion and resonance in high vibration environments. The transducer also has a built-in temperature compensation that allows it to operate in a temperature range of  $-240^{\circ} C \sim +205^{\circ} C$ . The transducer can measure pressure fluctuations in a range of  $0 \sim 6.89 \times 10^{5} \text{ N/m}^2$  with 13.8 N/m² resolution. It has a natural frequency of 250 kHz with a usable frequency of up to 80 kHz.

When a constant pressure is applied to the PCB transducers for a long time (> 100 sec), the output charge does not remain constant and decreases with time. For the transducers used for experiments described in this report the output charge would be constant for about 30~60 seconds. This makes it impossible to measure the steady absolute pressure with these transducers, and they can only measure pressure fluctuations. Thus, the averaged static pressure was measured through the static taps and Validyne transducers at every plane where unsteady transducers were mounted.

The signal from the PCB pressure transducer was conducted to an inline amplifier through a 10-feet of low-noise coaxial cable. The inline amplifier conditions the transducer output signal. This amplifier has high input impedance ( $10^{11} \Omega$ ) and a range capacitor in order to avoid any distortions in the signal through input capacitance shunting.

The signal was then passed on to the signal conditioner through a 50-feet low-noise coaxial cable. Even though one inline amplifier was used for each transducer, one signal conditioner was used for all four signals. The signal conditioner powered both the inline amplifier and the PCB transducer and could also amplify the signal with fixed gain of 1, 10, 100. During the system evaluation tests, it was found that the gain had no effect on the signal to noise ratio, indicating that the noise was being added to the signal before it reached the signal conditioner. Since the signal to noise ratio was unchanged with signal gain and the amplitude of the signal was small, a gain of 100 was used to obtain better resolution of the signal.

The amplified signals from the signal conditioner were transferred to a 4-channel digital tape recorder and stored on to a tape. The stored data on to a tape were transferred

to a PC for further processing and analysis through the signal analyzer and the signal processing software. The output connectors can develop the input signals or the tape reproduction signals. The real time signals are monitored through two-channel HP signal analyzer. The HP signal analyzer also provided the capability for on-line signal analysis through the various features available with it. It was possible to obtain the power spectrum, phase and cross-correlation between two signals for on-line monitoring of the compressor. The complete signal flow path is shown in Figure 3.6.

#### 3.5.2. Signal Processing

Since the signal analyzer had only two channels, the signal capture through the signal analyzer was done in pairs of two transducers. Transducer B located in impeller was used as reference for all captures, i.e. signal from transducer B was captured through channel 1 and the signal from transducers A, C, and D was captured through channel 2 of the signal analyzer alternately at each flow point. Thus, at each flow point for a given capture frequency, three captures were made with BA, BC, and BD transducer combinations at the two channels of the signal analyzer.

Even though the captures could be made at any sampling frequency of up to 261.12 kHz per channel, but most captures were made at 12 kHz and 4096 Hz sampling frequencies. The high frequency was used to observe the blade to blade pressure fluctuations and small captures of 64 records were taken. Each record has 1024 sample points. The captures at 2048 Hz were taken to study the unsteady flow patterns in different components of the compressors. The record lengths at this frequency ranged anywhere between 8 to 64 records. The choice of either 2048 Hz or 4096 Hz was based

on the available memory of the signal analyzer and the required resolution of the capture. Moreover, literature survey has shown that in most cases the rotating stall frequency was lower than the impeller rotational frequency. The maximum rotational frequency in the present experiments was 460 Hz and with 2048 Hz sampling frequency the usable frequency range was 800 Hz and with 4096 Hz sampling frequency the usable frequency range was 1600 Hz. Unsteady signals were also recorded on digital tape so that the data can be retrieved later with various frequency ranges and give better confirmation of what happens during transients.

Once the capture was taken and stored on the PC, the signal data is processed using in-house signal processing software (UDACS). The software has various data preparation tools such as windowing, filtering, removal of mean, removal of linear trend etc. It also provides options to choose different kinds of filters and windowing methods. From the prepared data power spectrum, cross spectrum, amplitude spectrum, phase, and coherence are calculated. In addition to these features the software was also capable of graphical display of the raw data in time domain and the results or processed data in frequency domain. Following parameters were used for the computation of the spectral functions:

- 64 records from each transducer were captured
- the sampling frequency was 4096 Hz
- each record contained 1024 discrete points, which corresponds to 0.25 seconds
- all records were detrended
- a Hanning window was applied
- 50% overlapping was used

- the power spectrum, the cross spectrum, the coherence, and the phase shift were calculated
- the output is represented in terms of decibels, the reference being 1 kPa.

The details of the software and the procedures used to accomplish the results can be found in Wilmsen (1996).

# 3.5.3. Analysis of the Data

After performing all the spectral analysis, one should determine whether any

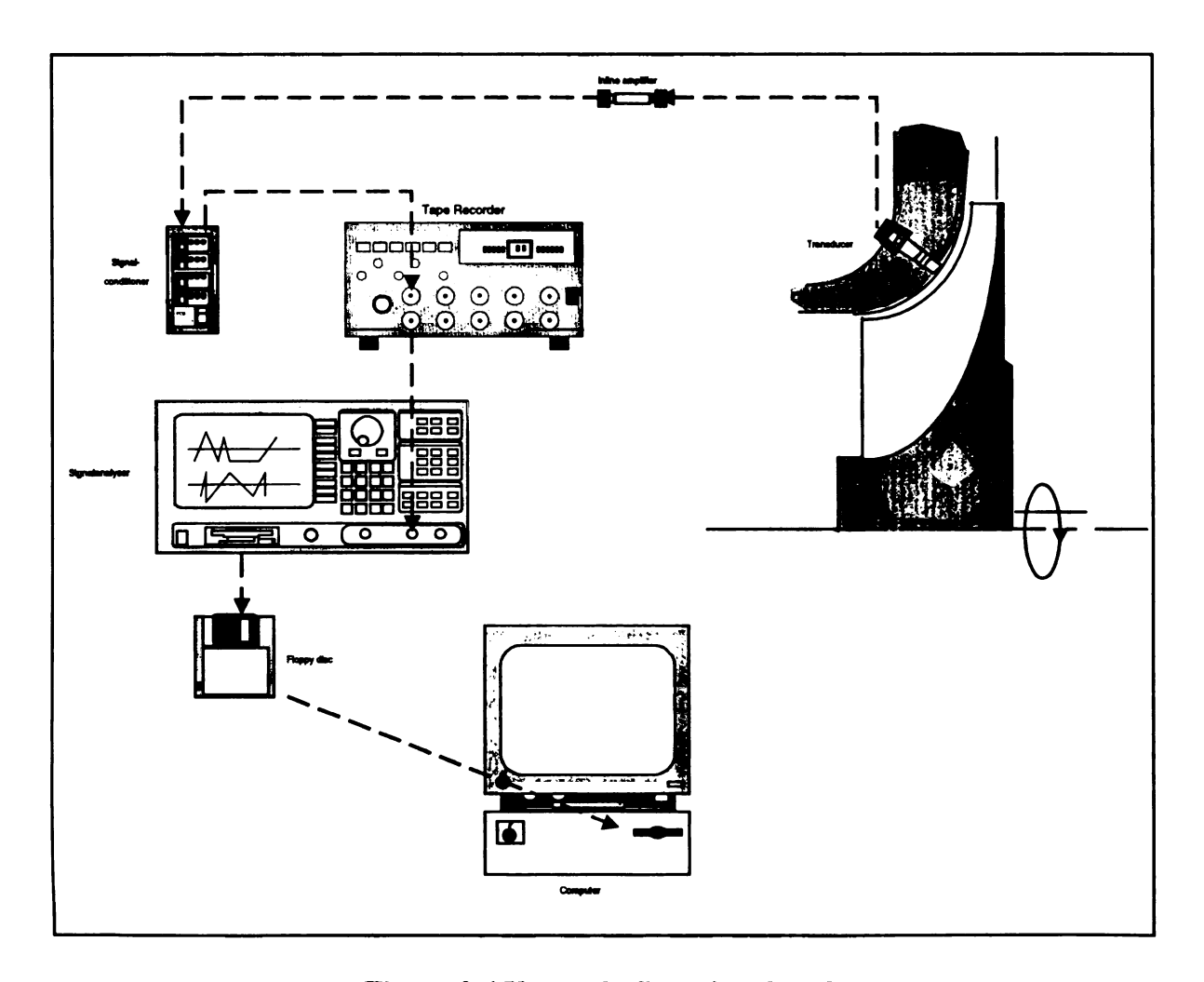


Figure 3.6 Unsteady flow signal path

peaks could be found in the power spectra. If no single peaks are present, a periodic signal can be excluded; and consequently no rotating stall can be expected. If the power spectrum increases for one operating point at all frequencies, this is a sign for a general increase of unsteadiness. But if one peak is detected, one should look at the cross spectrum of B and C, as well as at the coherence of B and C. If all graphs show the existence of a peak, the analysis described below should follow.

- If a peak is not present at all transducer locations, a surge can be excluded. If a surge occurs, the peak should be visible in all transducers.
- A peak that is present at all operating points is not due to flow phenomena.

  This may have its causes in vibrations or electrical distortions.
- If peaks occur that are not common in transducer B and C, a rotating stall in the impeller can be with good uncertainty excluded.
- B and C is close to zero, this could be a surge. Ideally, the phase shift between B and C should be zero, but the setup with a volute could possibly make the flow uneven up to the impeller and cause a small phase shift between B and C.

If a peak occurs only in the diffuser or in the inducer, a local periodic instability would be detected. It could be rotating or intermittent. This can be examined by examining the time domain. If the stall is rotating, no information about rotational speed and number of cells can be achieved, therefore a second transducer at the same radial position is necessary. But if the signal is strong enough it might be also visible in the signals from the two transducers in the impeller. A peak that is common in B and C and

where the phase shift is not close to zero could be a rotating stall. The following analysis should be performed to determine the numbers of cells.

### 3.5.3.1. Determination of the Number of Rotating Cells

The pressure fluctuations in the case of rotating stall are a function of time and circumferential position. With the simplification of a constant amplitude the pressure becomes as shown as

$$p(t,\phi) = p \cdot \sin(\omega_{st}t - m\phi)$$
 (3-25)

where  $\omega_{St}$  is the rotational speed of the stall and m is the number of lobes. For a negative number of lobes the rotational direction of the stall cells is the opposite of the direction of the rotation of the impeller.

In the casing there are the two transducers B and C at the same radial position. The signal at transducer B will reach at transducer C with a time shift of  $\Delta t$ .

$$p(t,\phi_B) = p(t + \Delta t, \phi_C) \tag{3-26}$$

in terms of fluctuation this becomes

$$\hat{p} \cdot \sin(\omega_{st}t - m\phi_B) = \hat{p} \cdot \sin(\omega_{st}(t + \Delta t) - m\phi_C)$$
(3-27)

and the number of lobes becomes

$$m = \frac{\omega_{st} \cdot \Delta t \pm k \cdot 2\pi}{\phi_C - \phi_R} \tag{3-28}$$

The product of the rotational speed of the stall cell and the time shift can be interpreted as the phase shift between the signals of the transducer signals. The

geometrical angle between the transducer is 42.5 degrees. With the phase shift information, the number of cells can be determined as shown in Table 3-3.

Table 3-3 Number of rotating stall cells.

Number of cells: m	k	Phaseshift [degree]
-6	1	105.0
-5	1	147.5
-4	0	-170.0
-3	0	-127.5
-2	0	-85.0
-1	0	-42.5
0	0	0.0
1	0	42.5
2	0	85.0
3	0	127. 5
4	0	170.0
5	-1	-147.5
6	-1	-105.0

A negative number of cells means that the rotating direction of the stall cells is the opposite to that of the impeller. If the number of cells is positive, the cells rotate in the same direction as the impeller.

$$\omega_{cell} = \frac{\omega_{st}}{m} \tag{3-29}$$

The rotational frequency of the cells can be found by dividing the frequency of the pattern by the number of cells.

## 4. EXPERIMENTAL RESULTS OF STEADY PERFORMANCE

Four low solidity vaned diffusers (LSVD5 through LSVD8) were tested downstream of the same impeller. Testing was conducted at three rotating speeds (M<sub>u</sub>=0.69, 0.88, and 1.02), each from maximum flow rate to surge flow with a minimum of 9 operating points per speed line. The results of this testing are presented here. Amineni (1996) designed and performed tests on the vaneless diffusers, conventional vaned diffuser and LSVD1 through LSVD4 with the same configuration.

The overall performances of each of these diffusers are compared with each other in order to understand the advantages and disadvantages of three types of diffusers used in centrifugal compressor stages. In addition, the flow range of operation, peak efficiency obtained by the low solidity vaned diffusers is compared with the vaneless and conventional vaned diffusers. Moreover, the effects of the LSVD vane number, the solidity, and the turning angle on the overall performance of the compressor stage are also discussed. All the performance curves are normalized with respect to the design flow of VNL1 running at  $M_u = 1.02$ .

#### 4.1. Overall Performance Characteristics

In this work four low solidity vaned diffusers (LSVD5 through LSVD8) were experimentally tested downstream of the same impeller at three different speeds corresponding to the impeller tip Mach number (M<sub>u</sub>) of 0.69, 0.88 and 1.02.

The overall performance of each of these four diffusers is compared with each other in order to enumerate the advantages and disadvantages of the three types of diffusers used in centrifugal compressor stages. In addition, the range of operation, peak efficiency and the pressure rise obtained by the low solidity vaned diffusers were compared with the vaneless and conventional vaned diffusers.

The performance characteristics of the compressor stage with LSVDs along with both vaneless and vaned diffusers at three different speeds are shown in Figure 4.1, Figure 4.2, and Figure 4.3 at the impeller tip Mach number of 1.02, 0.88, and 0.69 respectively.

At  $M_u = 1.02$  in Figure 4.1, the characteristic curves of the VNLs and all the LSVDs are vertical at the right end, with the mass flow rate being approximately constant for all these diffusers. On the other hand, the maximum flow rate attained by the stage with CVND was about 14% less than the other diffusers. This clearly indicates that the maximum flow through the compressor was controlled by the vaned diffuser throat choke in case of the CVND while the inducer choke, which will be discussed in the next chapter, in case of both the vaneless and the low solidity vaned diffusers. However, at lower speeds ( $M_u = 0.88$  and 0.69) than designed it can be noticed that their overload capacity decreased with the speed even though the LSVDs lack a true diffuser throat. This decrease in overload capacity of the compressor with LSVDs resulted from the high

negative incidence flow on the vanes at lower than design speed. The high negative incidence causes the pressure side stall of the LSVD vanes, which can be shown from the numerically simulated results in Chapter 6. The vanes along with the stalled flow form a virtual throat which limits the maximum possible flow through the compressor, similar to the CVND.

The VNL1 shows better stall margin than did VNL2 at all speeds. This is because the flow is more radial than VNL2 at a given flow rate. VNL1 is narrower in terms of width by 18% than VNL2, which makes the flow more radial leading to shorter fluid path. The LSVDs didn't exhibit surge flow rate equivalent to VNL1, contrary to the observations of Hayami et al. (1990) and Senoo et al. (1983) ( $\theta = 10^{\circ}$ ). The reason for this difference could be that the LSVD vanes in the present test had higher turning angle ( $\theta$ ) up to 14.6° and were made of thin flat plates which are more sensitive to incidence.

The efficiency of the compressor with LSVDs was better than the vaneless diffusers for a wide range of flow at all speeds. Among LSVDs, LSVD5 achieved highest peak efficiency at all speeds at the cost of flow range. At  $M_u = 0.69$  the LSVD5 achieved slightly better peak efficiency than the CVND. However, LSVD8 (0.6 solidity) didn't show any advantage over the vaneless diffuser in terms of both the efficiency and the flow range at  $M_u = 0.69$ . LSVD8 has the lowest turning angle (9.9°) among the tested diffusers and it has high negative incidence at high flow and  $M_u = 0.69$ . It might be predicted that the low solidity vaned diffuser with higher vane setting angle would achieve both better efficiency and the overload capacity at lower speed than design while the stall margin would suffer. LSVD5 has a solidity of 0.9, which is the maximum solidity for being a low solidity vaned diffuser. Moreover, it can also be seen that the

peak efficiency of the LSVDs at all speeds was attained at higher mass flow than the CVND. Thus LSVD provides greater stable operating range between peak efficiency flow point and surge flow.

In general at all speeds the efficiency and the pressure ratio of the compressor with LSVDs were superior to the best performing vaneless diffuser over a wide flow range. The flow range obtained by the LSVD was also comparable to the vaneless diffusers. Thus LSVD gives greater flexibility in design as they can be adjusted to peak in performance over a wide range of impeller flow conditions.

#### 4.1.1. Effect of Solidity

Figure 4.4(a) to (c) show the effect of solidity on the performance at three different rotational speeds. It is shown in Figure 4.4(a) that the flow range increases as the solidity decreases and the vaneless diffusers have the widest flow range. If the flat plate vane of LSVDs were replaced by streamlined airfoil, the LSVDs would achieve the better flow range. The flow range decreases with the impeller tip Mach number. In the present work a reduction in solidity caused a reduction in blade turning angle as the number of vanes was kept constant at 18. This can be attributed to the decrease in blade turning angle. However, it seems that the peak efficiency rises with the solidity in Figure 4.4(b). Also it can be known that the stage with LSVD having the flat plate vane offers good performance at lower speed.

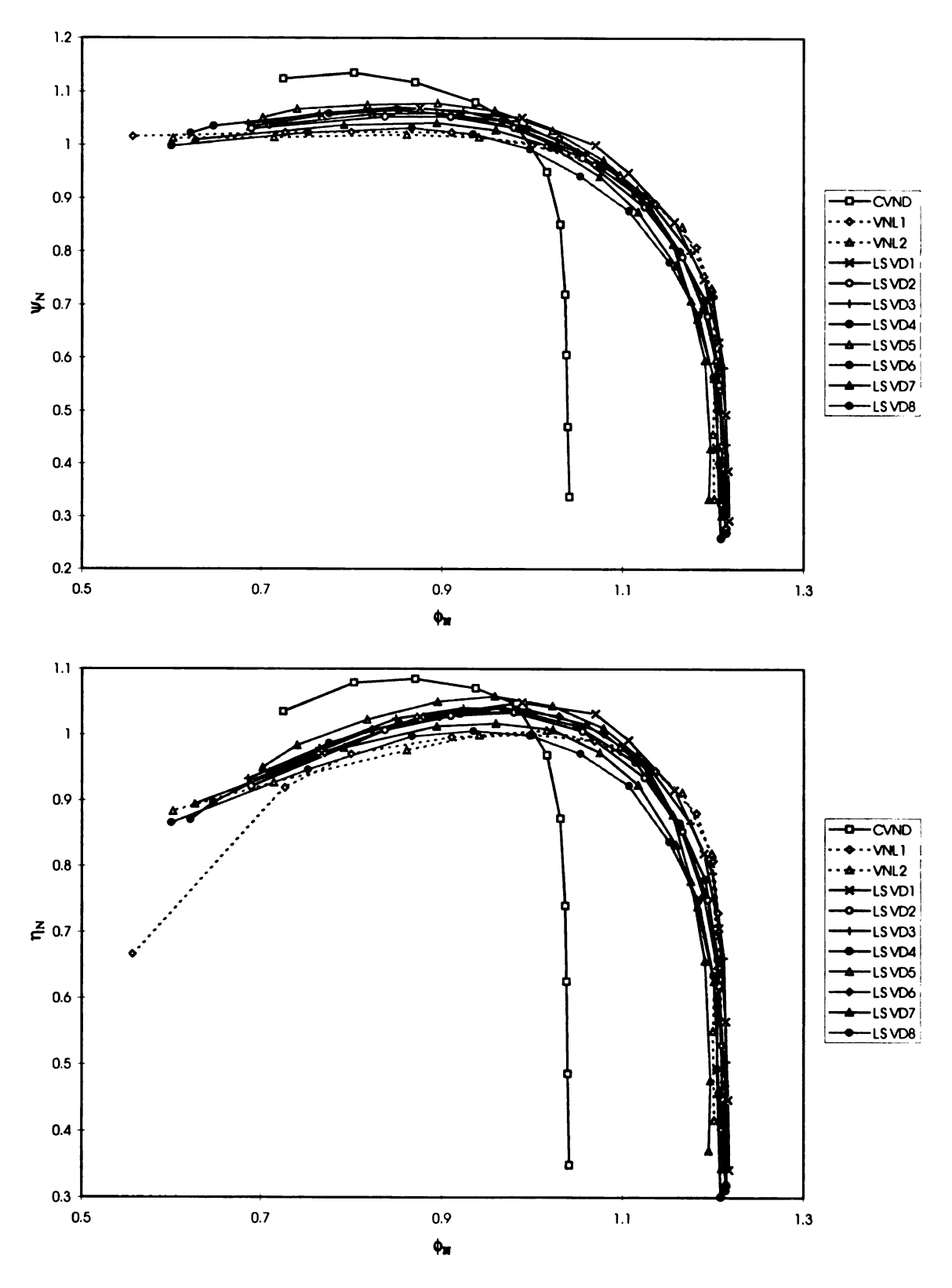


Figure 4.1 Performance characteristics of the stage at  $M_u$ =1.02

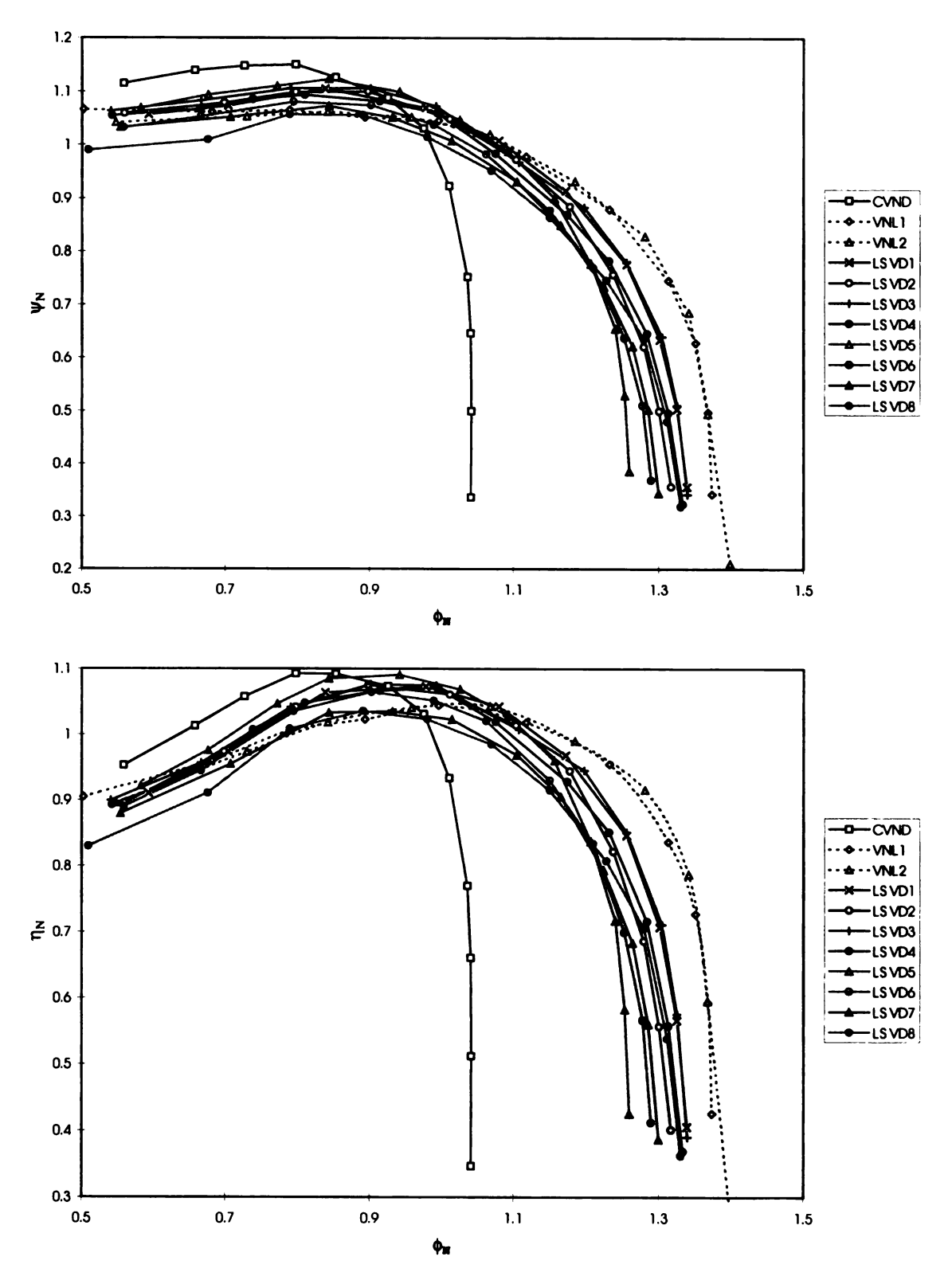
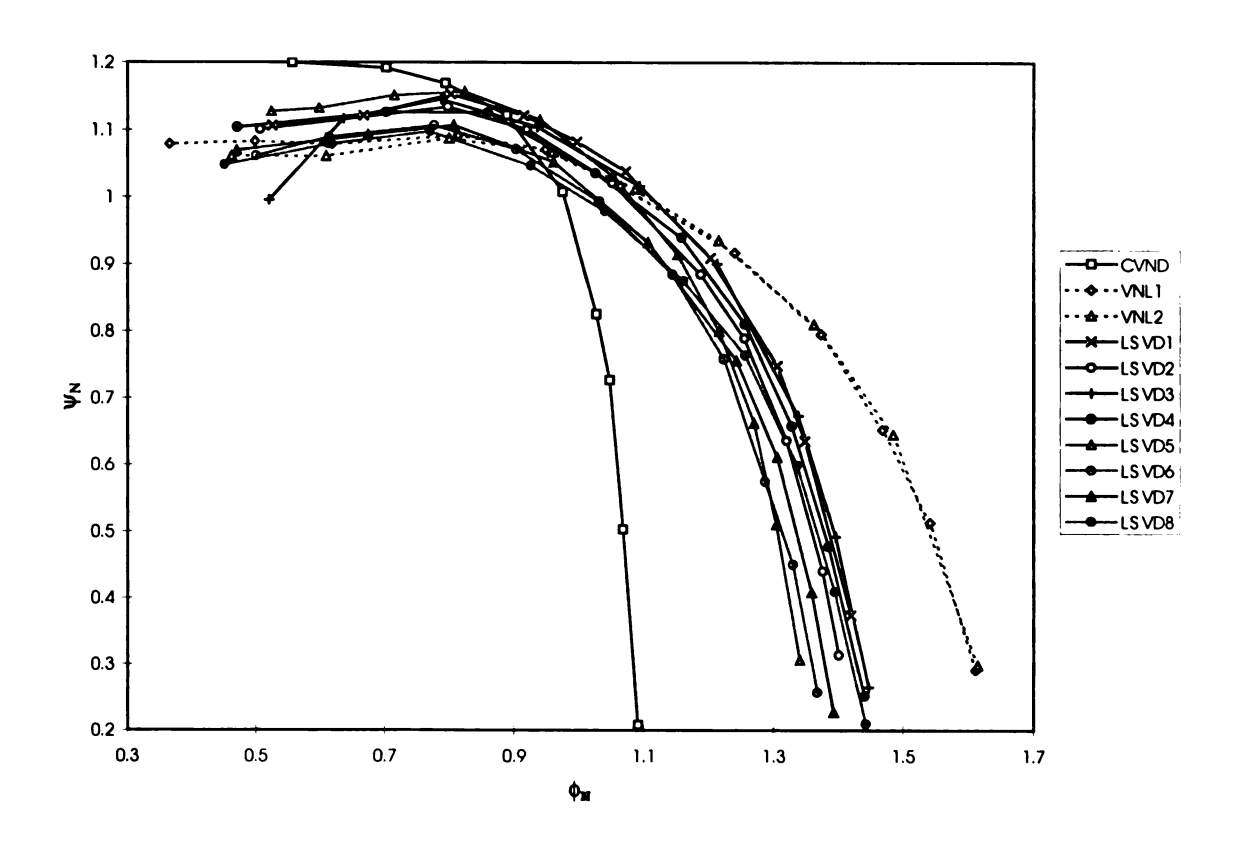


Figure 4.2 Performance characteristics of the stage at  $M_u$ =0.88



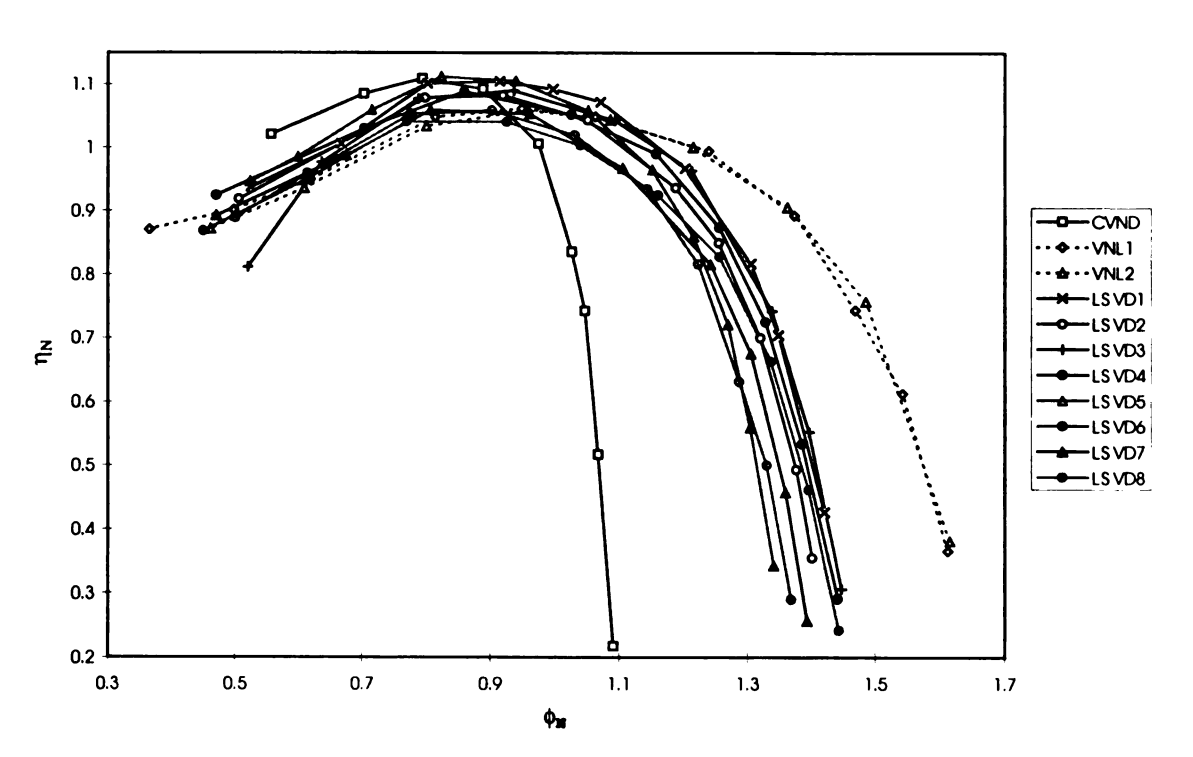
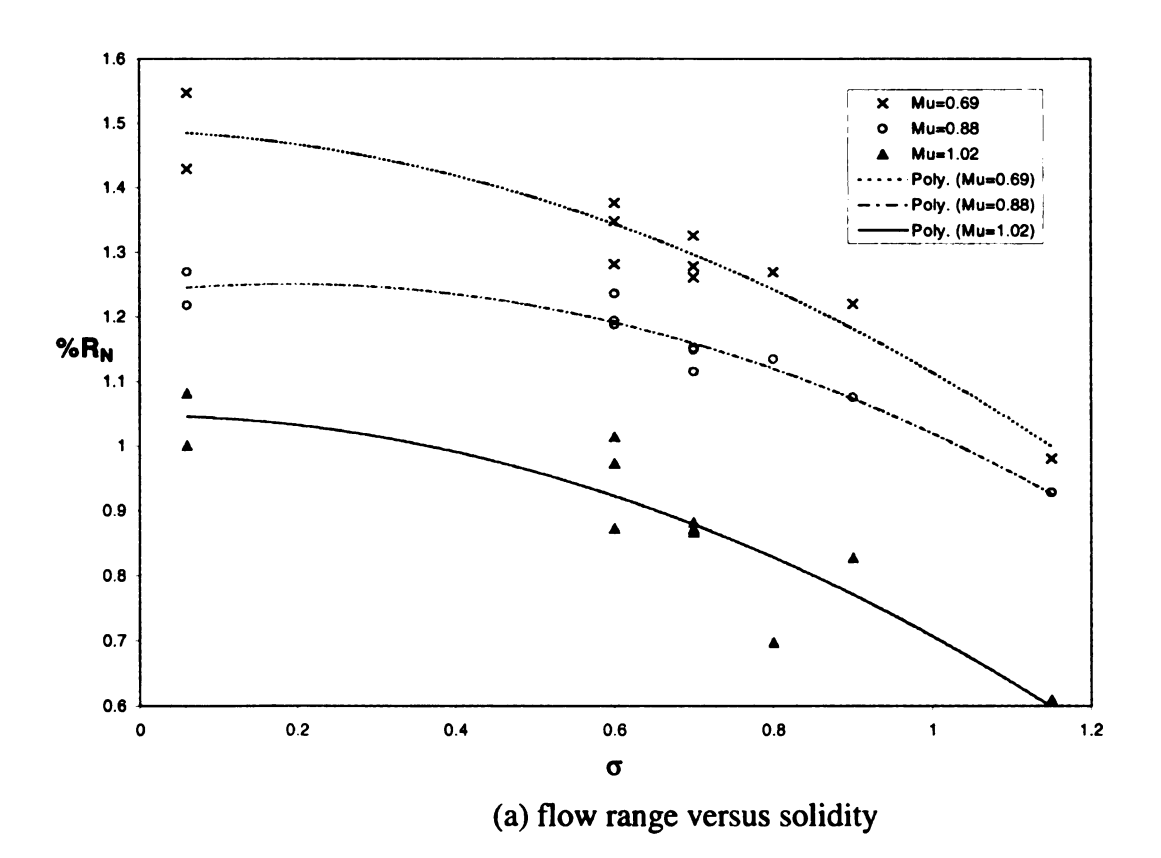
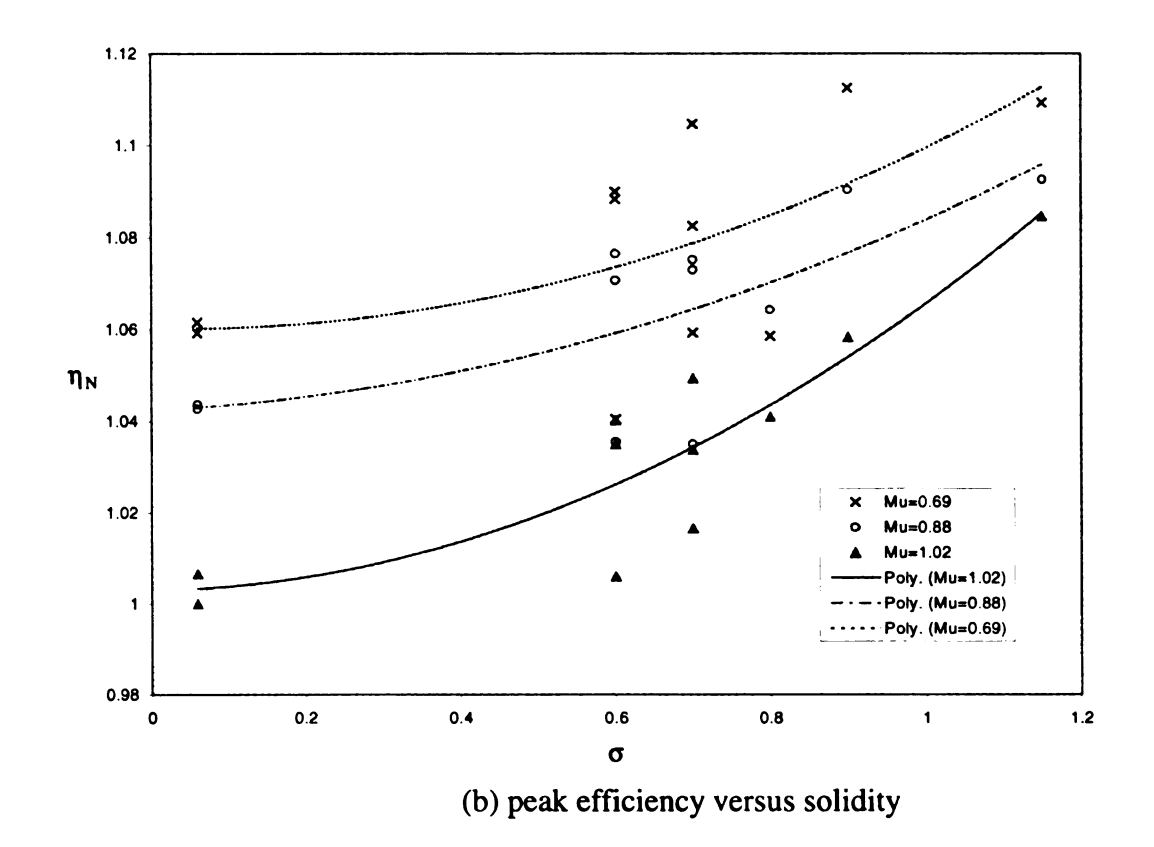


Figure 4.3 Performance characteristics of the stage at  $M_u$ =0.69

This is because of lower density increase at lower speed. At higher speed, the flow angle tends to decrease faster as the flow diffuses within the diffuser. The higher speed compressor, the less turning angle vane should be used or the vane should be curved. At M<sub>u</sub>=0.69, there is small difference both in peak efficiency and pressure recovery (Figure 4.4(c)). As impeller speed increases, the differences become higher. One interesting thing in Figure 4.4(c) is that the trendlines of pressure recovery at the different speeds encountered around the solidity of 0.35 and showed the lowest pressure recovery. The diffuser with higher solidity than 0.35 would achieve better pressure recovery with the impeller tip speed and vice versa one with lower than 0.35.

In general, the higher solidity diffuser shows the better pressure recovery and this can be a cause of a stall at a higher flow rate.





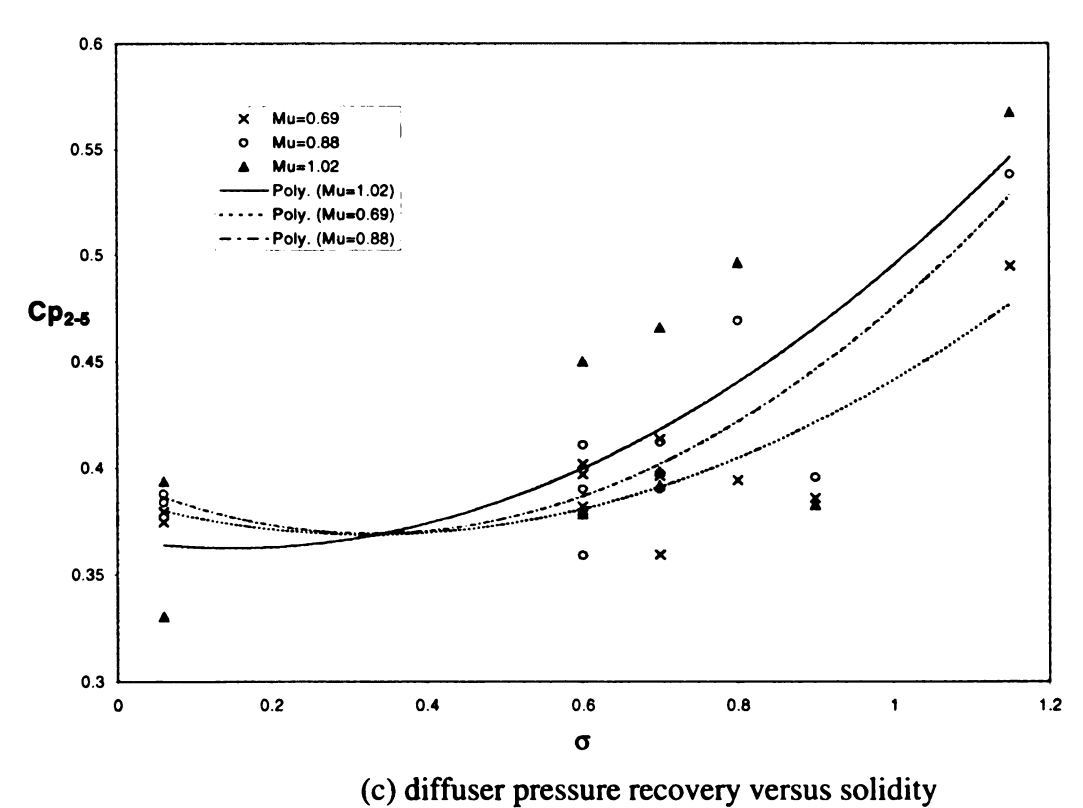


Figure 4.4 Effect of solidity on the performance

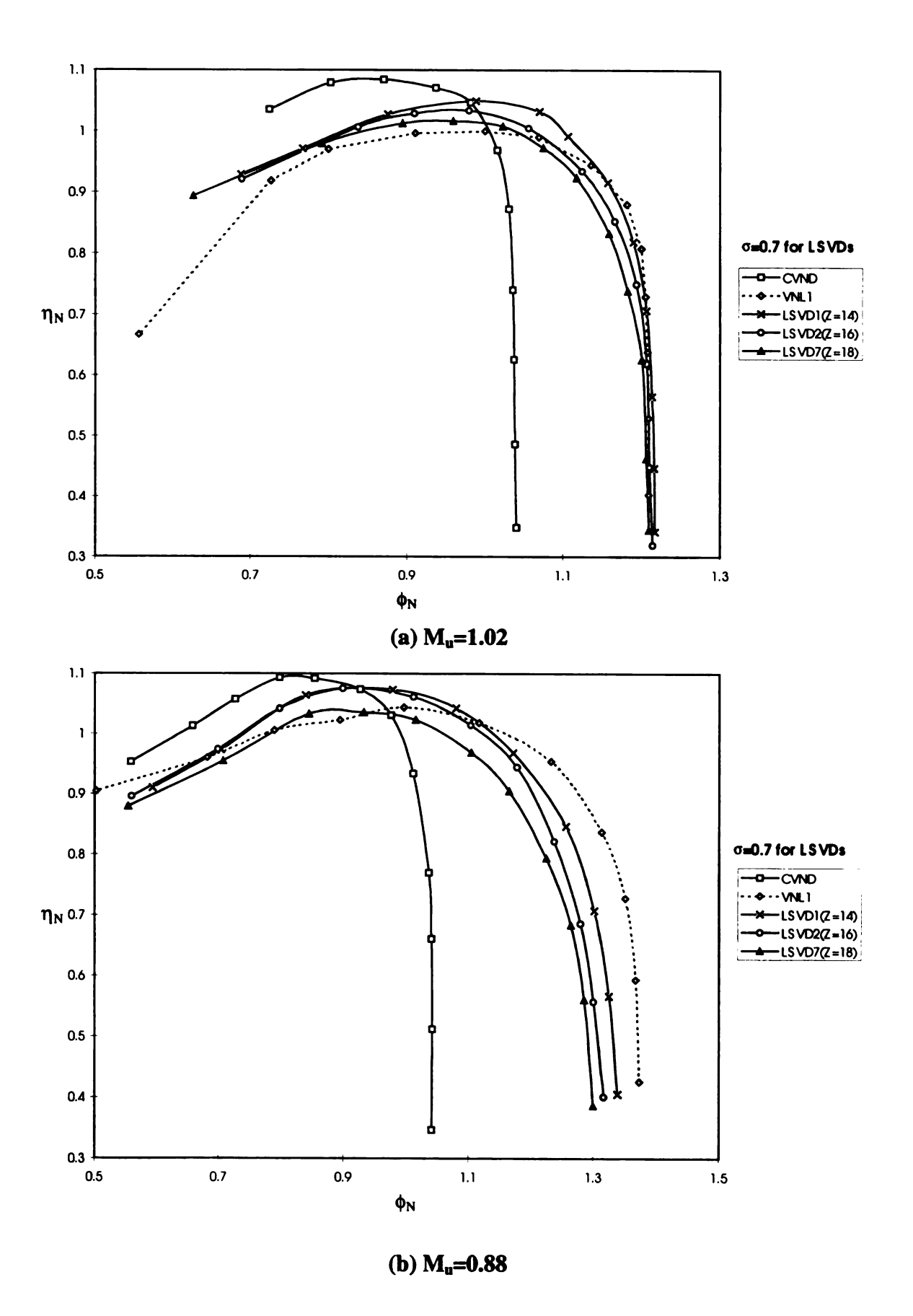
80

#### 4.1.2. Effect of Vane Number

Figure 4.5(a) to (c) show the effect of vane number on the performance of the stage with the low solidity vaned diffusers of 14-vane, 16-vane, and 18-vane having the same solidity of 0.7 at three different speeds. It is shown in Figure 4.5(a) that the overload capacities of the stage with vaneless diffusers and LSVDs are the same and 14% less for that with the vaned diffuser due to the choke at the diffuser throat.

The overload capacities of the stage with VNLs and LSVDs at M<sub>u</sub>=1.02 correspond to the inducer choke. However, the stage with the LSVD with less number of vanes has slightly better overload capacity and this becomes more clear at lower speed. However, when it comes to the stall margin the stage with fewer vane number of LSVD is better. For a fixed solidity and blade inlet angle, reduction in blade number causes an increase in blade turning angle and accordingly in blade loading. The surge margin was improved by increasing the number of vanes at a fixed solidity. It can be explained that the shorter vane allows the higher positive incidence angle because of smaller turning angle.

At all speeds, the LSVD with less vanes attain the best peak efficiency. This might be due to the higher blade turning angle which results in a shorter flow path to reduce friction losses and causes more flow diffusion which reduces losses in the volute.



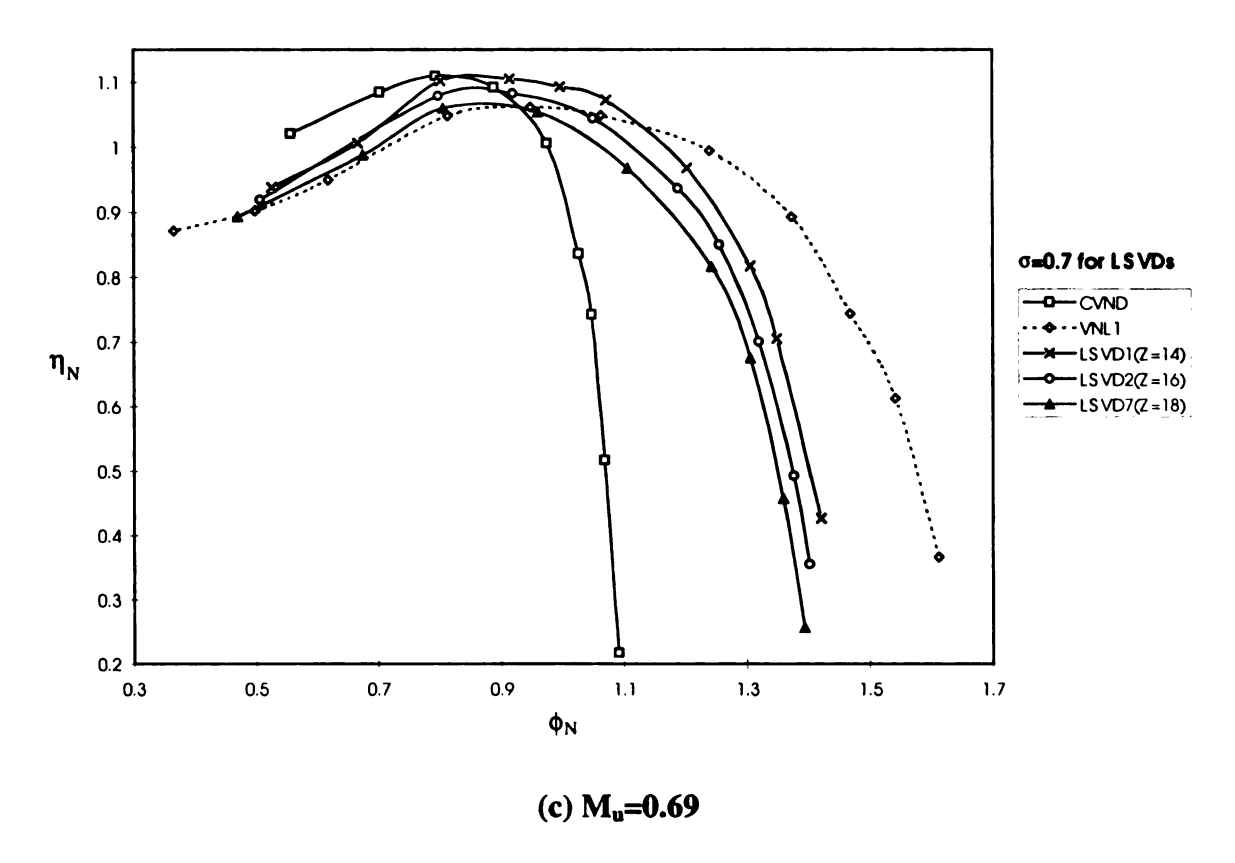


Figure 4.5 Effect of vane number on the performance

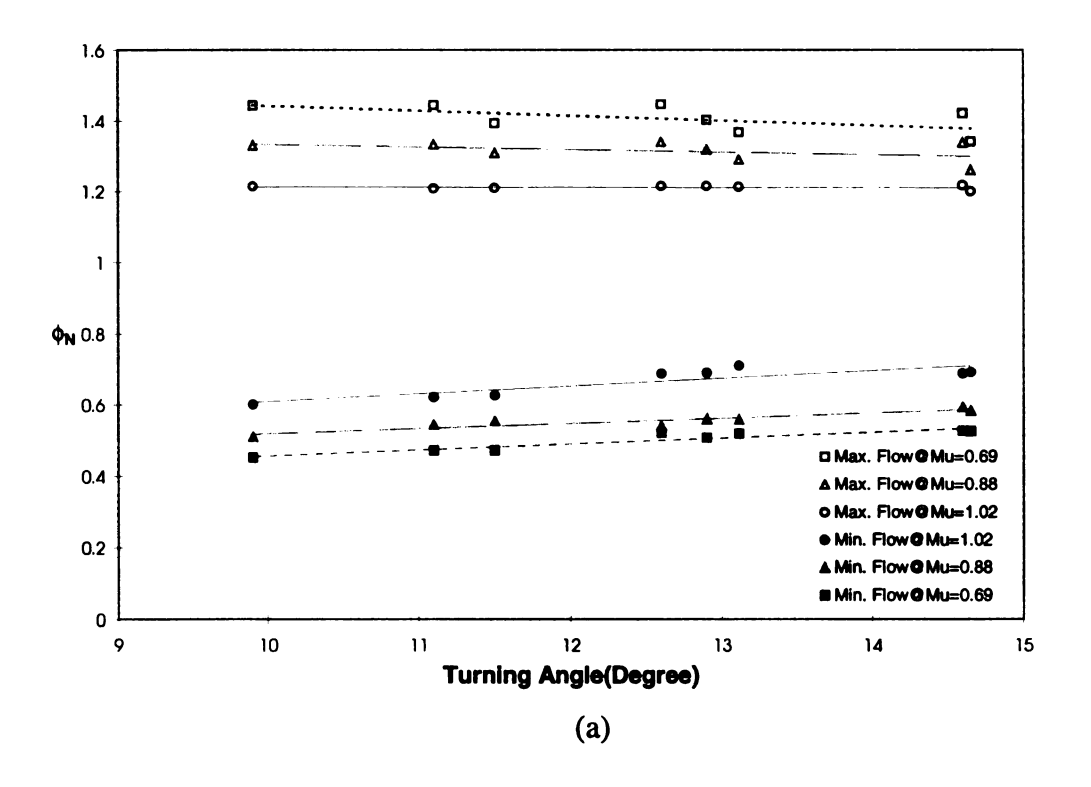
# 4.1.3. Effect of Turning Angle

Figure 4.6(a) and (b) show the influence of the turning angle of eight different LSVDs on flow range and the peak efficiency, respectively at different rotational impeller speeds regardless of vane number, solidity.

From Figure 4.6(a), the overload capacities of the stage running at  $M_u$ =1.02 with LSVDs (marked by circles) lie in almost horizontal straight line indicating the inducer choke. All LSVDs have almost the same overload capacity except LSVD5 which has the highest turning angle of 14.64° and the highest solidity of 0.9. LSVD1 has turning angle of 14.66° similar to LSVD5 with solidity of 0.7. Thus decrease in overload capacity of

LSVD5 resulted from virtual throat choke caused by high solidity for a low solidity vaned diffuser. The virtual throat was generated by the pressure side stall. This can be seen from the numerical simulation results. As rotational impeller speed decreases, the stage with LSVDs having the lower turning angle show better overload capacity. The decrease in overload capacity results from negative incidence flow to the vane leading edge at lower than design speed. It can be seen from Figure 4.6(a) by filled circle, triangle, and square that the stage with LSVD having higher turning angle exhibits the higher surge flow rate due to excessive diffusion. At all speeds, the flow range gets narrower as the turning angle increases.

The data are somewhat scattered in Figure 4.6(b), the higher the turning angle, the higher the peak efficiency.



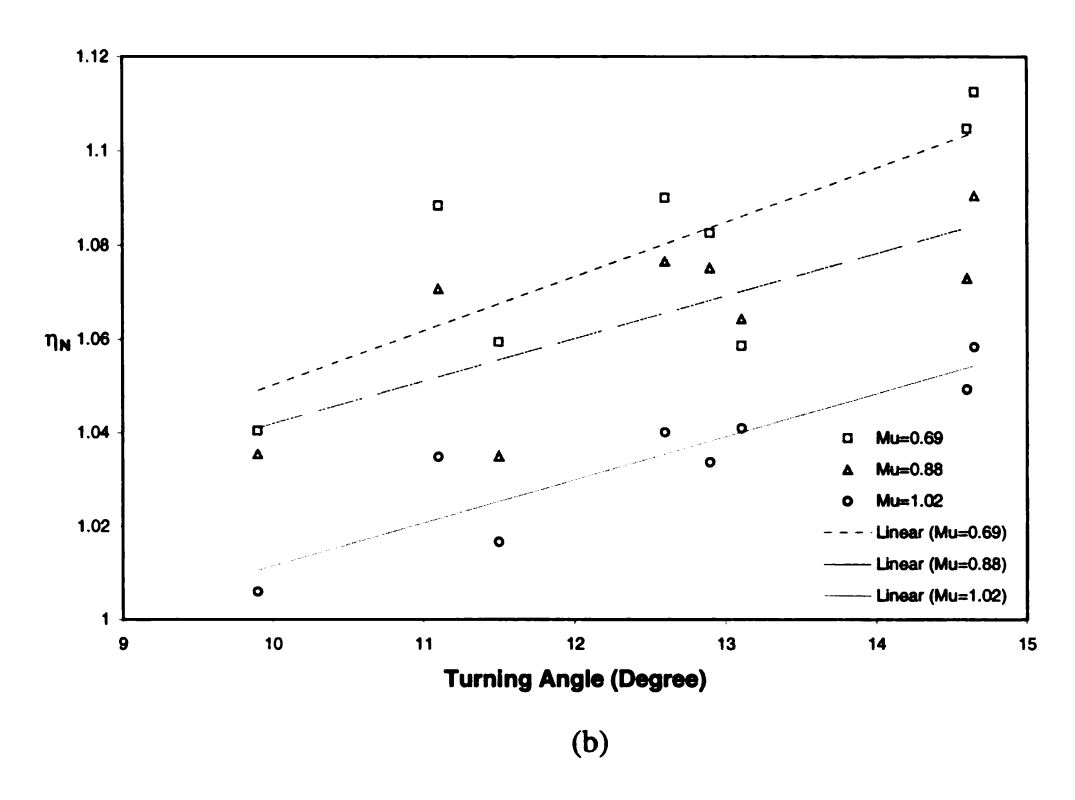
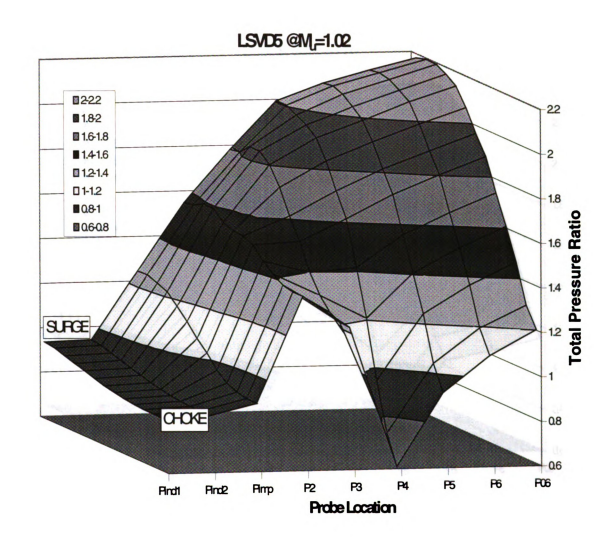


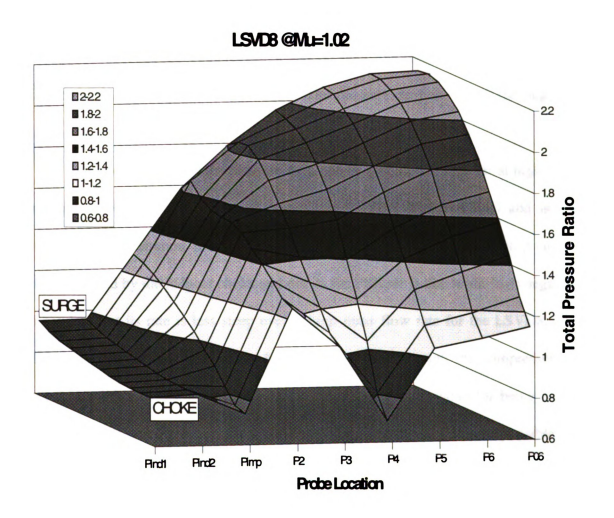
Figure 4.6 Effect of turning angle

## 4.2. Pressure Rise in the Stage with the Low Solidity Vaned Diffusers

In an attempt to understand the pressure rise in the stage with the low solidity vaned diffusers, the static pressure from stage inlet to exit measured at eight different locations are shown and discussed regarding to the factor limiting the flow. There is no significant observed difference in terms of pressure rises among all four low solidity vaned diffuser configurations at the different rotational speeds. Thus the data of LSVD5 and LSVD8 are shown only for the rotational speed of  $M_u = 1.02$  and discussed. In Figure 4.7 the ratio of the static pressure to the stage inlet total pressure is plotted, with respect to the different locations at which the pressure measurements were made for different operating flow points.



(a) LSVD5



(b) LSVD8

Figure 4.7 Pressure rise in the stage with the low solidity vaned diffuser

From the static pressure characteristics of LSVD5 (Figure 4.7(a)), the pressures from stage inlet to the diffuser inlet are constant for the first two operating points. However from diffuser inlet to stage exit the pressure rise is different each other, thus indicating that neither the inducer nor the impeller is responsible for limiting the maximum flow through the compressor. It can be seen that there is a sudden pressure drop in the diffuser at high mass flow rates. The pressure drop is due to the negative incidence loss.

In Figure 4.7(b) the sudden pressure drop can be seen in the impeller at high mass flows (Op#1 to Op#3), which can not be seen in LSVD5 (Figure 4.7(a)) and in the diffuser, which is common for both LSVD5 and LSVD8. The pressure drop in the impeller is caused by the inducer choke and one in the diffuser is due to the high negative incidence loss but its rate is less steep even a high mass flow rate for the LSVD8. The LSVD8 is not the limiting component for maximum flow through the compressor. In chapter 2, a solidity of 0.936 is determined to be the maximum value for being a low solidity vaned diffuser. However, the LSVD5 having a solidity of 0.9 is responsible for limiting the maximum flow. At high mass flow rates the flow has a high negative incidence on the vanes due to which the flow separates on the pressure side and forms a large stalled region. This large stalled flow blocks a major area between two vanes forming a virtual throat and causing the flow to accelerate.

The pressure rise characteristics of LSVD8 is a mixture of the characteristics of VNLs and CVND, which are not shown here. It can be seen that the sudden pressure drop occurs both in the impeller and in the LSVD8 at high mass flow rate. However the

maximum flow rate attained by the stage with LSVD8 was equivalent to that of the VNLs as seen in performance characteristics (Figure 4.1).

#### 4.3. Pressure Recoveries in the Diffusers

Figure 4.8 through Figure 4.10 show the pressure recovery (Cp<sub>2-5</sub>) in the various diffusers at all speeds. At all speeds it can be seen that the pressure recoveries of VNLs remains almost constant with respect to the flow rate and the CVND has the highest peak pressure recovery. The pressure recovery of the LSVDs at all speeds is in between the VNLs and the CVND. It can also be observed that the LSVDs have the pressure recovery trend similar to the CVND, which is because of the negative incidence loss at high mass flow rates. The LSVD with higher solidity or turning angle tends to yield higher Cp<sub>2-5</sub> at high mass flow rates at all speeds. This can be expected because of lower losses and blockage by the stall on the pressure surface of each vane. On the other hand at low mass flow rates, the LSVD with lower solidity seems to offer better Cp<sub>2-5</sub>. At the left ends of the figures, the irregular trends came from erroneous pressure at the diffuser inlet (P<sub>2</sub>). This reading was affected by the suction side of the vane leading edge where the pressure changes drastically along the vane leading edge radius. At  $M_u = 0.88$  the irregular trends are clearly observed for all LSVDs and CVND in Figure 4.9. The next subsection attempts to explain such observations by breaking the pressure recovery of the diffuser Cp<sub>2-5</sub> into the pressure recovery of two different regions.

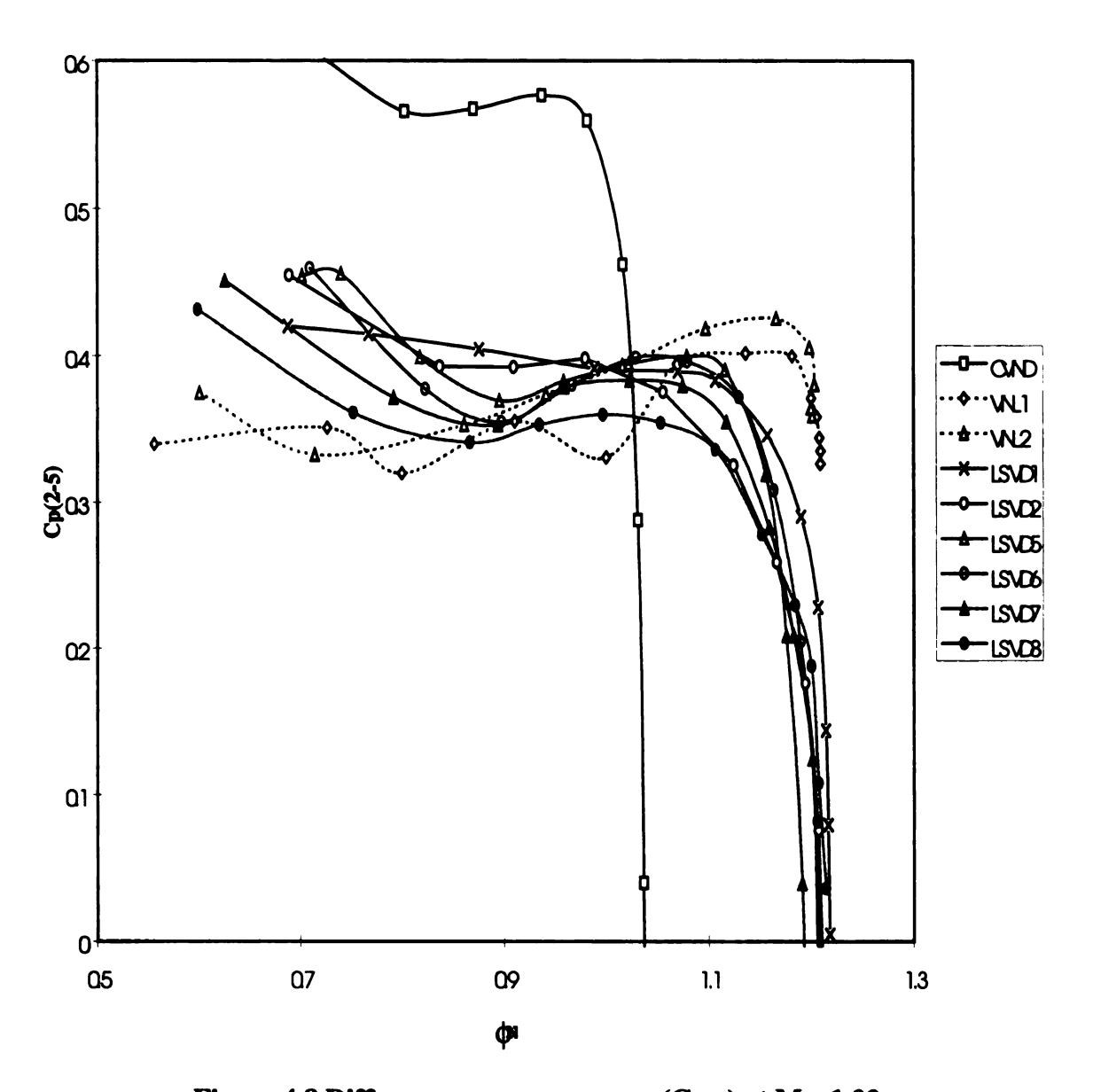


Figure 4.8 Diffuser pressure recovery ( $Cp_{25}$ ) at  $M_u$ =1.02

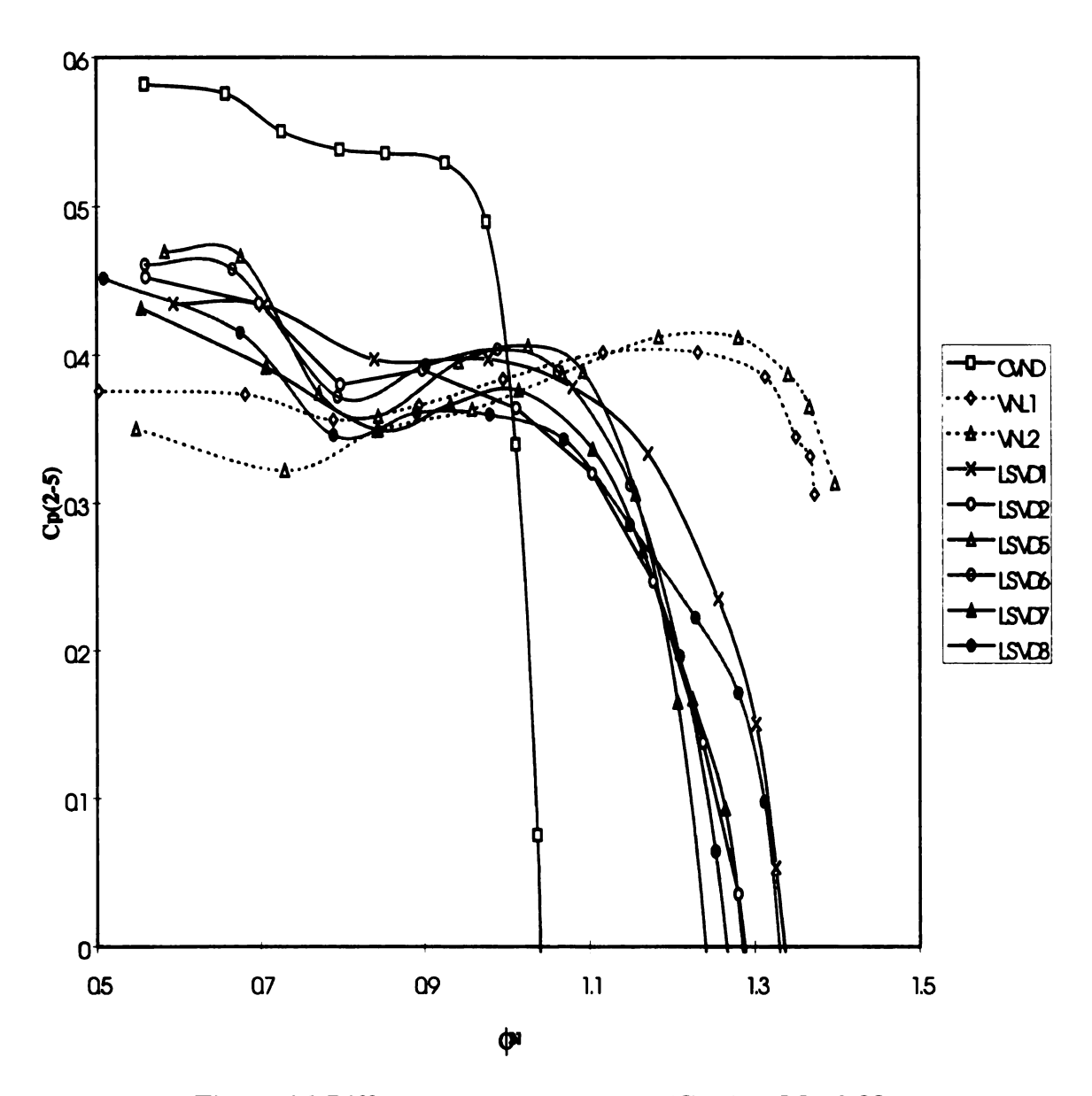


Figure 4.9 Diffuser pressure recovery (Cp<sub>25</sub>) at  $M_u$ =0.88

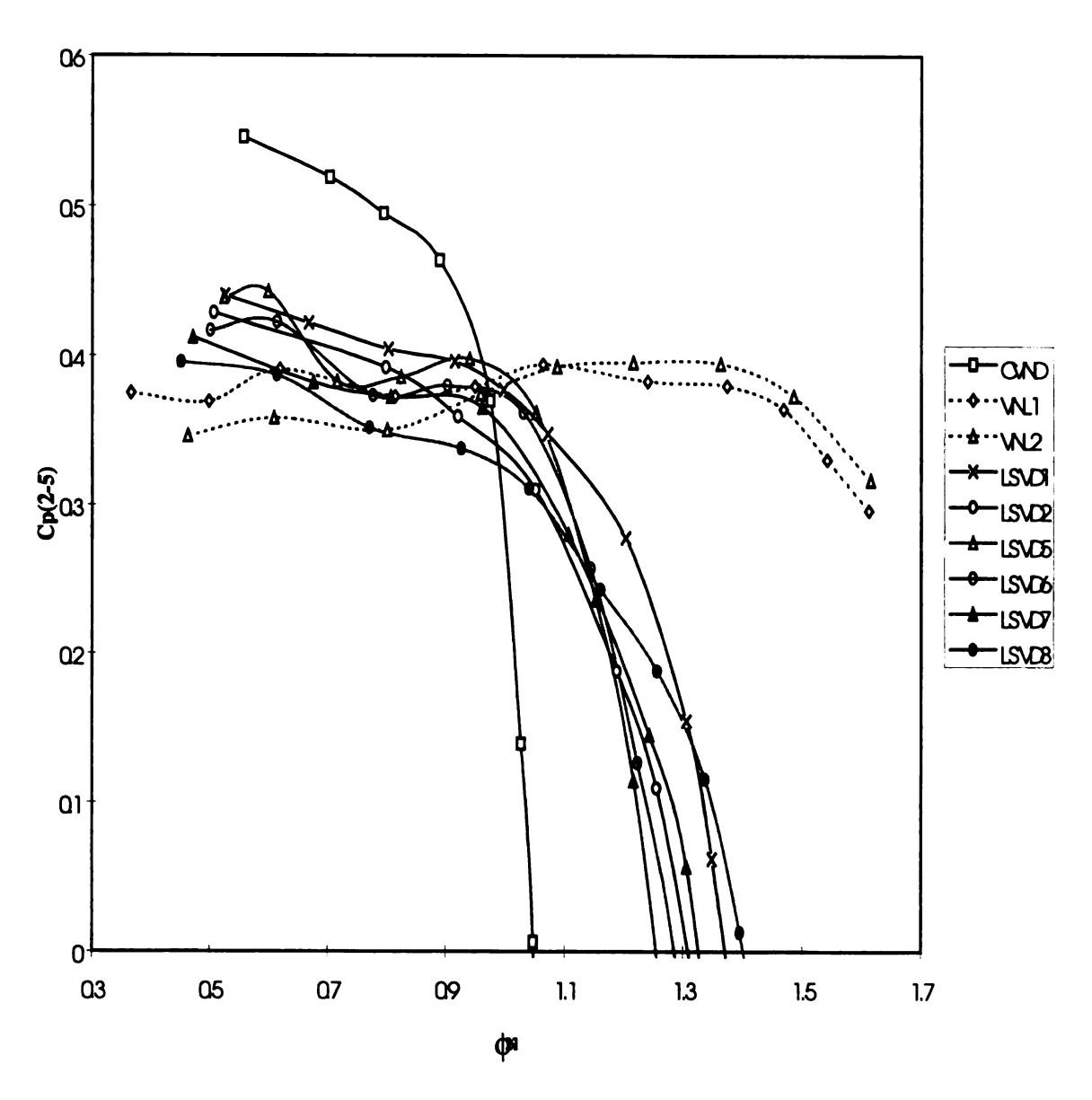


Figure 4.10 Diffuser pressure recovery (Cp<sub>25</sub>) at  $M_u$ =0.69

#### 4.3.1. Subdivided Pressure Recoveries

In an attempt to understand the detailed pressure recovery in the low solidity vaned diffuser the diffuser was subdivided. Generally the vaned diffuser can be divided into three parts: upstream vaneless space, vaned region, and downstream vaneless space. As can be seen from the numerical calculation, the pressure around the leading edge changes drastically at the same radius. So the diffusers are subdivided into two parts: (1) upstream vaneless space and vaned region and (2) downstream vaneless space. In this Figure 4.11 through Figure 4.13 show the subdivided pressure recoveries in the different diffusers at three different impeller speed. At the top (a)s represent the pressure recoveries of upstream vaneless space and vaned region, and (b)s for downstream vaneless space. It can be seen that the pressure is recovered in the downstream vaneless space of CVND and LSVDs at high mass flow rate, while the pressure is lost. However, as the flow rate decreases, Cp<sub>24</sub> increase rapidly for a short flow rate decrement and then gradually up to optimum point. It can be known by comparing Cp<sub>24</sub> and Cp<sub>45</sub> One interesting can be found for VNLs, which is almost zero pressure recovery between upstream vaneless space and vaned region at high mass flow rate. The radius ratio of P<sub>4</sub> probes are 1.21 and the corresponding flow angles for VNL1 are between 45.6° ~ 55.7°. The pressure recovery of the vaneless diffusers at high mass flow rate is a contribution of the diffusion from a certain radius ratio. As the flow decreases, Cp<sub>45</sub> decreases slowly and Cp<sub>24</sub> increases for a short flow rate decrement and remains almost constant. However,

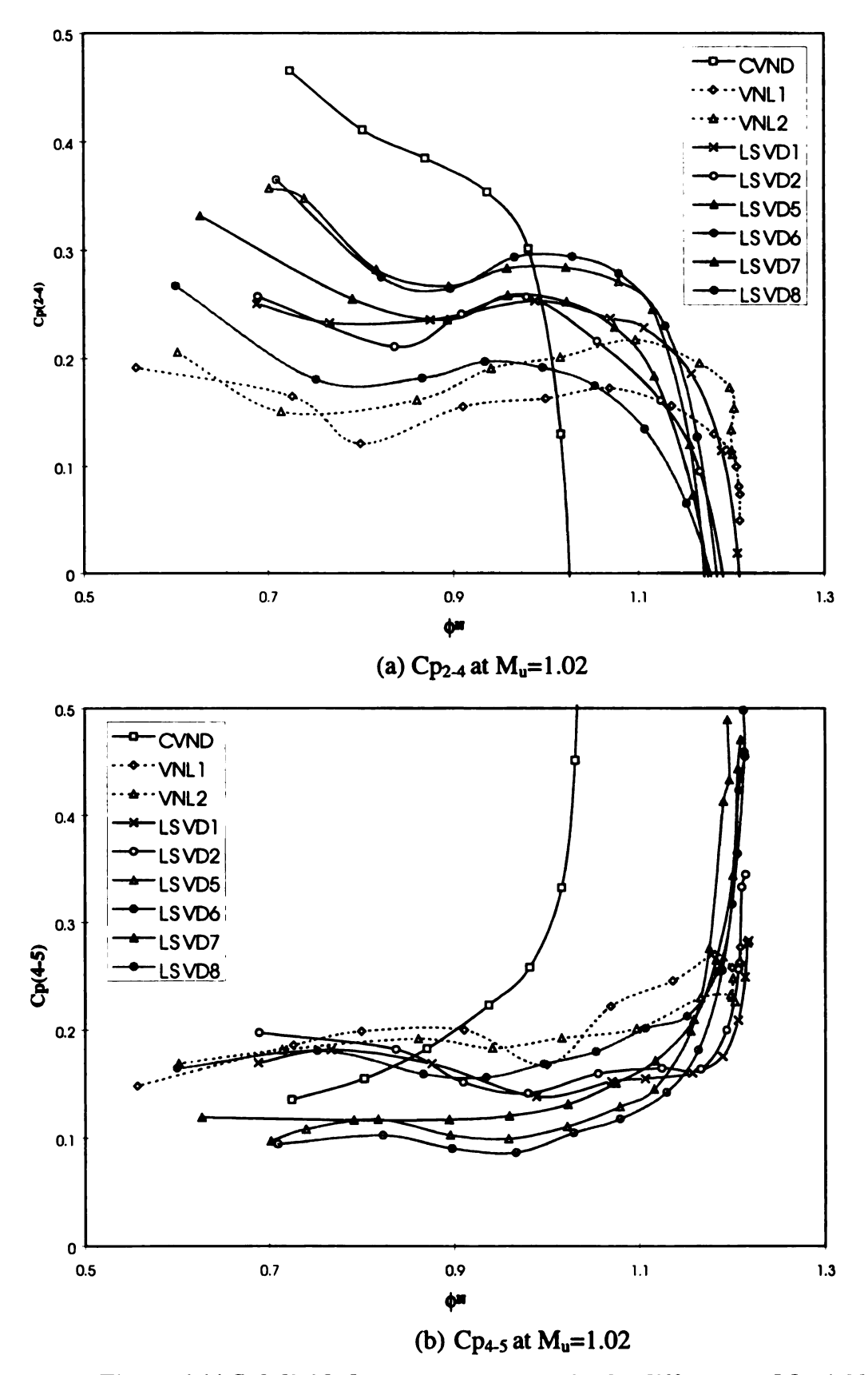


Figure 4.11 Subdivided pressure recovery in the diffusers at  $M_u$ =1.02

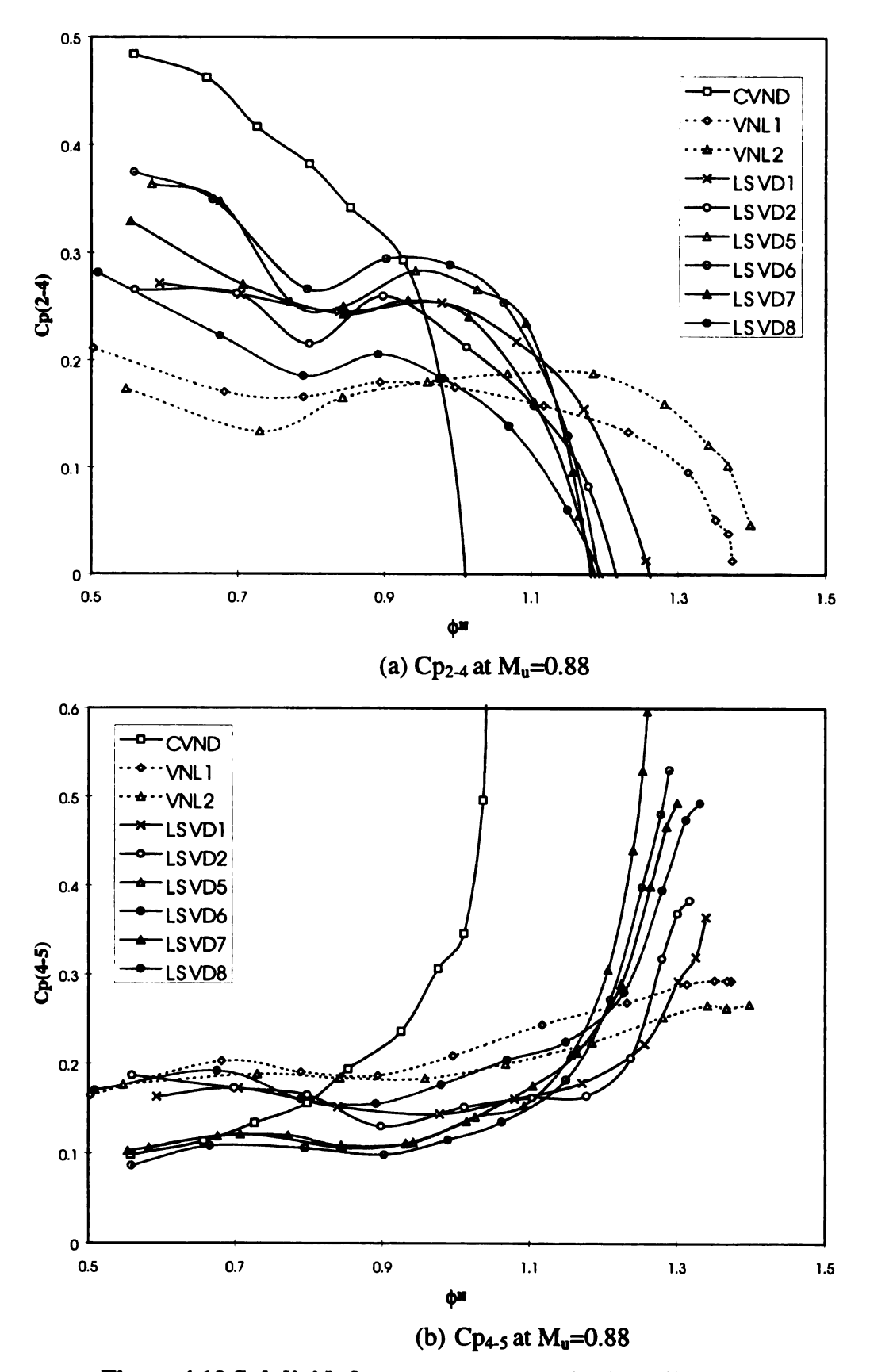


Figure 4.12 Subdivided pressure recovery in the diffusers at  $M_u$ =0.88

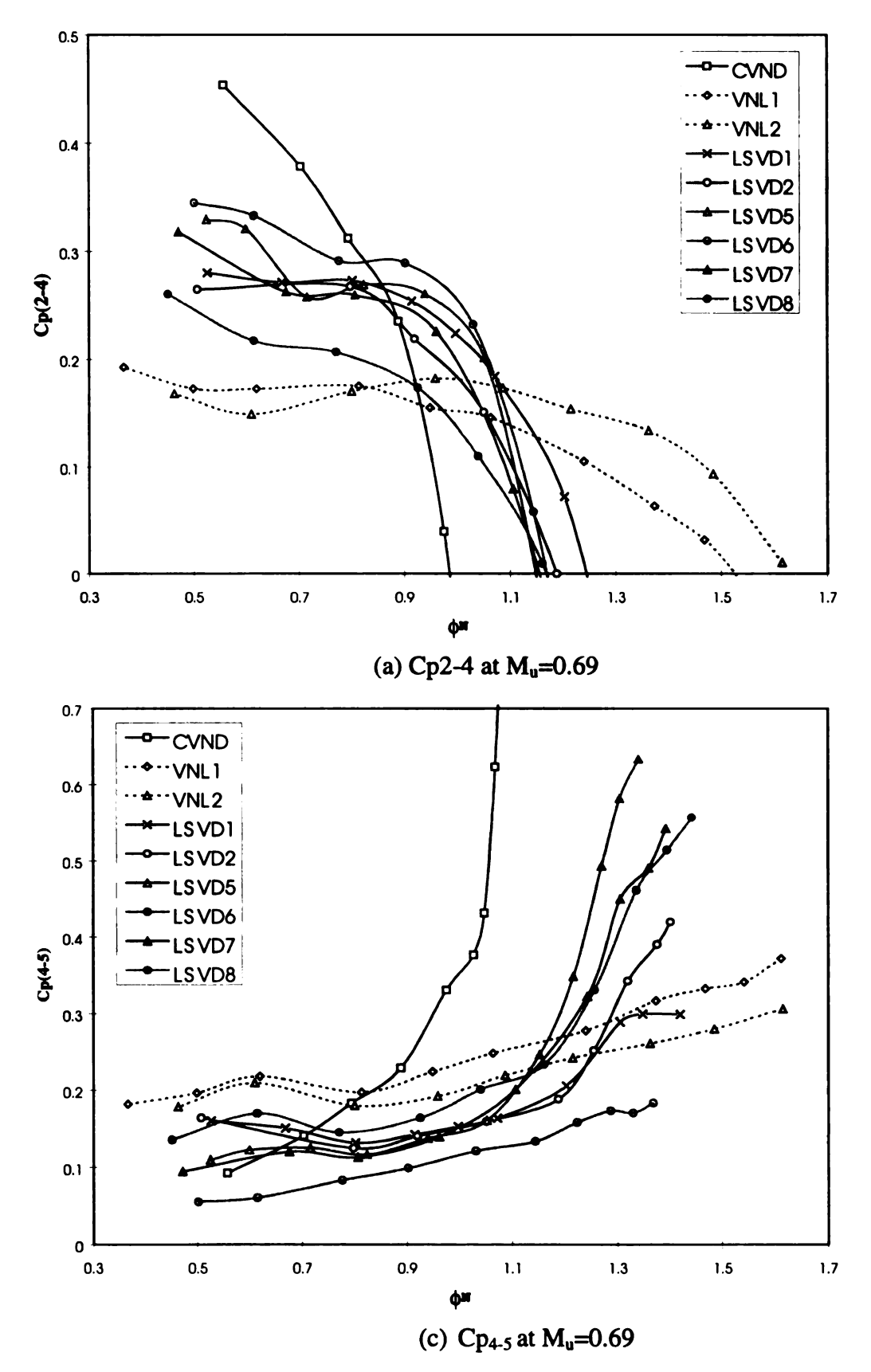


Figure 4.13 Subdivided pressure recovery in the diffusers at  $M_u$ =0.69

# 5. EXPERIMENTAL RESULTS ON INSTABILITY IN A CENTRIFUGAL COMPRESSOR STAGE

The causes of the instability in the centrifugal compressor stage with the different diffusers were determined with the aid of four dynamic pressure probes installed in the inducer (probe A), the impeller (probe B and C), and the diffuser (probe D) based on phase angle correlation. The results for  $M_u=1.02$  are shown here because of the similar patterns with the impeller tip speed. Both transducer B and transducer C were located in the impeller at the same radius but different circumferential position.

Since most rotating stall signals reported in the literature were below the rotational speed of the impeller, the data between 0-500 Hz are plotted here.

# 5.1. Instabilities of the Centrifugal Compressor Stage

### 5.1.1. Unsteady Behavior of the Stage with the Vaneless Diffusers

Figure 5.1(a) to (c) illustrate the power spectra of the signal from the inducer, the impeller, and the diffuser respectively of the compressor with the VNL2 at  $M_u = 1.02$ . The rotational frequency of 460 Hz is clearly seen along with a weak peak at 360 Hz. This weak peak was common to all configurations and constant in its level and occurred at  $M_u = 1.02$  only. Thus, it is presumed that 360 Hz peak is an electrical noise.

From Figure 5.1(a), no significant pressure fluctuations are found in the inducer at high mass flow rates. However the pressure fluctuations grow at Op#10 for VNL2. These fluctuations indicate the onset of inducer stall. This corresponds to the abrupt temperature increases at the inducer in Figure 5.8. The fluctuations are non-periodic.

From Figure 5.1(b) it can be seen that the energy level of the signals from the impeller is generally higher than in the inducer since transducer B is located in the impeller. The pressure fluctuations have medium level of energy over the whole frequency range at the first four operating points of the VNL2 configuration. The high energy in the fluctuations is due to the inducer choke and the associated losses. The level of energy decreases between Op#5 and Op#9 indicating that the flow in the impeller is stable yielding the best performance. At Op#10 the fluctuations begin to increase and at Op#12, two peaks, one at 488 Hz and the other at 6 Hz are clearly seen. There is weak periodic instability at 294 Hz. This could be possible impeller stall. The peak at 6 Hz corresponds to the stage surge and the peak at 488 Hz was found to be due to a rotating stall in the impeller. As the peak at 488 Hz can not be seen at inducer inlet and is stronger in its energy level than one in the diffuser, this instability seems to be attributed to a destabilization of the impeller flow. Detailed analysis will be given later in this chapter.

From the power spectra of transducer D for VNL2 in Figure 5.1(c), it can be seen that the pressure fluctuations have very low energy for the first nine operating points. Thus, the diffuser operates very stable in the operating range and has no negative effects on the stage stability. Between the Op#10 and Op#12 the fluctuations increase over the whole frequency range. A strong peak at 6 Hz is found in all transducers of VNL2 configuration. The energy at this peak is between 32 and 46 dB, which is much higher

than at any other peaks. Since the peaks occurred at the same frequency in all transducer signals, it can be classified as surge peak. The peak at 6 Hz has the highest energy level at transducer D than at any other transducer. This is expected as stage surge where 488 Hz rotating impeller stall was aggravated by diffuser rotating stall. The flow angle out of impeller is 11.5 degrees and this corresponds to the critical flow angle suggested by Van den Braembusche (1980).

Figure 5.2(a) to (c) are the power spectra of the signal from the inducer, the impeller, and the diffuser respectively of the compressor with the VNL1 at  $M_u = 1.02$ . The energy levels of the impeller at the last point (Op#13) are slightly lower than those of VNL2 at the last point (Op#11). The relative velocity leaving the impeller tip with VNL1 is bigger than with VNL2 at the same flow rate because the VNL1 has smaller inlet flow area. So this flow rate is the critical flow rate causing the impeller passage stall due to the excessive diffusion ratio ( $W_2/W_1$ ).

## 5.1.2. Unsteady Behavior of the Stage with the Vaned Diffuser

Figure 5.3 (a) to (c) are the power spectra of the signal from the inducer, the impeller, and the diffuser respectively of the compressor with the vaned diffuser at  $M_u = 1.02$ . The rotational frequency of 460 Hz is clearly seen along with a weak peak at 360 Hz. The rotational frequency of 460 Hz is seen in all configurations with higher energy than in the inducer.

As shown in Figure 5.3(a), the inducer seems to be stable because of the diffuser throat choke limiting the throughflow, hence avoiding critical incidence at inducer leading edge. It is presumed that the stage surge was caused due to the diffuser stall at a

higher flow rate than the flow rate causing critical incidence at the inducer. It is clear in Figure 5.8 that there is no sudden temperature rise with CVND configuration.

Only small fluctuations are seen in the power spectra of transducer B for the CVND (Figure 5.3(b)) configuration, except at the last operating point. Thus, the impeller is not the critical component causing the instability for this configuration and the 8 Hz peak seen at the last operating point is mild surge and its fluctuation level is lower than those of both diffuser and inducer are. Detailed analysis revealed that two-cell rotating stall running opposite to the impeller at 80Hz at flow rate just below Op#10. Its relative speed to the impeller is 0.17 and it has weak fluctuation level with no harmonics.

In the case of CVND configuration in Figure 5.3(c), from Op#1 to Op#4 flow fluctuation can be detected in the low frequency range (0~100Hz), as the diffuser is choked. The pressure fluctuations increase between Op#5 and Op#8. The pressure side stall causes these increased fluctuations. However, Op#9 and Op#10 seem to have much less fluctuations than at Op#8. The stage attained highest head ( $\psi_N$ ) at these operating points. The surge peak at Op#11 can be seen with 8 Hz frequency.

The peak in CVND configuration is weaker in energy than in LSVDs or VNLs configurations indicating the stage with CVND might have been operated just up to the onset of the surge.

## 5.1.3. Unsteady Behavior of the Stage with the Low Solidity Vaned Diffusers

Figure 5.4 through Figure 5.7 are the power spectra of the signal from the inducer, the impeller, and the diffuser, respectively of the compressor with low solidity vaned diffusers at  $M_u = 1.02$ .

From the figures of power spectra at inducer with LSVDs (Figure 5.4(a) through Figure 5.7(a)), no significant pressure fluctuations are found in the inducer at high mass flow rates. However, the pressure fluctuations grow at the last operating points except for LSVD6. These fluctuations indicate the onset of inducer stall. The fluctuations are non-periodic. For LSVD6, there was no inducer stall because flow fluctuations at 294 Hz, which appear in all the configurations of both LSVDs and VNLs, were abnormally developed into the surge and limited the throughflow.

From the figures of power spectra at impeller with LSVDs (Figure 5.4(b) through Figure 5.7(b)), the energy level over the whole frequency range is slightly higher at first three operating points and then decreases between Op#4 and Op#6. The higher energy at the first three operating points is due to the inducer choke. However, between Op#7 and Op#10 the fluctuations at lower frequencies increase to be very high at Op#10 and Op#11. Such patterns were not seen either in VNLs or CVND configurations. Thus, this high energy fluctuation at low frequency is possibly due to the vanes of the LSVD. At last operating points, flow fluctuations at 294 Hz can be detected both upstream and downstream of impeller and its energy level is higher in the impeller than in the inducer or in the diffuser. These fluctuations seem to be attributed to a destabilization of the impeller. For LSVD5 configuration, this 294 Hz fluctuation in the impeller is higher than any other configuration leading to surge.

From the figures of power spectra at diffuser with LSVDs (Figure 5.4(c) through Figure 5.7(c)), very high fluctuations are seen in the first two operating points due to the pressure side stall of the diffuser vanes. The fluctuations between Op#4 and Op#10 are

small indicating that the diffuser does not cause any instability in this operating range. However at operating point 11 fluctuations increase and the surge peaks are seen at 8 Hz.

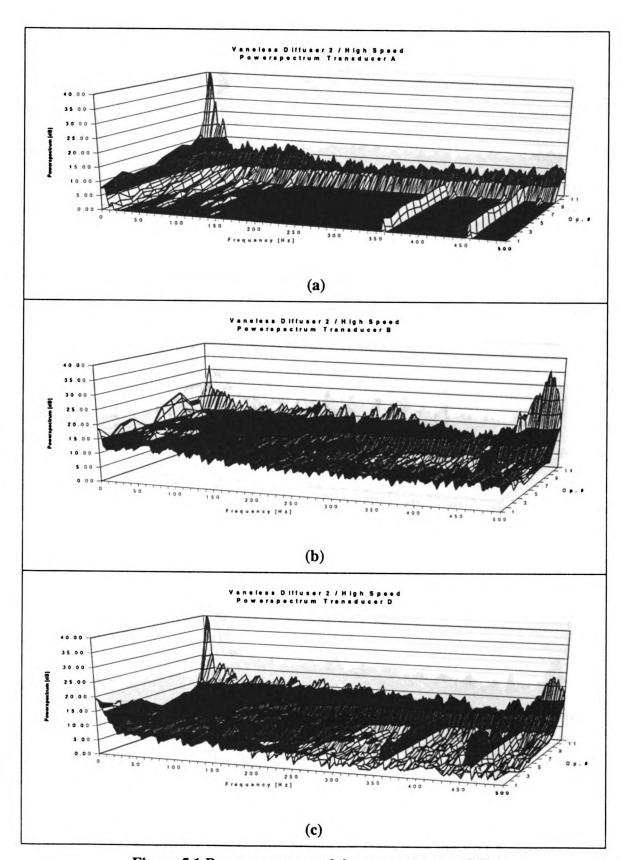


Figure 5.1 Power spectrum of the stage with the VNL2

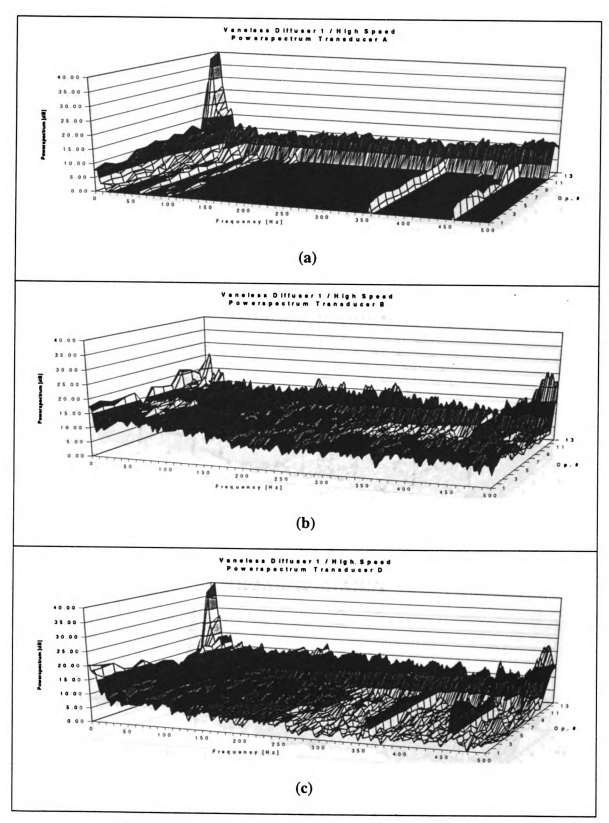


Figure 5.2 Power spectrum of the stage with the VNL1

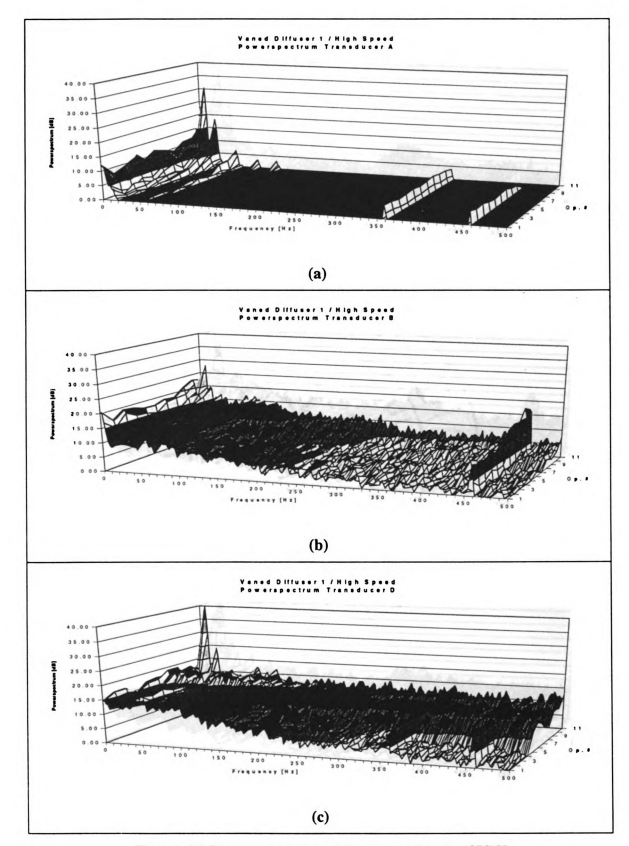


Figure 5.3 Power spectrum of the stage with the CVND

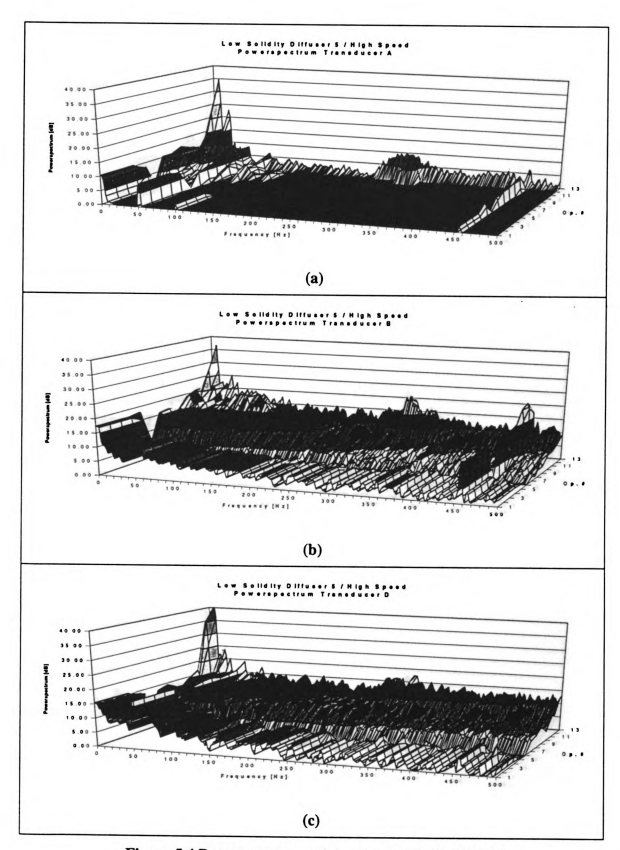


Figure 5.4 Power spectrum of the stage with the LSVD5

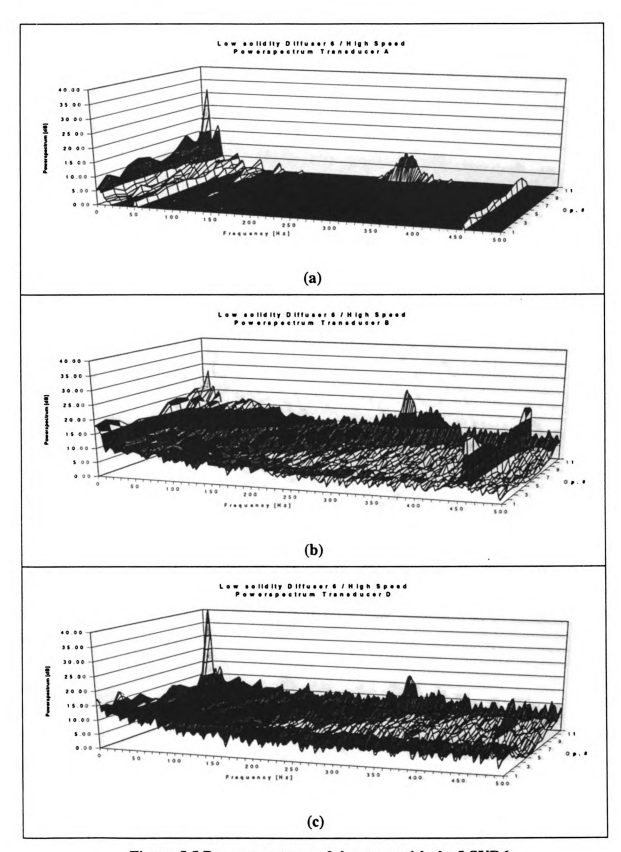


Figure 5.5 Power spectrum of the stage with the LSVD6

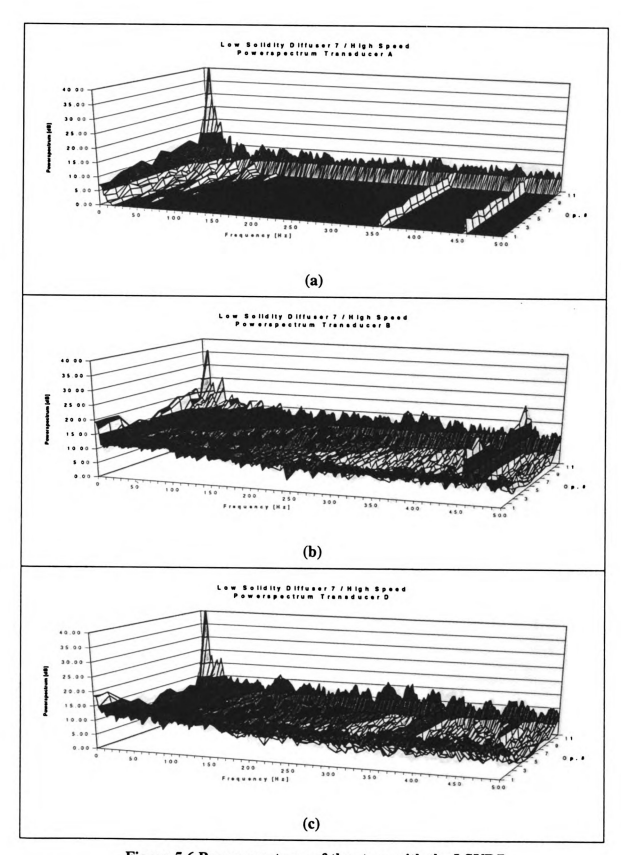


Figure 5.6 Power spectrum of the stage with the LSVD7

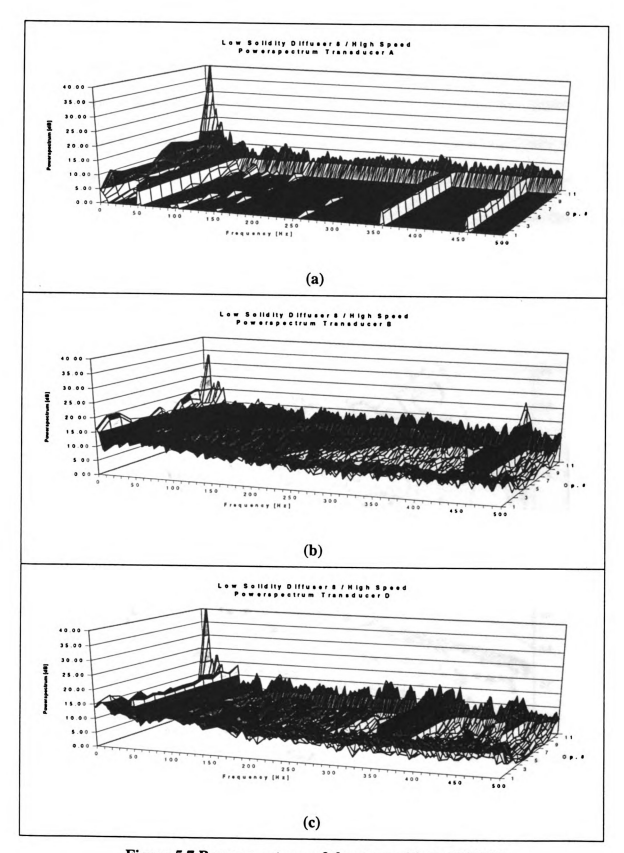


Figure 5.7 Power spectrum of the stage with the LSVD8

# 5.2. Inducer Stall

Figure 5.8 represents the dimensionless temperature at all speeds and total pressure ratio at  $M_u$ =1.02. This figure shows that at a certain mass flow the temperature in the inducer rises suddenly. The noise during the operation increases according to the inducer temperature rise. This is caused by highly energized fluid that flows back from the impeller to the inducer. This backflow at the shroud causes the main flow to accelerate. From Figure 5.8 the diffuser has no influence on the mass flow at which the inducer stalls.

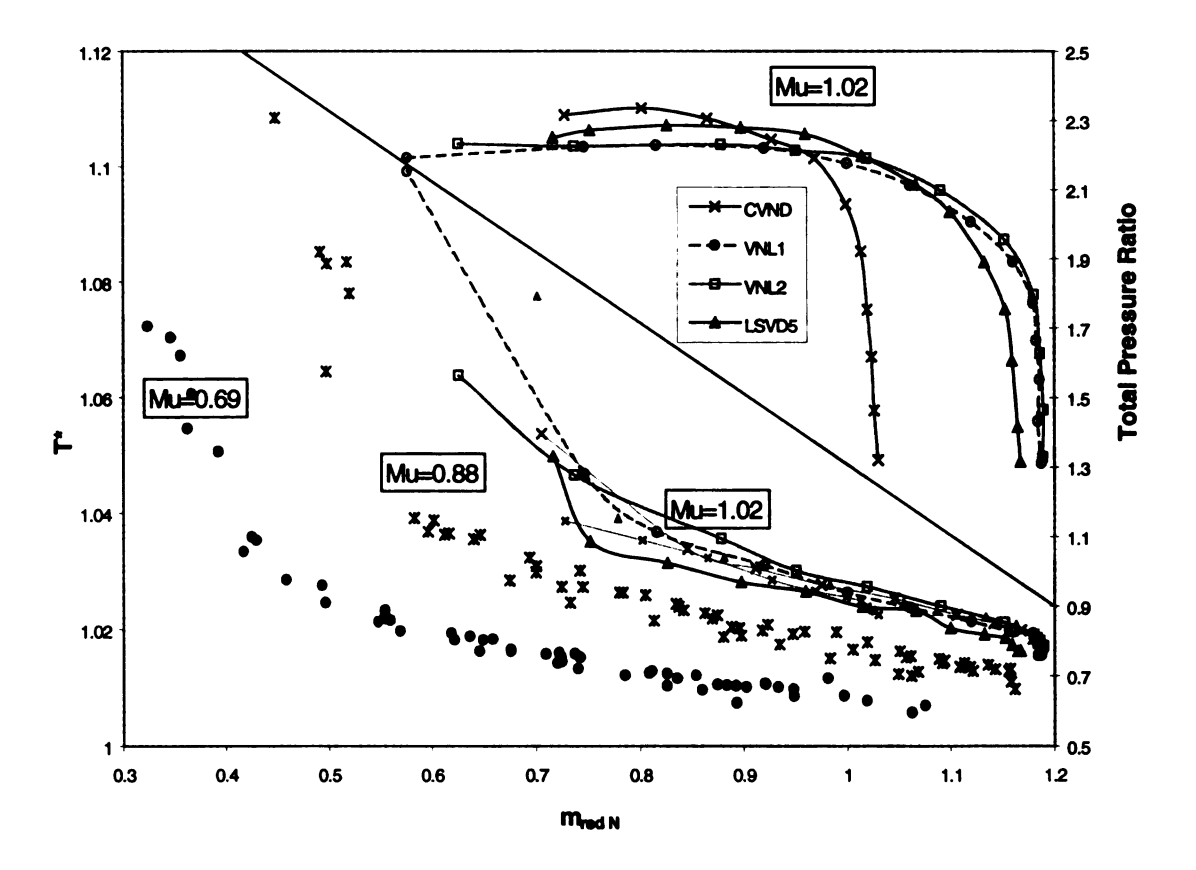


Figure 5.8 Temperatures in the diffuser

## 5.3. Rotating Stall

A rotating stall was found only with the vaneless diffuser configurations. It is presumed the progressive impeller stall due to the destabilization of the impeller flow. It was found that four or five rotating cells running opposite to the impeller appears and its relative speed is constant irrespective of impeller speed. Flow fluctuation at 488 Hz is stronger in the impeller than in the diffuser and the inducer for VNL1 at M<sub>u</sub>=1.02. This fluctuation of 488 Hz in the impeller is even stronger than that of 6 Hz which is the surge frequency. This fluctuation was added to the destabilization of the vaneless diffuser and triggered the stage surge with high fluctuation.

Another fluctuation occurred at 294 Hz with VNLs and LSVDs in the impeller but those fluctuations were not clear.

Table 5-1 Summary of the impeller rotating stall

	$M_{\rm u}$	0.69	0.88	1.02	1.17
VNL1	m	-5	-4	-4	-5
	ω./	0.23	0.275	0.24	0.2
	$m\Omega$	366Hz	440Hz	488Hz	564Hz
VNL2	m	-5/-2	-4/+3	+4	-5
	ω./	0.296/0.555	0.266/0.5	0.26	0.208
	$m\Omega$	464/348	422/602Hz	490Hz	554Hz

## 5.4. Surge

Deep surges of VNLs were triggered by the diffuser stall which added already existing rotating impeller stall. Flow fluctuation at  $M_u$ =1.02 is stronger in the diffuser than in any components. This surge might be triggered by a destabilization of the diffuser. This means that the diffuser is the critical component.

Deep surge was never reached in vaned diffuser because there was only single component stall. Flow fluctuation at  $M_u$ =1.02 is much stronger in the diffuser than in any components. This surge might be triggered by a destabilization of the diffuser also. Table 5-2 summarized the surge characteristics.

**Table 5-2 Summary of surge** 

$M_u=1.02$	f <sub>SURGE</sub> (Hz)	INDUCER	IMP_B	IMP_C	DIFFUSER
VNL2	6	46	32		46
CVND	8	30	28	25	41
LSVD3	6	34	35		44
LSVD5	8	35	37	30	46
LSVD6	8	31	28	25	41
LSVD7	8	42	35	34	46
LSVD8	6	42	34	34	44

$M_u = 0.88$	$f_{SURGE}(Hz)$	INDUCER	IMP_B	IMP_C	DIFFUSER
VNL2	4	35	21	25	34
CVND	6	15		18	23
LSVD5	8	36	33	31	40
LSVD6	8	35	30	28	36
LSVD7	6	36	30	28	37
LSVD8	6	37	29	32	13

$M_u = 0.69$	f <sub>SURGE</sub> (Hz)	INDUCER	IMP_B	IMP_C	DIFFUSER
VNL2	6	46	44	45	47
CVND					
LSVD5	6	22	20	18	22
LSVD6	6	24	24	22	30
LSVD7	6	25	25	22	30
LSVD8	6	27	27	30	30

# 6. NUMERICAL CALCULATION OF LOW SOLIDITY VANED DIFFUSERS

It is essential for a fluid engineer to understand a detailed flow behavior of the diffuser in order to develop and predict the performance of turbomachinery. The flow field in the low solidity vaned diffuser was numerically simulated to understand the flow behavior in the diffuser and thus to define the design parameters affecting the performance using 3-D viscous Navier-Stokes code. The LSVD5 and the LSVD8 were modeled for numerical simulation at the design flow, near surge flow, and near choke flow and compared with the experimental results. The effect of solidity or the turning angle on the diffuser flow was studied.

This chapter explains 3-D viscous Navier-Stokes code, grid generation, and boundary conditions used for numerical simulation and its results.

#### 6.1. 3-D Viscous Flow Solver

The code employed for this work is TASCflow, which solves the 3-D Reynolds Stress averaged Navier-Stokes (N-S) equations and the time averaged mass and energy equations in stationary or rotating frames of reference. The viscous effects are simulated by the standard k-\varepsilon turbulence model and log-law wall functions for a hydraulically smooth surface. The primitive variables are found directly with the methods such as the

streamfunction-vorticity approach, which, by differentiation of the basic N-S equations, eliminates the pressure term and reduces the number of equations to be solved.

In partial differential equation form, the governing equations for a general scalar, momentum and mass are

$$\frac{\partial}{\partial t}(\rho\phi) + \frac{\partial}{\partial x_{j}}(\rho u_{j}\phi) = \frac{\partial}{\partial x_{j}}\left(k_{eff}\left(\frac{\partial\phi}{\partial x_{j}}\right)\right) + S_{\phi}$$
 (5-1)

$$\frac{\partial}{\partial t}(\rho u_i) + \frac{\partial}{\partial x_j}(\rho u_j u_i) = -\frac{\partial P}{\partial x_j} + \frac{\partial}{\partial x_j}\left(\mu_{eff}\left(\frac{\partial u_i}{\partial x_j}\frac{\partial u_j}{\partial x_i}\right)\right) + S_{u_i}$$
 (5-2)

$$\frac{\partial \rho}{\partial t} + \frac{\ddot{o}}{\partial x_j} (\rho u_j) = 0 \tag{5-3}$$

and

$$\rho = \frac{P}{RT} \tag{5-4}$$

where

$$\mu_{eff} = \mu_{dynamic} + \mu_{turbulent}$$

$$k_{\it eff} = k_{\it dynamic} + k_{\it turbulent}$$

The partial differential equations are discretized by means of an implicit formulation at each node, so that each algebraic equation contains unknown values from its neighboring nodes. The second order accurate discretization scheme uses skewed-upwind differencing combined with physical advection correction. This fully implicit formulation avoids stability limits that occur with explicit methods. A finite volume

approach is used, which insures conservation of mass, momentum, and energy over any region of the computational domain.

Amineni (1996) used BTOB3D code for his numerical analysis of the low solidity vaned diffusers. He chose BTOB3D code encouraged by many researchers' reports showing the capability of predicting the flow inside the turbomachinery components. Dalbert et al. (1995) carried out two sets of flow field calculation using both BTOB3D and TASCflow, which are commercially available 3-D Navier-Stokes codes, and showed those current computational fluid dynamics (CFD) codes can achieve reasonable level of accuracy when used with about 100,000 nodes. He concluded that the turbulence model of TASCflow is superior if detailed flow is important.

# 6.2. Grid Generation and Boundary Conditions

A single blade passage was modeled with body-fitted, H-grid structured mesh. The blade is located in the center of the domain and nodes are buried in the width of the blade to improve resolution of the leading and trailing edges, and to reduce grid skewness in these regions. The computational mesh, shown in Figure 5-1, consists of 105 x 50 x 17 gridlines in the streamwise (I), pitchwise (J) and spanwise (K) direction resulting in 89,250 nodes.

The adjacent regions of the full diffuser were modeled by periodic boundary condition. At the inlet, total pressure, total temperature, and velocity direction were specified. In every case, the inlet endwall boundary layer thickness was assumed to be zero, and a uniform flow condition across both the span and pitch was assumed.

The inlet boundary condition can be taken from (1) the measurement data of the impeller exit, (2) CFD results of impeller simulation, or (3) one-dimensional flow analysis. A simulation using measurement data at an impeller exit is ideal and highly relevant for code validation. But it is known that the traverse data obtained near the surge and stall flows are unstable and not reliable. And this measurement is not possible unless a test rig has the appropriate measuring equipment including space for it. Casey et al (1995) carried out numerical calculations of the vaned diffuser of a pump using three different inlet boundary conditions and compared those calculation results with each other. He found out that more complicated inlet boundary conditions do not yield significantly better results than simple (uniform) inlet boundary condition. Thus, using uniform inlet condition seemed appropriate for this work.

The inlet total pressure, total temperature, and velocity direction were determined based on velocity triangles and checked against measured temperature rise.

At the outlet, the mass flow rate was specified. The walls were modeled as an adiabatic smooth wall and the logarithmic law of the wall was used as a wall boundary condition. The wall function was used to prescribe the shear stress on solid surfaces.

The flow was assumed steady, compressible, and turbulent. The working fluid was dry air governed by the equation of perfect gas. The turbulence model used was a standard k- $\epsilon$  model.

The total pressure ratio curves of the stage with the VNL1, the CVND, the LSVD5, and the LSVD8 and the three selected flows used for the numerical calculation on the constant speed line of  $M_u$ =0.69 are shown Figure 6.2. The ratios of mass flow rates of the near surge and the near choke to the design flow are 0.73 and 1.41 respectively. In

Figure 6.3 the measured pressures divided by the stage inlet total pressures at different locations of the stage with LSVD5 are shown.

The calculation was carried out on a Sun Ultra1 Workstation until the maximum residual was less than 10<sup>4</sup>. The whole diffuser geometry is shown in Figure 6.4.

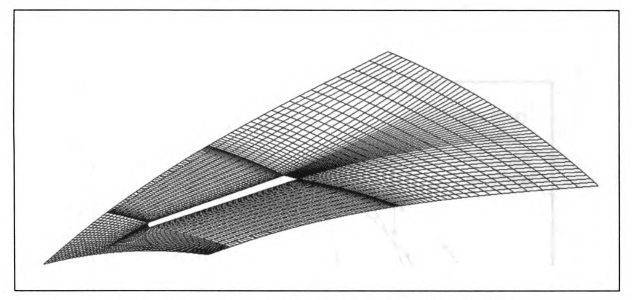


Figure 6.1 Computational mesh of LSVD5 (105 x 50 x 17)

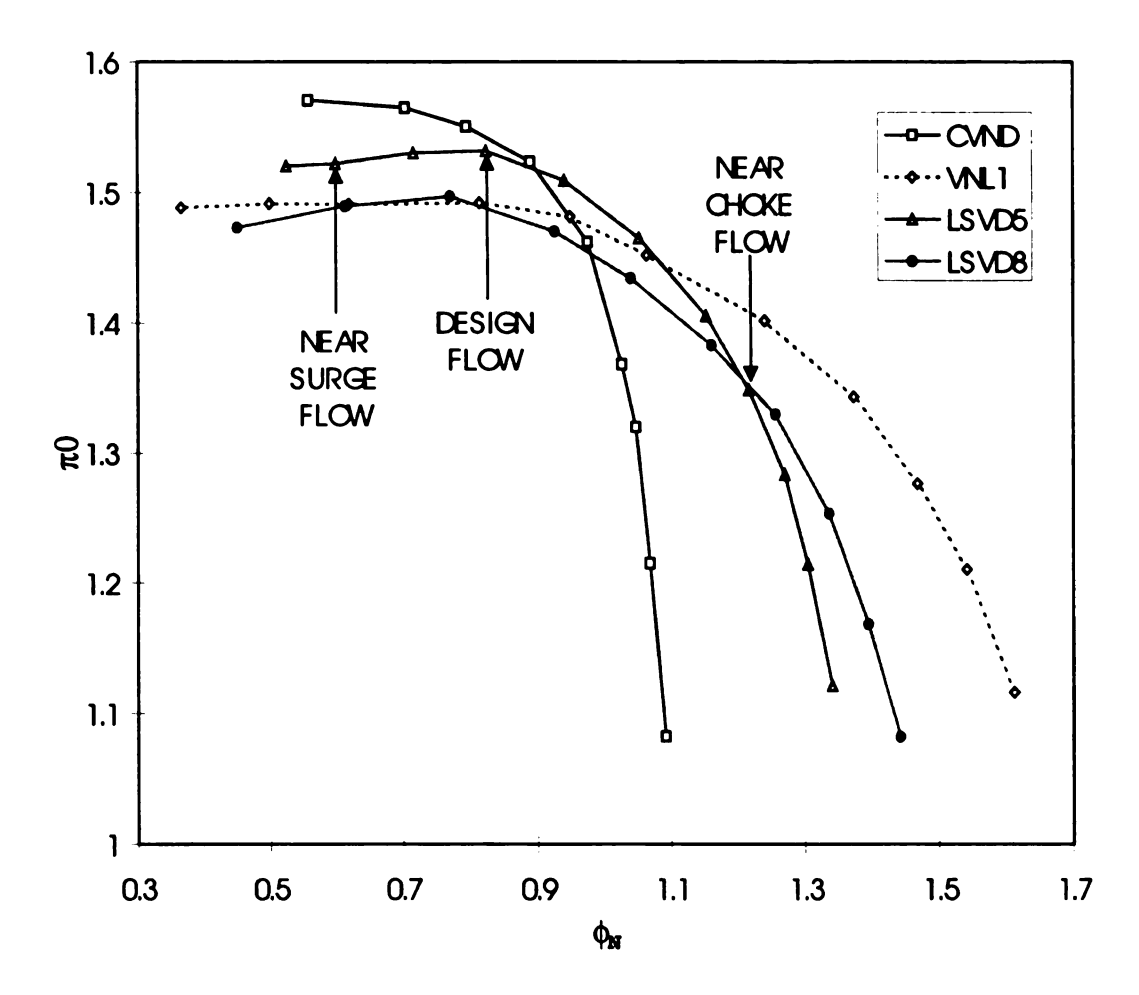


Figure 6.2 Pressure ratio curves of the stage with the flows used for the numerical calculation

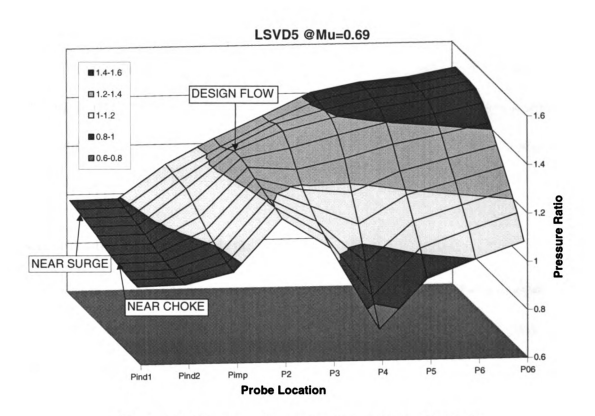


Figure 6.3 Pressure rise in the stage with the LSVD5

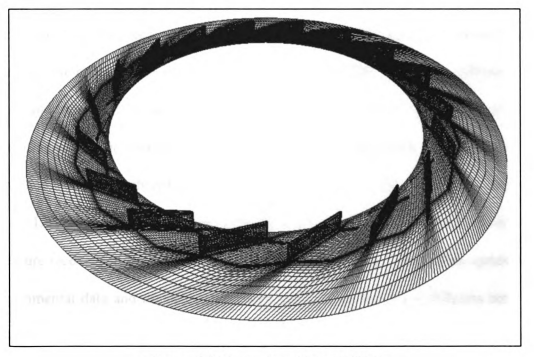


Figure 6.4 Geometry of the LSVD5

### **6.3.** Calculation Results

This section will discuss the result from the numerical calculation of the LSVD5 and the LSVD8 at the design flow, near surge, and near choke flow. From this result, the low solidity vaned diffuser was modified for better performance and will be discussed in the next section.

#### **6.3.1. Pressure Distributions in the Diffusers**

Figure 6.5 through Figure 6.7 show the calculated static pressure distributions of the LSVD5 and the LSVD8 for the flows of design, near surge, and near choke respectively and at  $M_u$ =0.69.

From Figure 6.5(a), the pressure rises steeply and the contour lines are aligned for the design flow between the adjacent vanes of LSVD5 with an incidence angle of -1.9°. Most of the pressure recovery is achieved up to the trailing edge of the diffuser vane. The pressure rise becomes less steep in the area from the trailing edge of the diffuser vane and more and more uniform circumferentially as the diffuser radius increases. In tests of this operating speed, the peak efficiency of the LSVD5 is even higher than that of the CVND designed with the cambered airfoil type vane. Compared to the LSVD5, the pressure rise of the LSVD8 is similar but due to a less flow guidance on turning from shorter vane the pressure recovery of the LSVD8 is lower as shown in Figure 6.5(b). This agrees with the experimental data and the calculated efficiency differences of the diffusers between the LSVD5 and LSVD8 are 1.5% and 4.2% based on total-to-total and total-to-static calculation respectively.

Figure 6.6(a) and Figure 6.6(b) represent the calculated static pressure distributions of the LSVD5 and the LSVD8 respectively at near surge flow and M<sub>u</sub>=0.69. The incidence angle of these is +5.0°. It is apparent for the LSVD5 as shown in Figure 6.6(a) that the pressure gradient of the diffuser vane suction side is steep up to half of the diffuser length and then the flow is separated from the suction side of the rest half of the diffuser vane. This is due to excessive blade loading from the thin flat plate vane, which is sensitive to the incidence angle. Compared to the LSVD5, the flow of the LSVD8 has less separated region with the same incidence angle and the pressure distribution at downstream of the vane trailing edge is more uniform circumferentially at a radius as shown in Figure 6.6(b). The chord length difference, which is directly related to the solidity and the turning angle with this configuration, makes a big difference in the flow field and pressure recovery at off-design flow condition. The calculated efficiency differences of the diffusers between the LSVD5 and LSVD8 are -2.3% and -1.3% based on total-to-total and total-to-static calculation respectively.

Figure 6.7(a) and Figure 6.7(b) represent the calculated static pressure distributions of the LSVD5 and the LSVD8 respectively at near choke flow and M<sub>u</sub>=0.69. The incidence angle of these is -9.7°. There is a hole at the leading edge of the vane suction side indicating the stagnation point. The pressure drops steeply along the vane suction side (lower surface) but starts to gain near trailing edge. However, the flow moving along the vane pressure side (upper surface) starting from the stagnation point accelerates while turning around the leading edge causing sudden pressure drop. From then the diffusion starts. There is additional pressure rise after the trailing edge and this agrees with the experimental data. The calculated efficiency differences of the diffusers

between LSVD5 and LSVD8 are -0.7% and -4.0% based on total-to-total and total-to-static calculation respectively. This difference at off-design comes from the chord length.

### **6.3.2.** Flow Field in the Diffusers

Figure 6.8 through Figure 6.10 represent the flow pattern including velocity vectors and streaklines from the diffuser inlet of LSVD5 and LSVD8 for the flows of design, near surge, and near choke respectively and at M<sub>u</sub>=0.69. Each section represents near the wall (2% from the wall), 25% from the wall, and the mid-span of the low solidity vaned diffuser from left to right, respectively. The solid lines are the streaklines from the diffuser inlet and the arrows for the velocity vectors at corresponding grids.

In Figure 6.8(a) the fluid of the LSVD5 with incidence angle of -1.9° tends to flow more tangentially as we look at the flow close to the wall. Due to the viscous effect the boundary layer is developing and thus, retarding the radial component velocity. The main flow is well guided within the vane but the flow after the trailing edge turns tangentially. This seems to be attributed to the shape of trailing edge as well as the viscous effect. Compared to LSVD5, the flow in LSVD8 is guided by shorter blade resulting higher friction loss due to longer flow path. This agrees with the experimental data and the calculated differences of the diffuser efficiencies are 1.5% and 4.2% based on total-to-static and static-to-static calculation, respectively.

In Figure 6.9(a), the LSVD5 stalls at the near wall of the suction side and large recirculation area is shown near the trailing edge of suction side. However, the main flow of mid-span seems to be well guided yet. The secondary flow can be found at this flow. Figure 6.9(b) shows the flow pattern of LSVD8 at near surge flow. When compared to

LSVD5 (longer vane) with the same boundary conditions, the flow of LSVD8 seems much healthier than that of LSVD5. This is because LSVD5 is much more loaded than LSVD8. Therefore, the surge of LSVD5 is expected to happen earlier if the cause of the surge is due to the diffuser stall.

Figure 6.10(a) shows the flow of the LSVD5 with the incidence angle -9.7°. The flow near the leading edge is complex. The flow after the stagnation point accelerates and especially for the flow turning around the leading edge along the pressure side. The stalled area of the vane pressure side and furthermore the backflow from the trailing edge to leading edge can be seen. The flow stalled in the pressure side of the diffuser vane from the leading edge due to high negative incidence forming a virtual throat. The virtual throat limited the flow rate and made the different overload capacity from that of the vaneless diffuser (see Figure 3). The flow of LSVD8 is similar to the LSVD5.

### 6.3.3. Separation at the Diffuser Vane

Figure 6.11 through Figure 6.13 show the streaklines starting from the leading edge of the LSVD5 and the LSVD8 for the flows of design, near surge, and near choke respectively and at  $M_u$ =0.69. Here the near wall (2% from the wall), 25% from the wall, and the mid-span of the low solidity vaned diffuser are represented by the gray density.

Figure 6.11(a) and (b) show the streaklines starting from the leading edge of LSVD5 and LSVD8 at the design flow. It is shown that the flow is nicely guided by the vane and the flow of LSVD5 is more guided passing shorter path than LSVD8.

Figure 6.12(a) and (b) streaklines starting from the leading edge of LSVD5 and LSVD8 at the near surge flow. The flow of the LSVD5 near the wall is separated and

recirculating at the vane suction side. However, the flow of the LSVD8 is much healthier than the LSVD5 achieving better performance with the same incidence angle.

Figure 6.13(a) and (b) streaklines starting from the leading edge of the LSVD5 and the LSVD8 at the near choke flow. The stalled area along the pressure side (upper surface of the vane) is shown.

## 6.3.4. Vane Setting Angle Effect

In an attempt to understand the effect of the vane setting angle on the diffuser performance, two degrees of vane setting angle was added and subtracted from the LSVD5. The rest of parameters remain the same. The same boundary conditions were employed. Figure 6.14 through Figure 6.17 show the calculated results of these LSVDs where the pressure contours, the flow pattern, and the streaklines from the leading edge are combined in one figure in the counterclockwise direction.

First, in an attempt to develop the overload capacity the vane setting angle was increased by two degrees (called LSVD5<sup>+2</sup>). Figure 6.14 represents the calculation with near choke conditions at M<sub>u</sub>=0.69. Compared to the LSVD5 the flow near leading edge is much healthier and yields much better diffuser efficiencies as shown in Figure 6.18 and Figure 6.19. The definitions of diffuser efficiency are explained in Appendix B. However, as shown from Figure 6.15, the flow with near surge conditions became much worse. The whole area of the vane suction side stalls and the diffuser efficiencies are dropping about 5% by setting the vane angle two degrees radially for the same flow conditions of near surge. It seems the flow rate corresponding to the peak efficiency moves at a higher flow rate.

Secondly, in an attempt to increase surge margin capacity the vane setting angle was reduced by two degrees (called LSVD5<sup>-2</sup>). Figure 6.17 represents the calculation with near surge flow conditions at M<sub>u</sub>=0.69. Compared to LSVD5 the flow at the vane suction side stalls only near end wall area offering better diffuser efficiencies about 5%. The pressure recovery between the vane channel is steeper than the LSVD5. It is apparent that the trailing edge/suction side has less separated flow zone than the LSVD5. Here at this flow condition, two-degree vane setting angle corresponds to 5% difference of the diffuser efficiencies. However, the peak efficiency seems to be lower than LSVD5. As presumed before, it seems that the optimum incidence angle for the maximum efficiency is near -2 degrees. The pressure recovery of LSVD5<sup>-2</sup> at near choke flow is very poor. Due to high negative incidence angle the separated flow at the vane pressure side generates a thick flow blockage (Figure 6.16). The flow accelerates from the vane leading edge. The first diffuser efficiency is the lowest among all the calculated diffuser including LSVD8, which offers 2 to 4 % higher than LSVD5. Furthermore, the second efficiency of LSVD5<sup>-2</sup> is really poor close to zero.

The LSVD8 has the lowest peak efficiency at the design flow due to the small turning angle. This implies the sensitivity of the turning angle (or the solidity) to the maximum diffuser efficiency. However, as the flow more away than the design flow the efficiencies of LSVD8 become higher than LSVD5. This implies the sensitivity of the flow incidence (vane setting angle) to the diffuser performance including operating range.

The diffuser efficiencies are shown in Figure 6.18 and Figure 6.19 based on total-to-static and static-to-static respectively. The effect of vane setting angle on the pressure recovery and flow range agrees well with Sorokes et al. (1992).

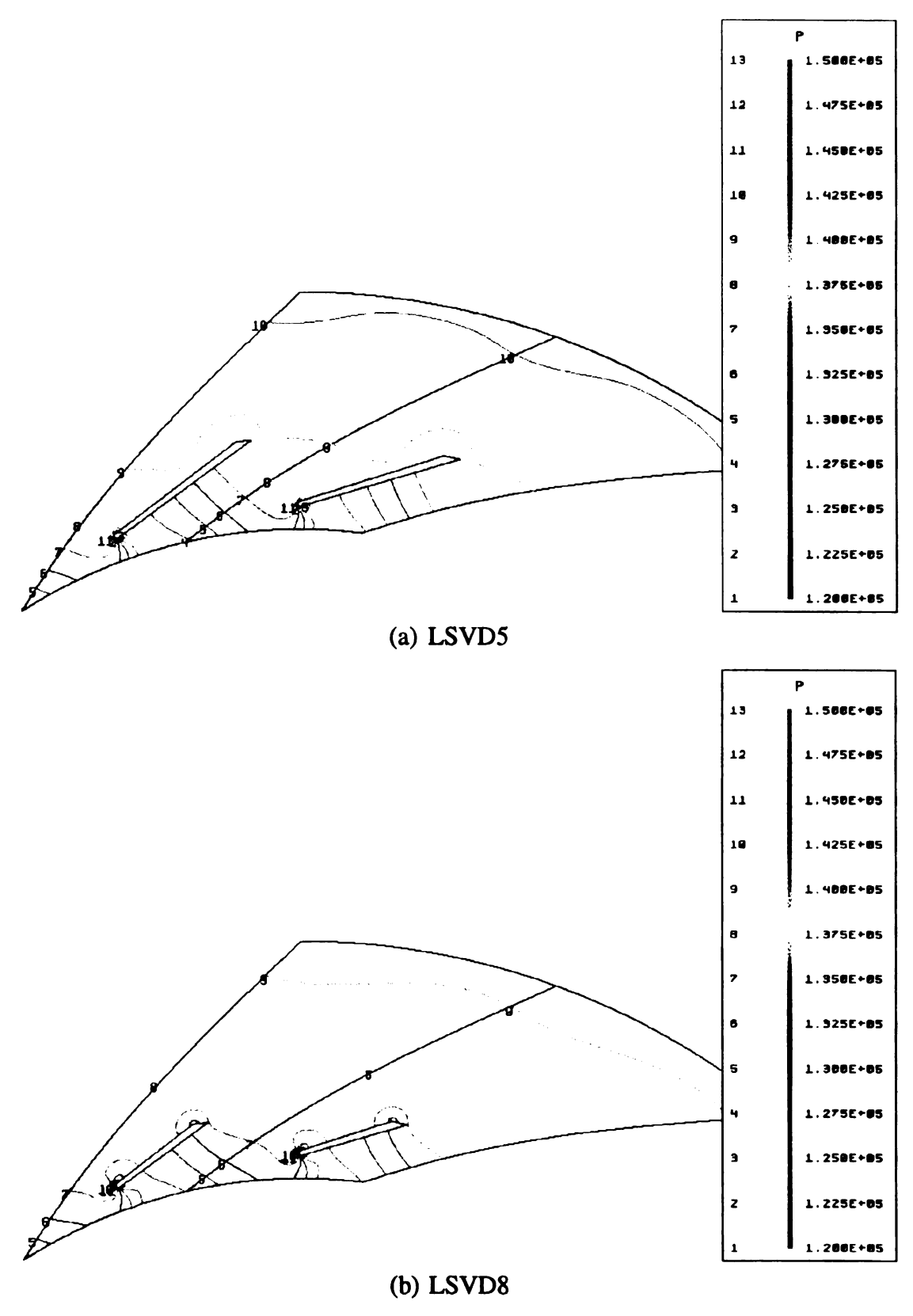


Figure 6.5 Pressure distribution at design flow & M<sub>u</sub>=0.69

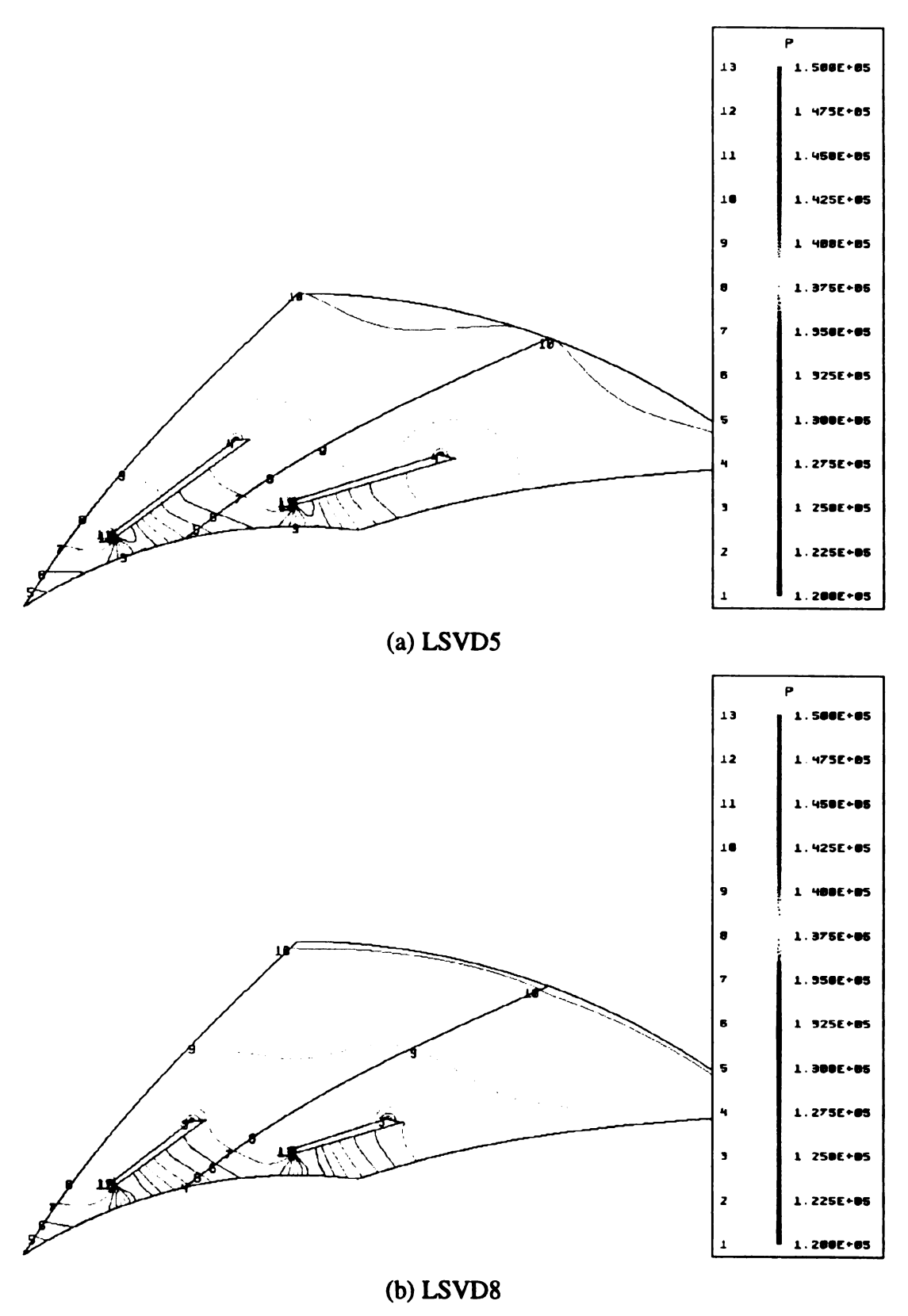


Figure 6.6 Pressure distribution at near surge flow & M<sub>u</sub>=0.69

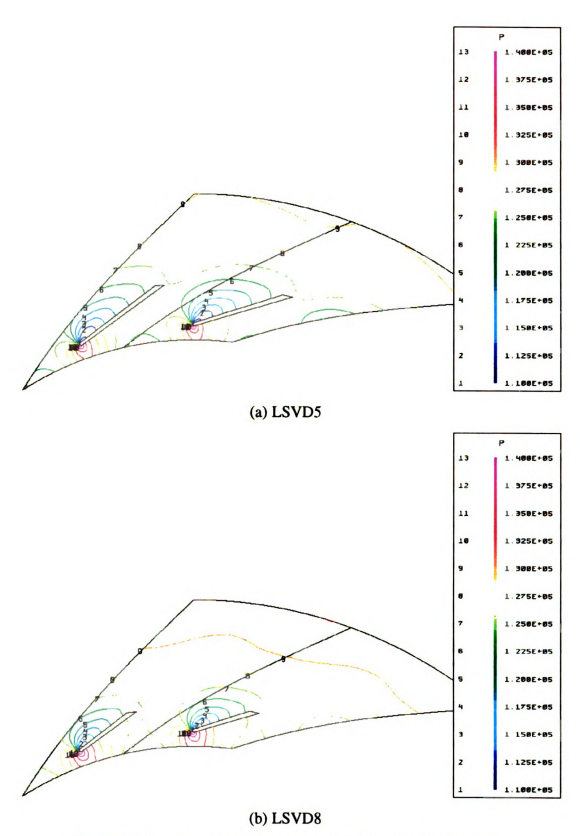


Figure 6.7 Pressure distribution at near choke flow & Mu=0.69

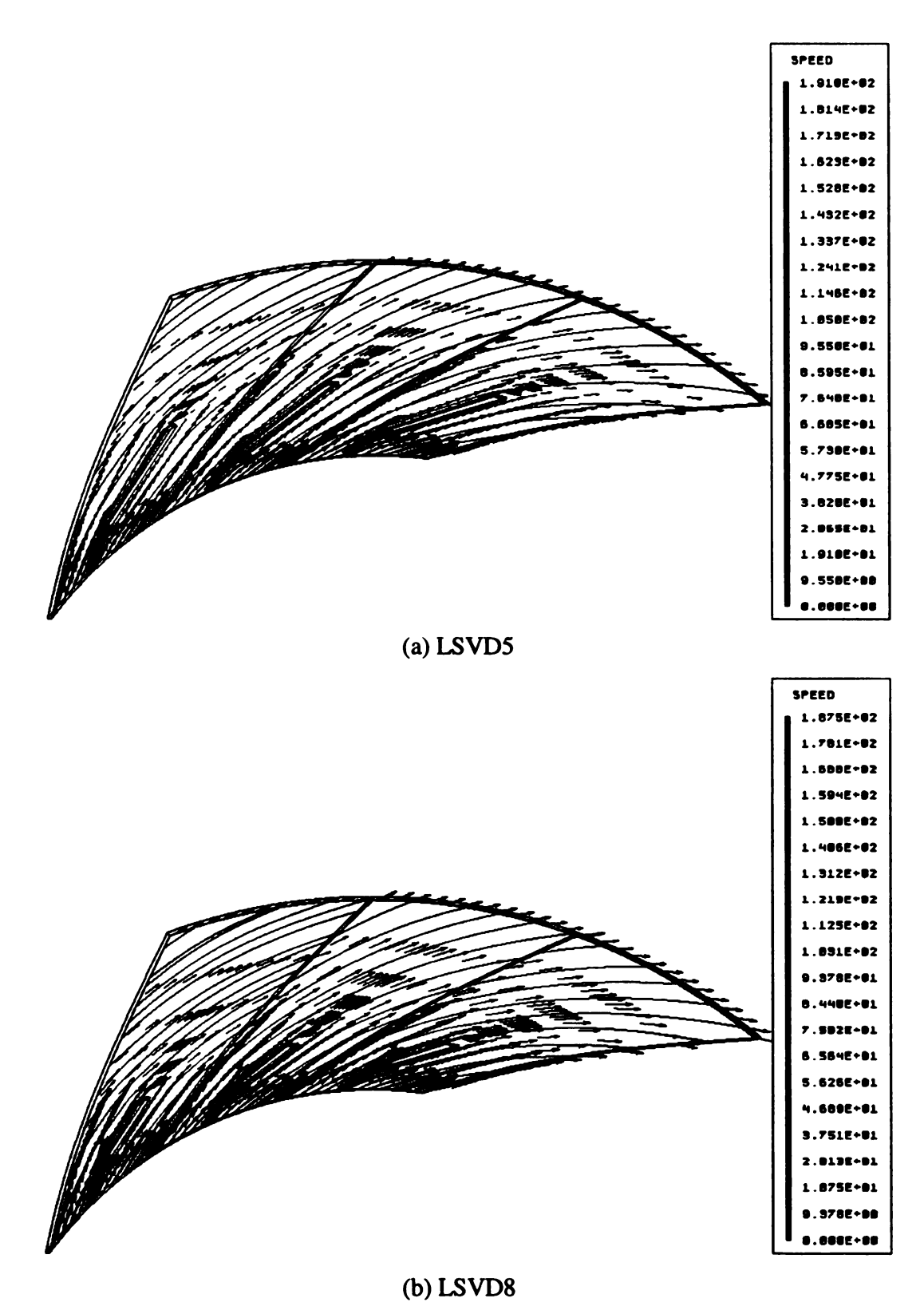


Figure 6.8 Flow pattern at design flow &  $M_u$ =0.69

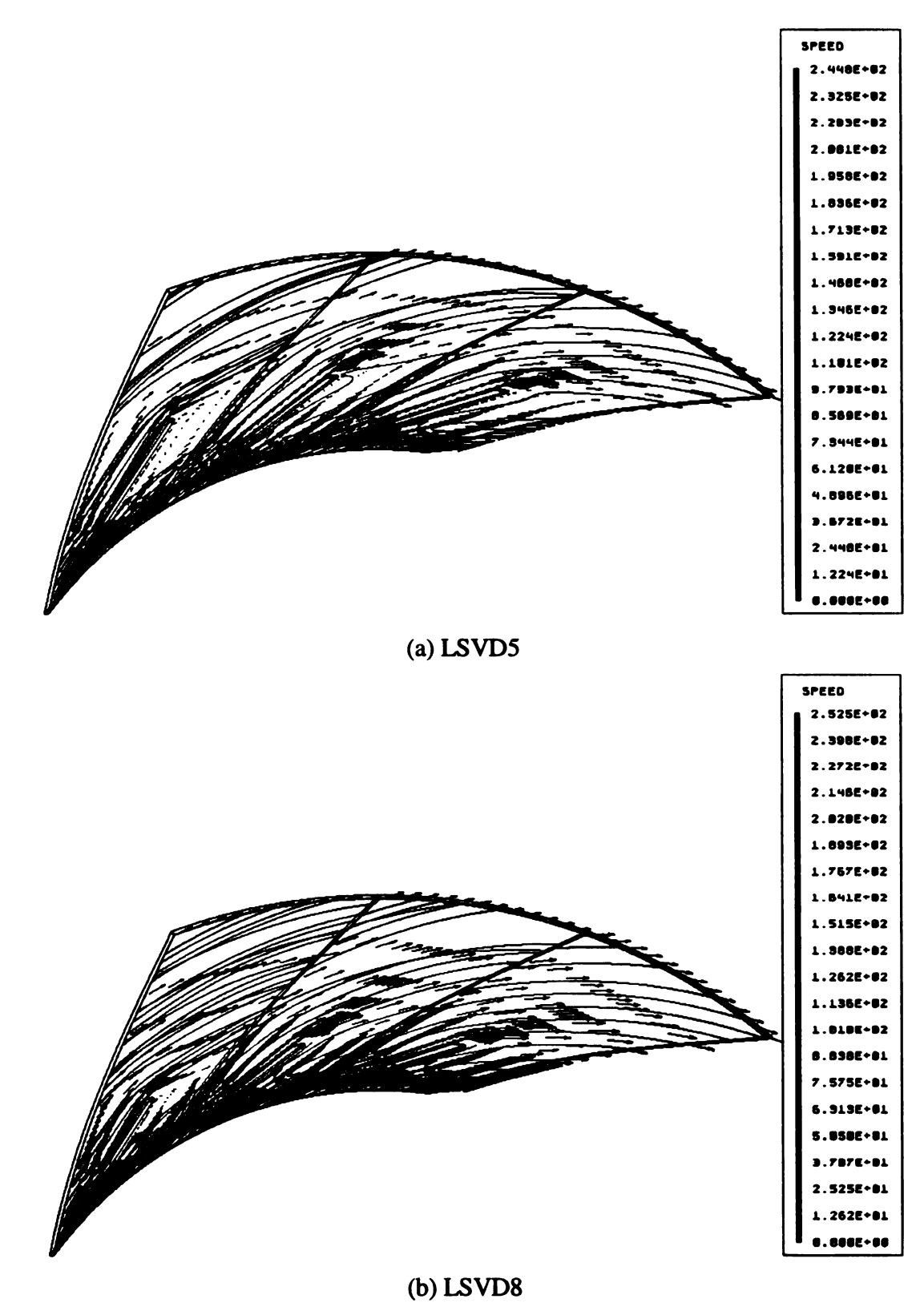


Figure 6.9 Flow pattern at near surge flow &  $M_u$ =0.69

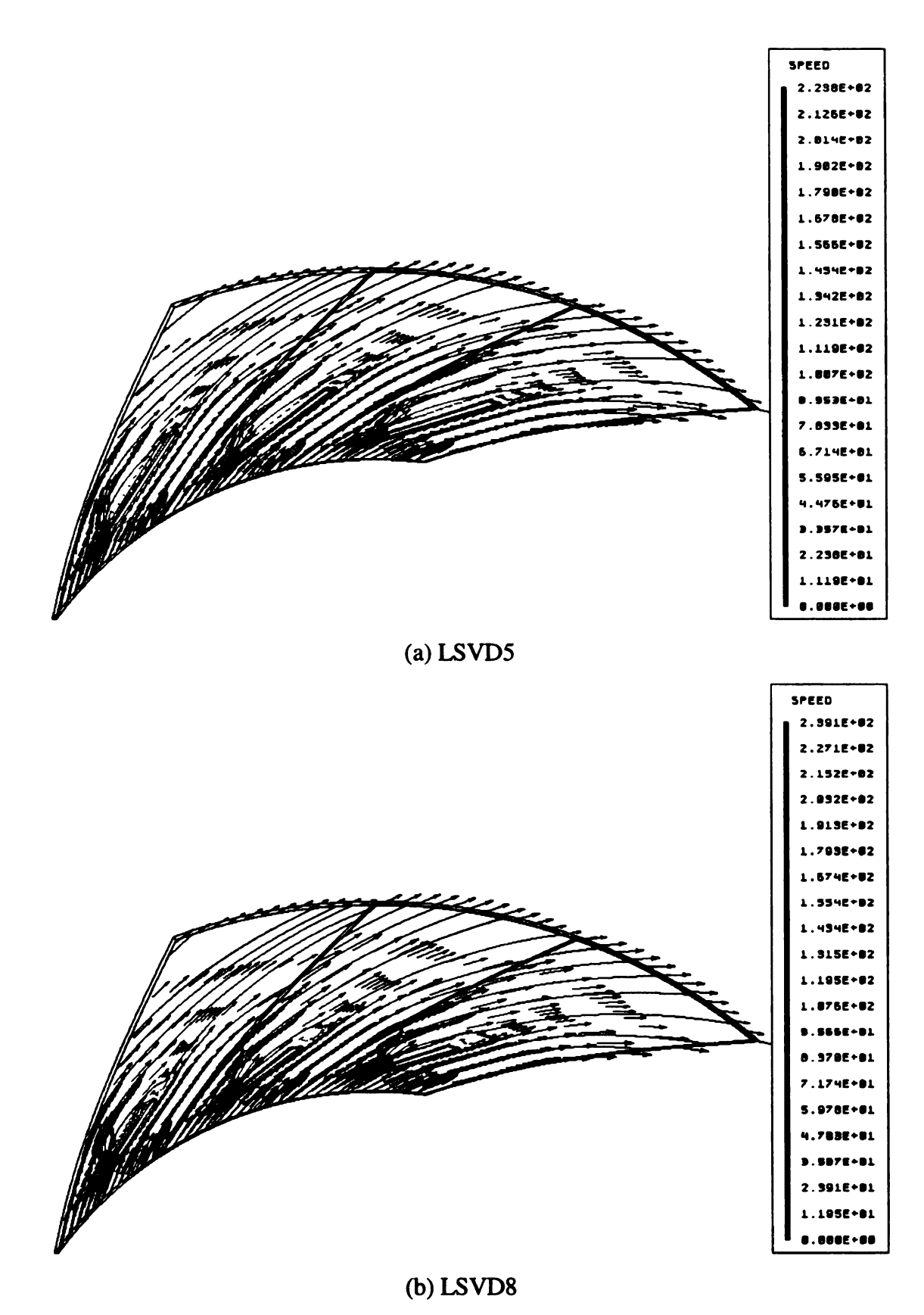
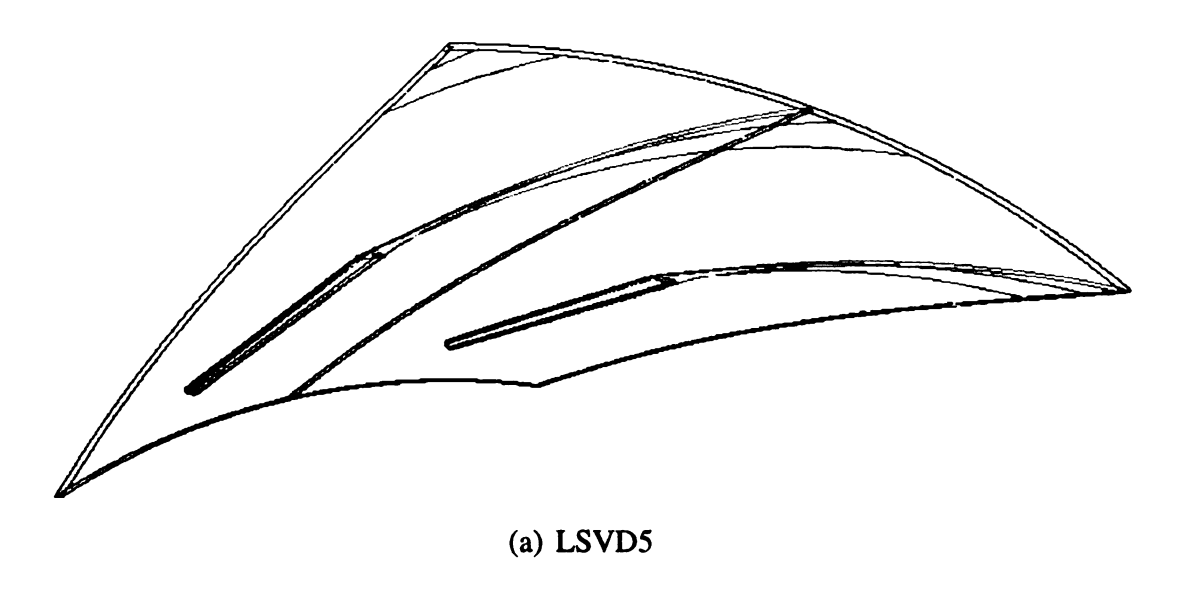


Figure 6.10 Flow pattern at near choke flow &  $M_u$ =0.69



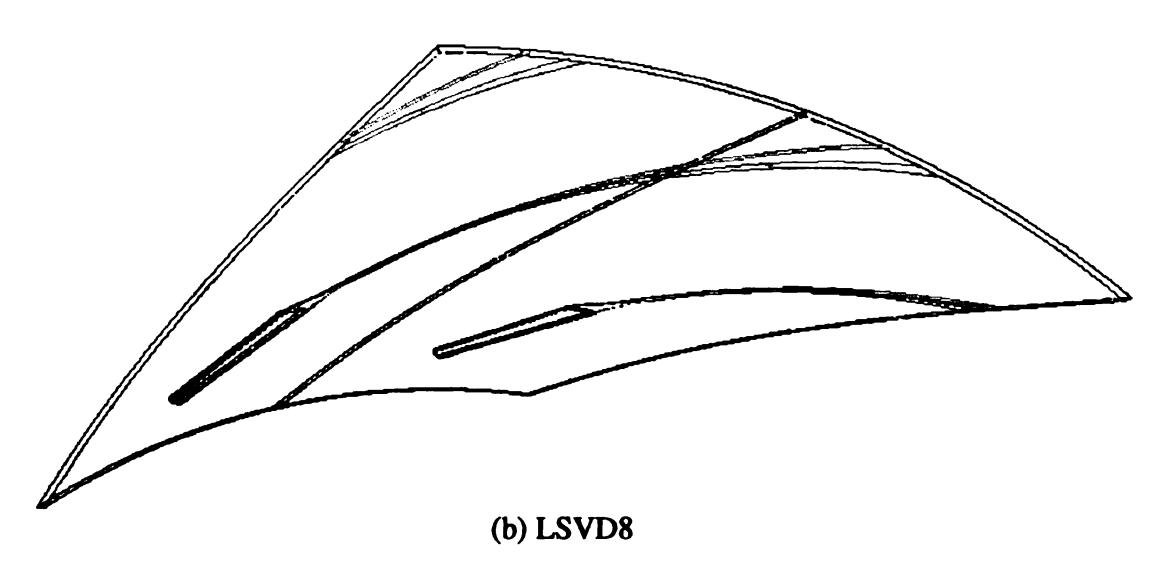
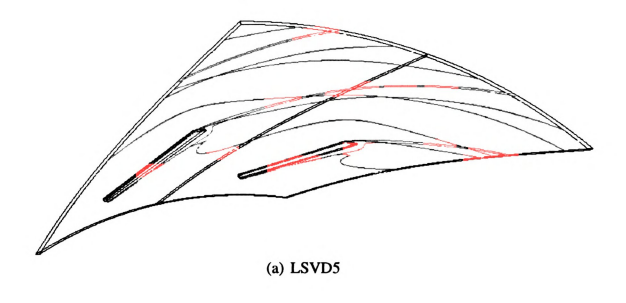


Figure 6.11 Flow from leading edge pattern at design flow &  $M_u$ =0.69



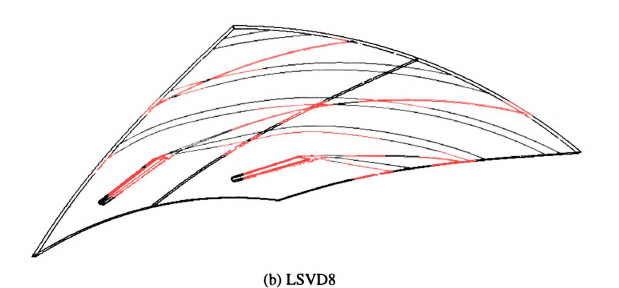
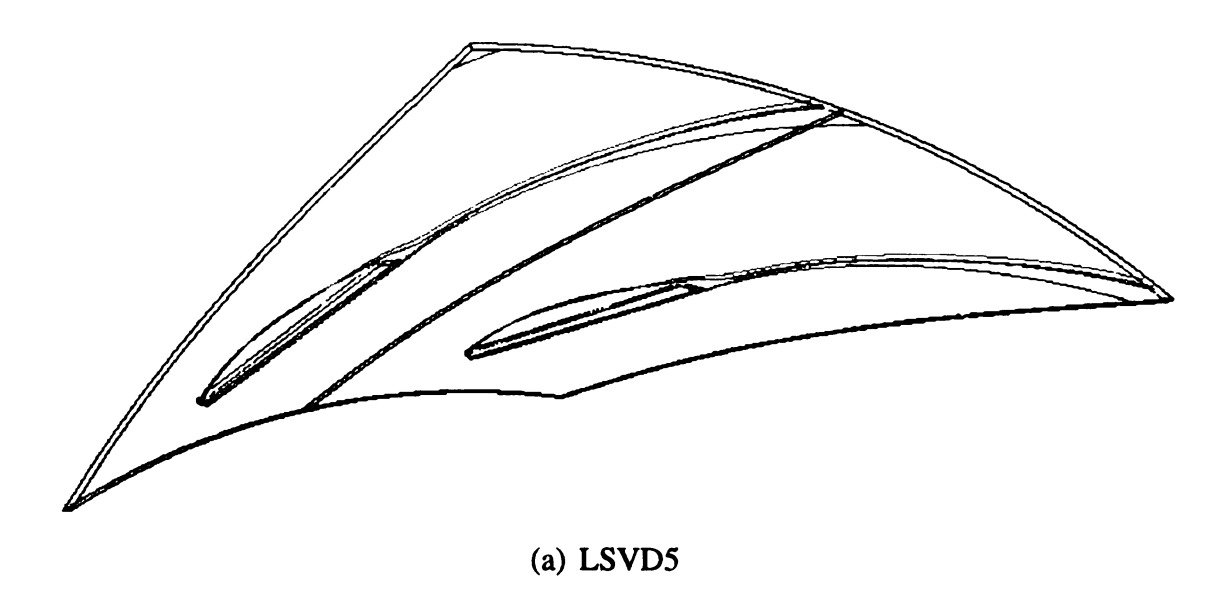


Figure 6.12 Flow from leading edge at near surge flow &  $M_u\!\!=\!\!0.69$ 



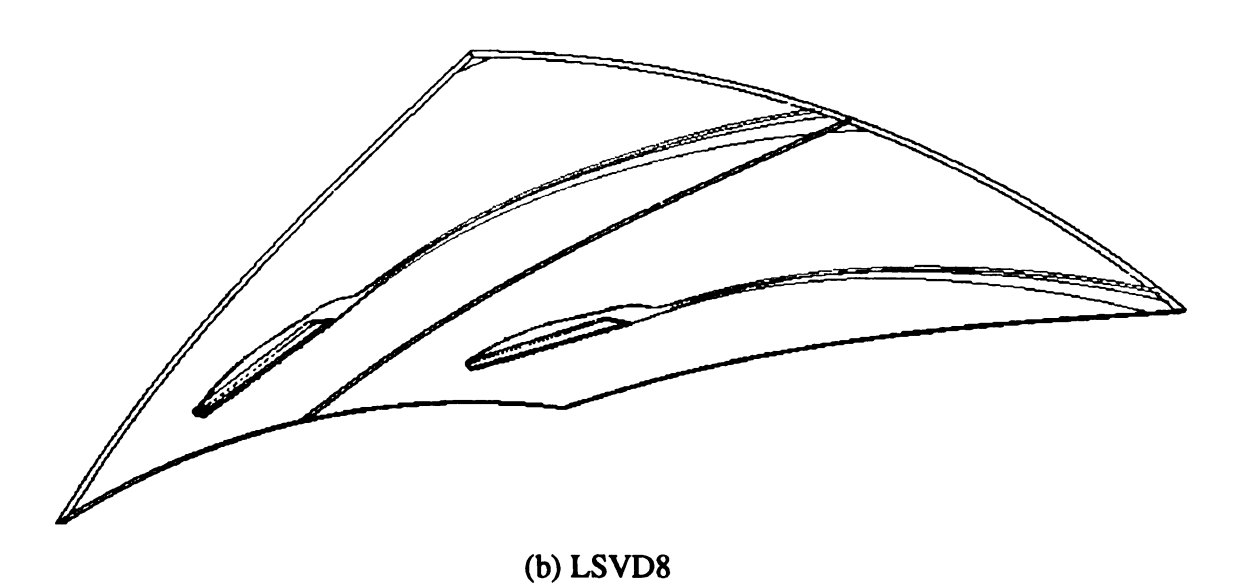


Figure 6.13 Flow from leading edge at near choke flow &  $M_u$ =0.69

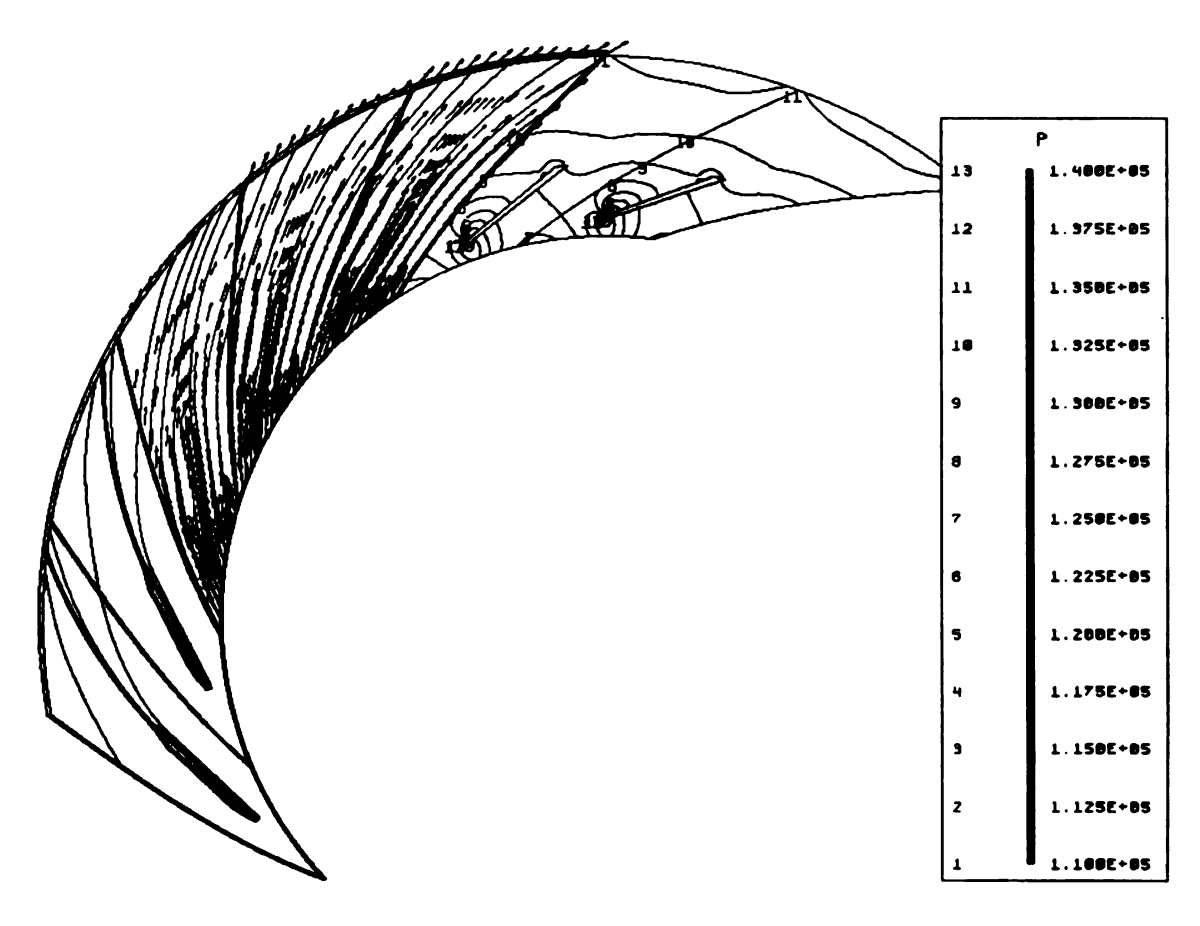


Figure 6.14 LSVD5<sup>+2</sup> for near choke flow at  $M_u$ =0.69

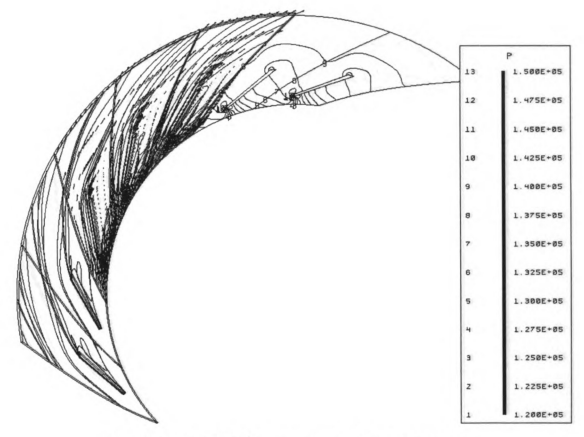


Figure 6.15 LSVD5<sup>+2</sup> for near surge flow at M<sub>u</sub>=0.69

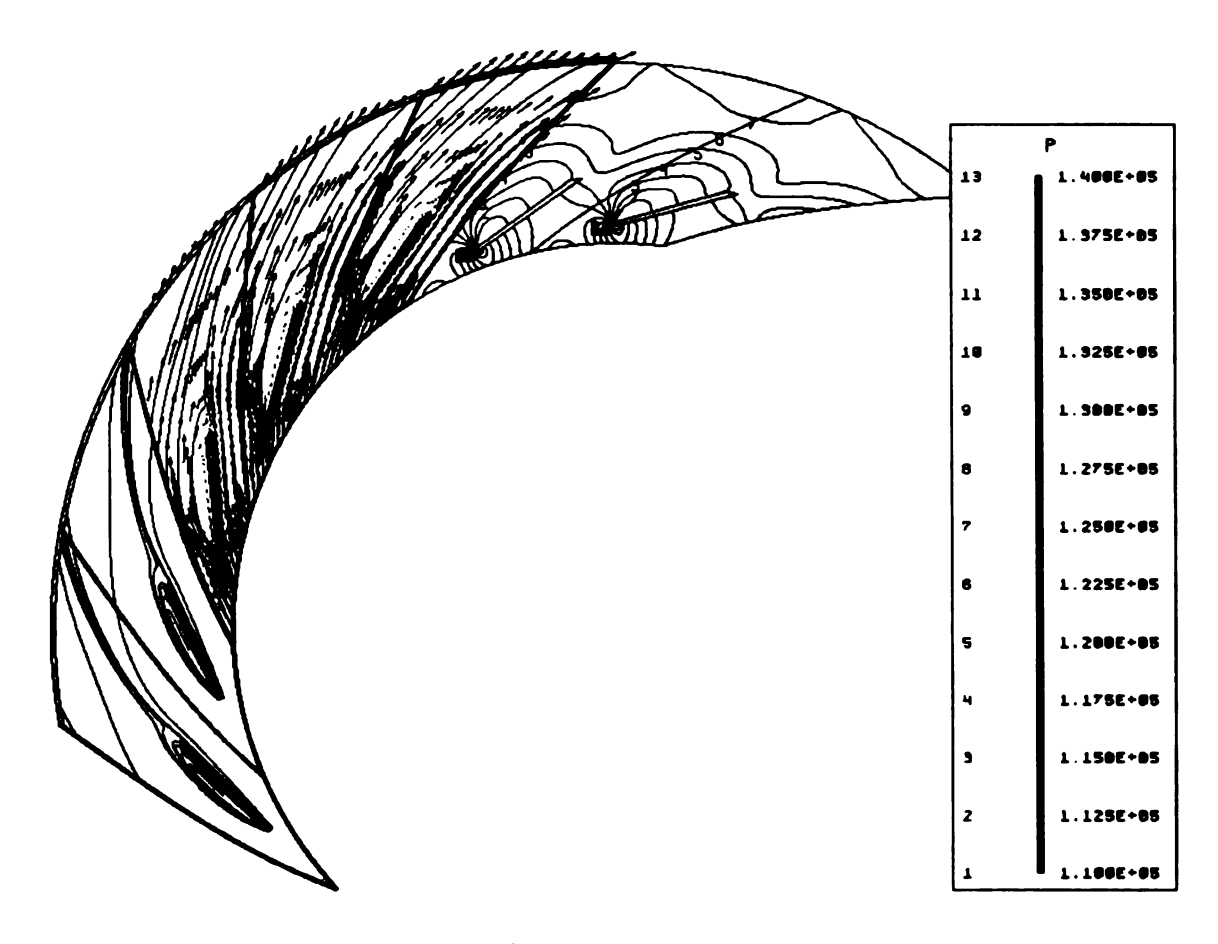


Figure 6.16 LSVD5<sup>-2</sup> for near choke flow at  $M_u$ =0.69

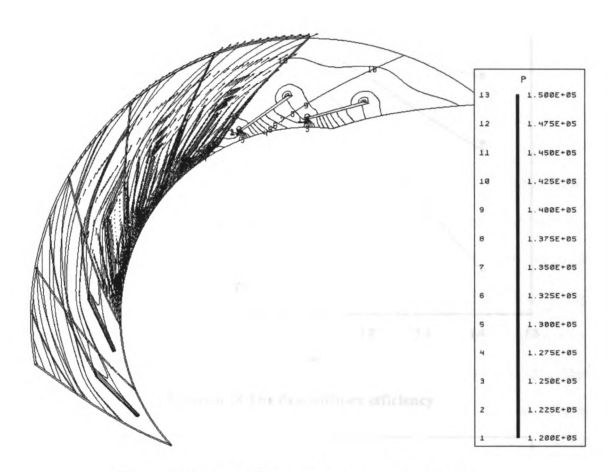


Figure 6.17 LSVD5 $^{-2}$  for near surge flow at  $M_u$ =0.69

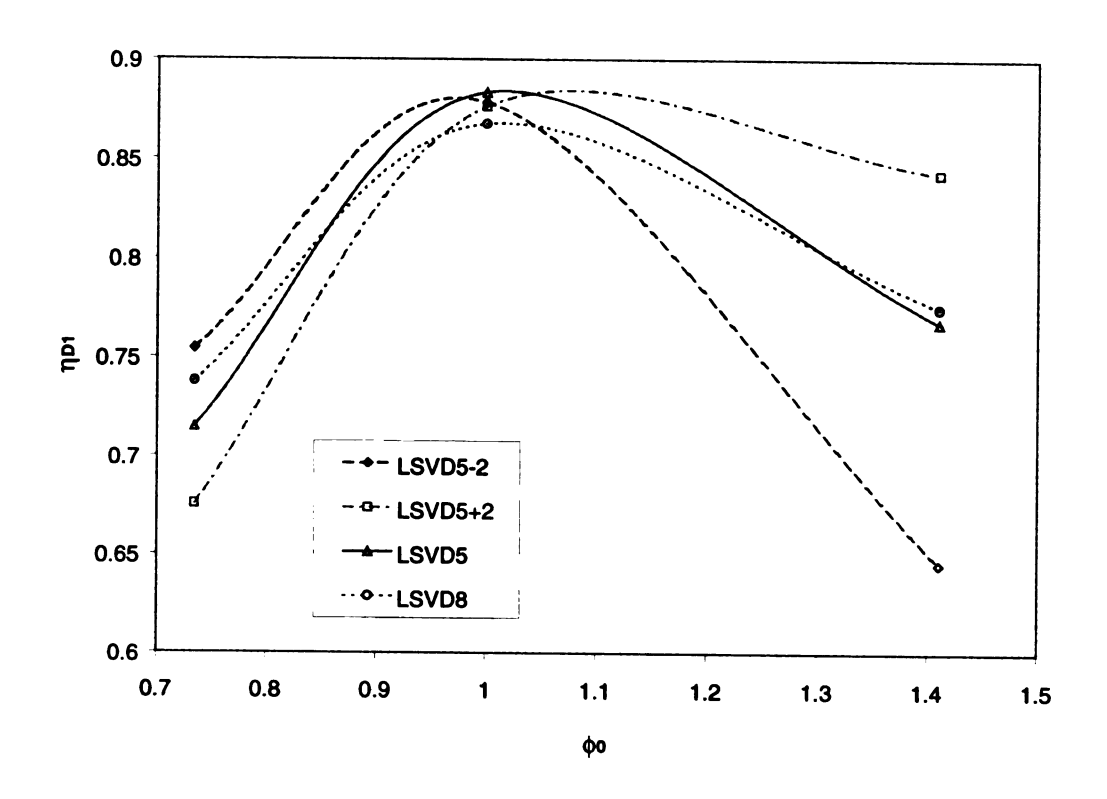


Figure 6.18 The first diffuser efficiency

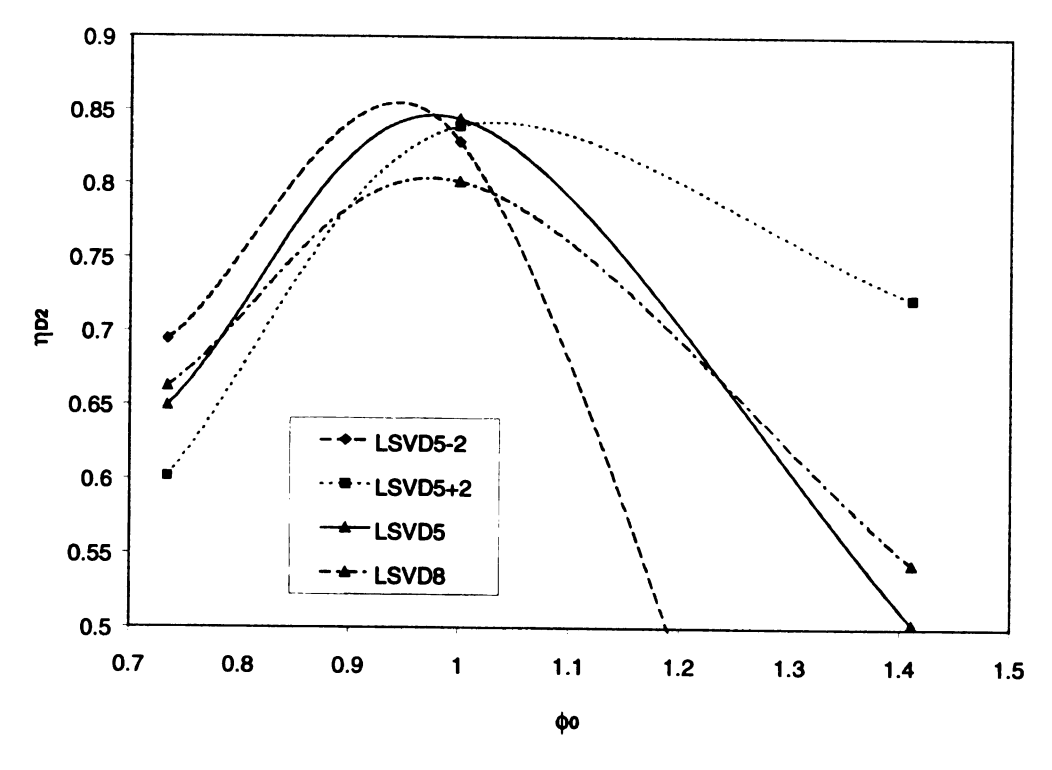


Figure 6.19 The second diffuser efficiency

## 7. CONCLUSIONS AND RECOMMENDATIONS

Experimental testing of a centrifugal compressor with the low solidity vaned diffusers along with two vaneless diffusers and one vaned diffuser has been carried out to understand the effect of design parameters on performance and the results were compared with those from numerical simulation. The design parameters include solidity, turning angle, incidence angle, and the number of vanes. The testing was performed at three different rotational speeds (M<sub>u</sub>=0.69, 0.88, 1.02). The LSVD fulfilled the high expectations since they seemed to combine the advantages of the vaned diffuser systems by providing a good pressure recovery over a wide flow range. Besides steady performance analysis, pressure fluctuations were measured to understand the instability of a compressor stage such as stall and surge using fast response dynamic pressure transducers.

From the results of experimental test and numerical simulation, it is found that solidity is the major parameter affecting the centrifugal compressor along with blade turning angle. The high flow limits for the LSVDs and VNLDs tend to overlap at the designed rotational speed. However, the LSVDs lose their equivalent overload capacity at lower than the designed rotational speed. This effect is due to higher sensitivity of the flat plate vane to the incidence angle, which turns to lower negative value (more incidence angle) at lower than the designed rotational speed. The entailed stall on the pressure

surface is suspected to form an artificial throat limiting the maximum flow through the compressor. This pressure side stall is supported by numerical simulation along with the effects of solidity, blade turning angle and vane setting angle. On the other hand, the real throat of the CVND causes the loss of overload capacity as well. This throat choke allows only a mass flow rate that is approximately 14% less than that achieved by the LSVDs and VNLs at the designed rotational speed. Concerning efficiency, the LSVDs achieve slightly lower than the vaned diffuser but their behavior is similar to the VNL since they obtain higher values over a wide flow range. The efficiency of LSVD5 (0.9 solidity and 14.6° turning angle) is even higher than that of CVND at M<sub>u</sub>=0.69. Moreover, the peak efficiency of the LSVDs at all speeds was attained at higher mass flow than the CVND. Thus, LSVD provides greater stable operating range between peak efficiency flow point and surge flow.

The solidity should be considered as a major design parameter. It gives significant effect on the peak efficiency and flow range; thus, it can be used as an initial design parameter to correlate other parameters like blade length, vane setting angle, radius ratio of vane leading edge, and vane number. In general, the higher solidity diffuser shows the better pressure recovery and this can be a cause of stall at the higher flow rate.

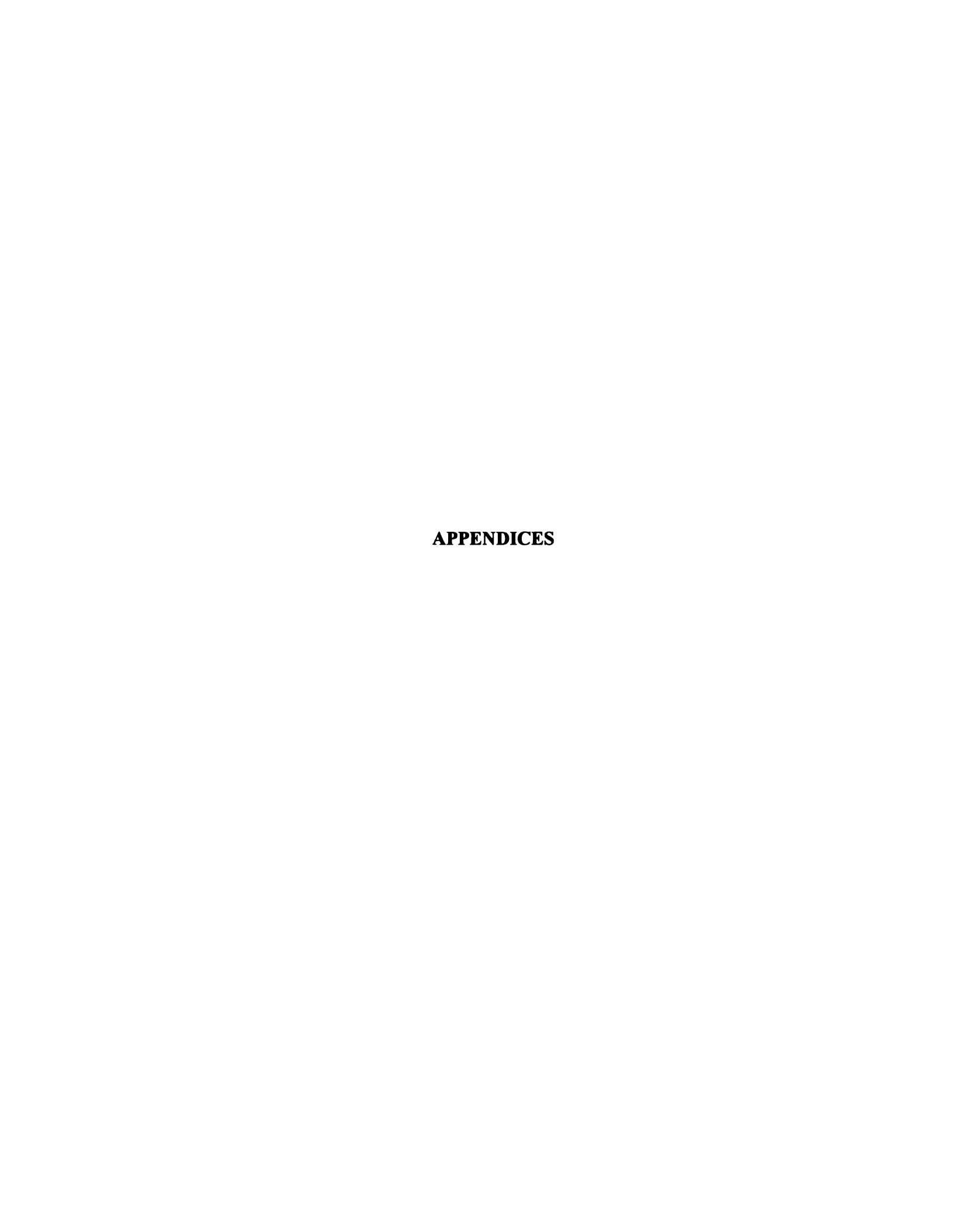
The number of vanes does not have significant effect on the overall performance. At a fixed solidity a LSVD with fewer number of vanes provides better overload capacity and peak efficiency at all speeds even though the difference is small. Better efficiency is due to the higher blade turning angle which shortens the flow path through the diffuser. This means less friction loss despite of the longer vane. On the other hand, a LSVD with more vanes at constant solidity seems to move the surge point to lower mass flow, which

might be due to the shorter vanes allowing a higher positive incidence angle. The low surge flow of the vaneless diffuser obviously cannot be reached by any vaned diffuser configuration.

The vane setting angle effect on the performance has been studied by means of CFD. It shows significant effect on the flow range and rather less on peak efficiency. Flow range will widen with a negative incidence angle, which will suffer peak efficiency due to higher friction loss caused by longer flow path. An incidence of -2 degrees seems to be an optimal incidence angle yielding the best peak efficiency. However, the flow exiting impeller is not uniform in terms of velocity. Profiled leading edge based on measured data in detail from the impeller exit should be considered together for optimization.

A rotating stall was found only with the vaneless diffuser configurations. It is presumed the progressive impeller stall due to the destabilization of the impeller passage flow. This fluctuation was added to the destabilization of the vaneless diffuser and triggered the stage surge with high fluctuation. Deep surge was never reached in vaned diffuser because there was only single component stall. Flow fluctuation at  $M_u$ =1.02 is much stronger in the diffuser than in any components. This surge might be triggered by a destabilization of the diffuser also.

By comparing its results to the experimental data the CFD could be validated. The CFD is very helpful tool to design and develop the turbomachinery. It is believed that more profiled vane will develop the performance of centrifugal compressor. This will be carried out by means of CFD.





### APPENDIX A

### **Diffuser Efficiencies**

The diffuser does not involve work transfer. The efficiency of the diffuser can be defined by the ratio of a rise in enthalpy along an isentropic process to actual enthalpy rise from the diffuser inlet to diffuser outlet.

$$\eta_{D,T-S} = \frac{h_{05s} - h_2}{h_{05} - h_2} \tag{A-1}$$

$$\eta_{D,S-S} = \frac{h_{5s} - h_2}{h_5 - h_2} \tag{A-2}$$

The rise in pressure taken from inlet static to outlet total pressure is used for the efficiency,  $\eta_{D,T-S}$ , while the rise in pressure from inlet static to outlet static pressure for the efficiency,  $\eta_{D,S-S}$ . The process is shown in Figure A-1. Assuming a perfect gas,  $\eta_{D,T-S}$  can be related to inlet static and out total pressure and to the inlet Mach number.

$$\eta_{D,T-S} = \frac{(T_{05s} - T_2)/T_2}{(T_{05} - T_2)/T_2} = \frac{\left(\frac{P_{05}}{P_2}\right)^{r-1/r} - 1}{\frac{T_{05}}{T_2} - 1}$$
(A-3)

Combining Eq.3-21 with Eq.A-3 reduces to

$$\eta_{D,T-S} = \frac{\left(\frac{P_{05}}{P_2}\right)^{r-1/r} - 1}{\frac{\gamma - 1}{2}M_2^2} \tag{A-4}$$

By a similar procedure,  $\eta_{\ D,S\text{-}S}$  can be related to pressure and Mach number.

$$\eta_{D,S-S} = \frac{\left[ \left( \frac{P_5}{P_2} \right)^{\gamma - 1} - 1 \right] \left( 1 + \frac{\gamma - 1}{2} M_5^2 \right)}{\frac{\gamma - 1}{2} \left( M_2^2 - M_5^2 \right)}$$
(A-5)

The polytropic efficiency is defined by

$$\eta_{D,P} = \frac{\gamma - 1/\gamma}{n - 1/n} \tag{A-6}$$

where 
$$\frac{P}{\rho n} = Const.$$

n generally varies from diffuser inlet to outlet. An overall value can be determined from

$$\frac{P_5}{P_2} = \left(\frac{\rho_5}{\rho_2}\right)^n$$

or

$$\frac{P_5}{P_2} = \left(\frac{T_5}{T_2}\right)^{\gamma_{n-1}} = \left(\frac{1 + \frac{\gamma - 1}{2} M_2^2}{1 + \frac{\gamma - 1}{2} M_5^2}\right)^{\gamma_{n-1}}$$
(A-7)

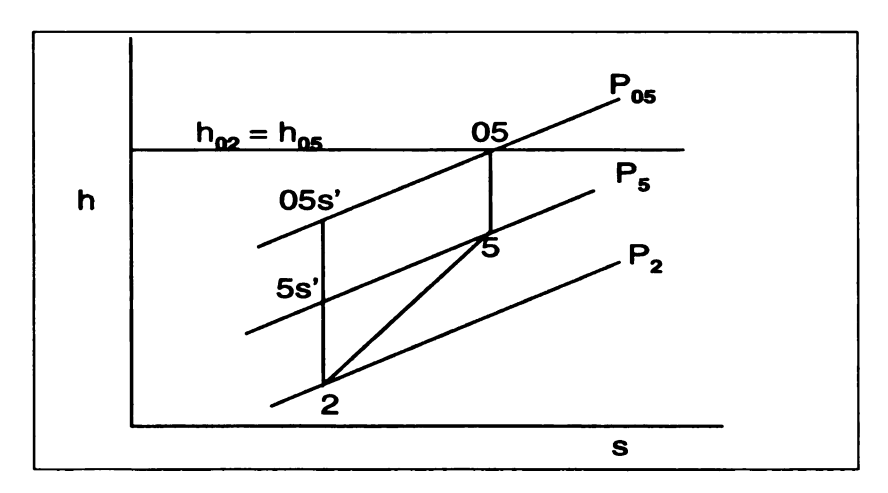
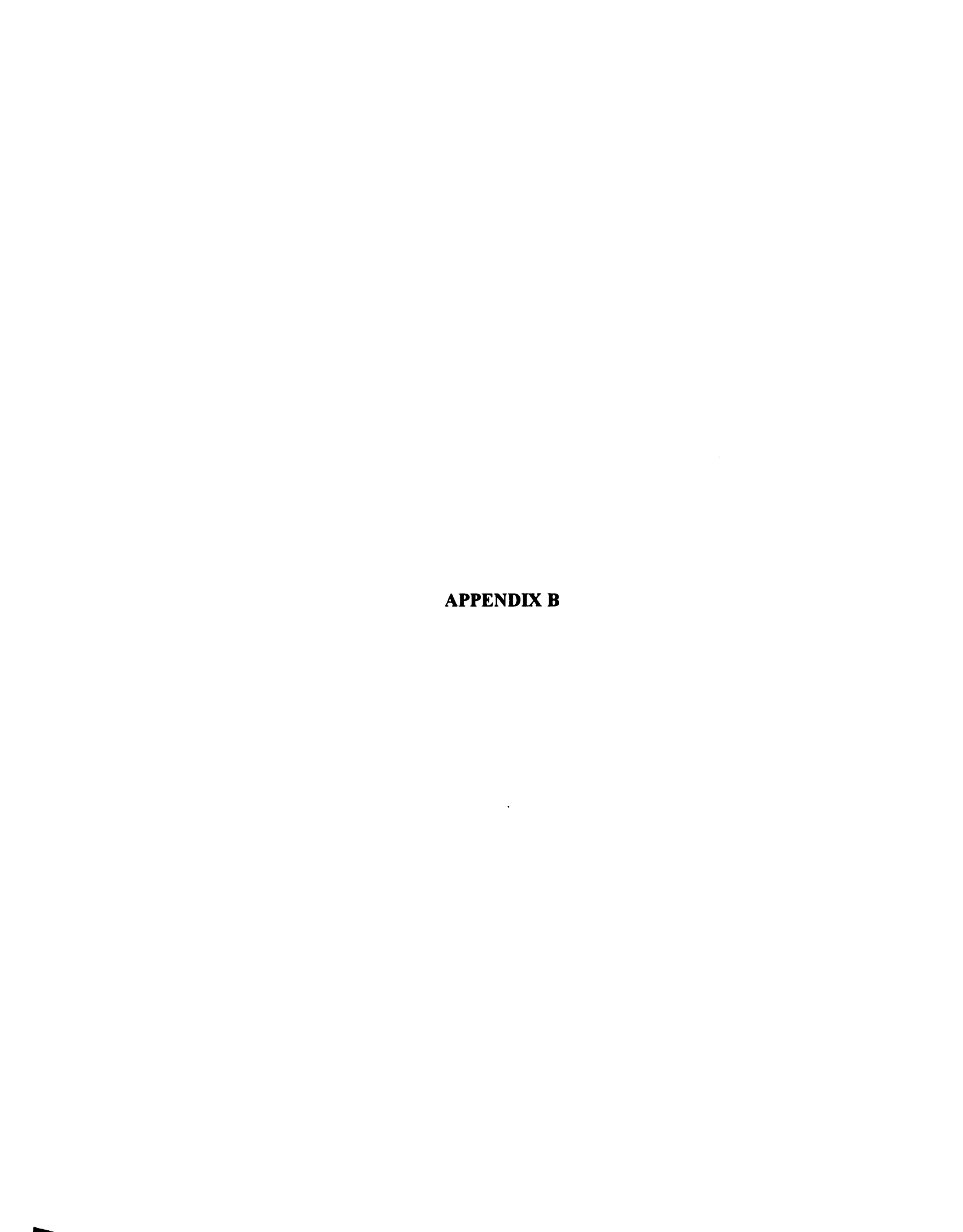


Figure A.1 h-s diagram in a diffuser



# APPENDIX B

# **Specifications of Instruments**

SPECIFICATION		Pressure transducer		
	Company	Validyne		
Pressure Range	DP15-32-N3S4A (P <sub>ind1</sub> )	2.0psid		
	DP15-34-N3S4A (P <sub>ind2</sub> ,ΔP <sub>orf</sub> )	3.2psid		
	DP15-36-N3S4A (P <sub>imp</sub> )	5.0psid		
	DP15-42-N3S4A (P <sub>2</sub> ,P <sub>3</sub> ,P <sub>03</sub> )	20psid		
	DP15-44-N3S4A (P <sub>4</sub> ,P <sub>5</sub> )	32psid		
	DP15-46-N3S4A (P <sub>06</sub> )	50psid		
	Excitation	50psid 5Vrms, 3kHz to 5kHz ±35mV/V		
	Output			
	Accuracy	±0.25% FS includes non-linearity and		
		hysteris, and non-repeatability		
	Temperature range	0 to 160°F		
	Inductance	20 mH, each coil		
Sensor material		410 Stainless steel		
Pressure ports		1/8"-27 NPT – Bleed screws		

SPECIFICATION	Pressure transducer (2xP <sub>06</sub> ) Omega/PX425-030AV		
Company/Model No.			
Excitation	10Vdc		
Output	30mV ± 0.3mV 0. to 50 psia		
Pressure Range			
Accuracy	±0.2% span includes linearity and hysteris		
Temperature range	-54 to 120°C		
Gages	Diffused semiconductor		

SPECIFICATION	Pressure transducer (P <sub>4</sub> ,P <sub>03</sub> ,P <sub>05</sub> )		
Company/Model No.	Omega/HHP-201E		
Pressure Range	0. to 30 psi		
Display	41/2 digit LCD display		
Accuracy	±0.2% span includes linearity and hysteris		
Temperature range	0 to 40°C		
*REMARKS	HHP-100C/101B/101C/101D were used		
	for others, which are similar to HHP-201E.		

SPECIFICATION	Temperature reading		
Company/Model No.	Omega/Type T+DP460		
Temperature range	-99.9 to 401.4 °C		
Accuracy	± 0.5 °C		
Temperature coefficient	0.03°/°C; 5 to 45 °C		
Repeatability	±1 count		
Time stability	1 °C per year		
Input impedance	20 ΜΩ		
Reading rate	1 per second		
Ambient temperature range	5 to 45 °C; 80%RH non-condensing		

SPECIFICATION	Dynamic transducer		
Company/Model No.	PCB/112A02		
Sensitivity	1.0 pC/psi		
Resolution	0.002 psi		
Resonant Frequency	250 kHz		
Rise Time	2 μs		
Pressure Range	0.01 to 100 psi		
Capacitance	18pF		
Temperature range	±400°F		

SPECIFICATION	Inline amplifier		
Company/Model No.	PCB/402A02		
Gain	2.5 mV/psi		
Input Resistance	10 <sup>11</sup> ohm		
Input Capacitance	100 pF		
Noise	15 μV rms		



#### **BIBLIOGRAPHY**

- Amineni, Naresh K, 1996, "Design and Development of Advanced Vaned Diffusers for Centrifugal Compressors," Ph.D. thesis, Michigan State University.
- Aungier, R. H., 1988, "A Systematic Procedure for the Aerodynamic Design of Vaned Diffusers," Flow in Non Rotating Turbomachinery Components, ASME FED Vol. 69, pp. 27-34.
- Aungier, R. H., 1990, "Aerodynamic Performance Analysis of Vaned Diffusers," Fluid Machinery Components, ASME FED Vol. 101, pp. 37-44.
- Baghdadi, S., 1977, "The Effect of Rotor Blade Wakes on Centrifugal Compressor Diffuser Performance -- A Comparative Experiment," ASME Journal of Fluids Engineering, Vol. 99, pp. 45-52.
- Casey, M. V., Dalbert, P., and Roth, P., 1992, "The Use of 3D Viscous Flow Calculations in the Design and Analysis of Industrial Centrifugal Compressors," ASME Journal of Turbomachinery, Vol. 114, pp. 27-37.
- Casey, M. V., Eisele, K., and Muggli, F. A., 1995, "Flow Analysis in a Pump Diffuser, Part 2: Validation of a CFD Code for Steady Flow", ASME FED Vol. 227, pp. 135-143
- Dalbert, P., Gyarmathy, G., and Sebestyen, A., 1993, "Flow Phenomena in a Vaned Diffuser of a Centrifugal Stage," ASME Paper No. 93-GT-53
- Dalbert, P., Wiss, D. H., 1995, "Numerical Transonic Flow Field Predictions for NASA Compressor Rotor 37", ASME Paper No. 95-GT-326
- Eckardt, D., 1975, "Instantaneous Measurements in the Jet Wake Discharge Flow of a Centrifugal Compressor Impeller," ASME Journal of Engineering for Power, Vol. 97, pp. 337-346.
- Fisher, E.H., and Inoue, M., 1981, "A Study of Diffuser/Rotor Interaction in a Centrifugal Compressor," Journal of Mechanical Engineering Science, Vol. 23, pp. 149-156.
- Fringe, P., and Van den Braembusche, R., 1984, "Distinction Between Different Types of Impeller and Diffuser Rotating Stall in a Centrifugal Compressor With Vaneless Diffuser", ASME Journal of Engineering for Gas Turbines and Power, Vol. 106, pp. 468-474

- Hathaway, M. D., Chriss, R. M., Wood, J. R., and Strazisar, A. J., 1993, "Experimental and Computational Investigation of the NASA Low Speed Centrifugal Compressor Flow Field," ASME Journal of Turbomachinery, Vol. 115, pp. 527-542.
- Hayami, H., Senoo, Y., and Utsunomiya, K., 1990, "Application of a Low Solidity Cascade Diffuser to Transonic centrifugal Compressor," ASME Journal of Turbomachinery, Vol. 112, pp. 25-29.
- Hohlweg, W. C., Direnzi, G. L., and Aungier, R. H., 1993, "Comparison of Conventional and Low Solidity Vaned Diffusers," ASME Paper No. 93-GT-98.
- Inoue, M., and Cumpsty, N. A., 1984, "Experimental Study of Centrifugal Impeller Discharge Flow in Vaneless and Vaned Diffusers," ASME Journal of Engineering for Gas Turbine and Power, Vol. 106, pp. 455-467.
- Japikse, D., 1984, "Turbomachinery Diffuser Design Technology," Concepts ETI, Inc., Norwich, Vermont
- Johnson, M. W., and Moore, J., 1980, "The Development of Wake Flow in a Centrifugal Impeller," ASME Journal of Engineering for Power, Vol. 102, pp. 382-390.
- Johnson, M. W., and Moore, J., 1982, "The Influence of Flow Rate on the Wake in a Centrifugal Impeller," ASME Paper No. 82-GT-45.
- Johnson, M. W., and Moore, J., 1983, "Secondary Flow Mixing Losses in a Centrifugal Impeller," ASME Journal of Engineering for Power, Vol. 105, pp. 24-32.
- Kämmer, N., and Rautenberg, M., 1986, "A Distinction Between Different Types of Stall in a Centrifugal Compressor Stage," ASME Paper 85-GT-194
- Kämmer, N., and Rautenberg, M., 1982, "An Experimental Investigation of Rotating Stall in a Centrifugal Compressor Stage," ASME Paper 82-GT-82
- Kim, Won J., and Engeda, Abraham., 1997, "Comparison of Pressure Recovery and Overall Performance of Different Diffusers for Centrifugal Compressors," ASME FED97-3029
- Kline, S. J., Abbott, D. E., and Fox, R.W., 1959, "Optimum Design of Straight Walled Diffusers," ASME Journal of Basic Engineering, Vol. XXX, pp. 321-331.
- Krain, H., 1981, "A Study on centrifugal Impeller and Diffuser Flow," ASME Journal of Engineering for Power, Vol. 103, pp. 688-697.
- Krain, H., 1988, "Swirling Impeller Flow," ASME Journal of Turbomachinery, Vol. 110.

- Lennemann, E., and Howard, J. H. G., 1970, "Unsteady Flow Phenomena in Rotating Centrifugal Compressors," Journal of Engineering for Power, Vol. 92, pp. 65-72.
- Osborne, C., and Sorokes, J., 1988, "The Application of Low Solidity Diffusers in Centrifugal Compressor," Flow in Non Rotating Turbomachinery Component, ASME FED-Vol. 69, pp. 89-101.
- Pampreen, R. C., 1972, "The Use of Cascade Technology in Centrifugal Compressor Vaned Diffuser Design," ASME Journal of Engineering for Power, Vol. 94, pp.187-192.
- Pinarbasi, A., and Johnson, M. W., 1994, "Detailed Flow Measurements in a Centrifugal Compressor Vaneless Diffuser," ASME Journal of Turbomachinery, Vol. 116, pp. 453-461.
- Reneau, L.R., Johnston, J. P., and Kline, S. J., 1967, "Performance and Design of Straight, Two Dimensional Diffusers", ASME Journal of Basic Engineering, Vol. 89, pp. 141-150.
- Rodgers, Colin, 1978, "A Diffusion Factor Correlation for Centrifugal Impeller Stalling," ASME Journal of Engineering for Power, Vol. 100, pp. 592-602.
- Runstadler, P. W. Jr., and Dean, R. C. Jr., 1969, "Straight Channel Diffuser Performance at High Inlet Mach Numbers," ASME Journal of Basic Engineering, Vol. 91, pp. 397-422.
- Senoo, Y., 1984, "Low Solidity Cascade Diffusers for Wide Flow Range Centrifugal Blowers," Flow in Centrifugal Compressors, VKI Lecture Series, 1984-07.
- Senoo, Y., Hayami, H., and Ueki, H., 1983, "Low Solidity Tandem Cascade Diffusers for Wide Flow Range Centrifugal Blowers," ASME Paper No. 83-Gt-3.
- Sorokes, J. M., and Welch, J. P., 1992, "Experimental Results on a Rotatable Low Solidity Vaned Diffuser," ASME Paper No. 92-GT-19.
- Sorokes, J. M., and Welch, J. P., 1991, "Centrifugal Compressor Performance Enhancement Through the Use of a Single Stage Development Rig," Proceedings of the Twentieth Turbomachinery Symposium, Taxas A&M University, pp. 101-112.
- Van den Braembusche, R. A., Fringe, P., and Roustan, M., 1980, "Rotating Non Uniform Flow in Radial Compressors," AGARD CP282

- Yoshinaga, Y., Gyobu, I., Mishina, H., Koseki, F., and Nishida, H., 1980, "Aerodynamic Performance of a Centrifugal Compressor With Vaned Diffuser," ASME Journal of Fluid Engineering, Vol. 102, pp. 486-493.
- Wilmsen, B., 1996, "Design and Development of an Unsteady Data Acquisition System for Centrifugal Compressor," Master thesis, Michigan State University.
- Wilson, D. G., 1991, "The Design of High-Efficiency Turbomachinery and Gas Turbines," The MIT Press
- Watson, N. and Janota, M. S., 1982, "Turbocharging the Internal Combustion Engine," MACMILLAN PUBLISHERS LTD

į.			
•			
,			
,			
,			
ſ			
!			
,			
í			
t			
,			
•			
•			

